

Complex plasmas: An interdisciplinary research field

Gregor E. Morfill* and Alexei V. Ivlev

Max-Planck-Institut für extraterrestrische Physik, 85741 Garching, Germany

(Published 2 October 2009)

Complex (dusty) plasmas are composed of a weakly ionized gas and charged microparticles and represent the plasma state of soft matter. Complex plasmas have several remarkable features: Dynamical time scales associated with microparticles are “stretched” to tens of milliseconds, yet the microparticles themselves can be easily visualized individually. Furthermore, since the background gas is dilute, the particle dynamics in strongly coupled complex plasmas is virtually undamped, which provides a direct analogy to regular liquids and solids in terms of the atomistic dynamics. Finally, complex plasmas can be easily manipulated in different ways—also at the level of individual particles. Altogether, this gives us a unique opportunity to go beyond the limits of continuous media and study—at the kinetic level—various generic processes occurring in liquids or solids, in regimes ranging from the onset of cooperative phenomena to large strongly coupled systems. In the first part of the review some of the basic and new physics are highlighted which complex plasmas enable us to study, and in the second (major) part strong coupling phenomena in an interdisciplinary context are examined. The connections with complex fluids are emphasized and a number of generic liquid and solid-state issues are addressed. In summary, application oriented research is discussed.

DOI: [10.1103/RevModPhys.81.1353](https://doi.org/10.1103/RevModPhys.81.1353)

PACS number(s): 52.27.Lw, 64.70.D-, 67.10.Jn, 68.65.-k

CONTENTS

I. Introduction	1353	III. Kinetic Studies of Liquids and Solids with Complex Plasmas	1372
A. Complex plasmas as a new state of soft matter	1354	A. Relevance to conventional fluids	1372
B. Complex plasmas as a model system to study generic strong coupling phenomena	1354	B. Atomistic dynamics in fluids	1373
C. Complex plasma applications	1355	C. Kinetics of stable flows	1377
II. Basic Properties of Complex Plasmas	1355	D. Kinetics of heat transport	1378
A. Charging of particles	1355	E. Hydrodynamics at the discreteness limit	1380
1. Isotropic plasmas	1355	1. Basic hydrodynamic instabilities	1380
2. Anisotropic plasmas	1357	2. Viscosity-modulation instability	1383
3. Other charging mechanisms	1357	F. Confined fluids	1384
B. Pair interaction between particles	1357	G. Electrorheological fluids	1385
1. Isotropic plasmas	1357	H. Fundamental stability principles of condensed matter	1387
2. Anisotropic plasmas	1358	I. 2D crystals	1389
C. Momentum exchange and other forces acting on particles	1359	1. Kinetic characterization of crystals	1389
1. Momentum exchange	1359	2. Scalings in 2D crystallization	1390
2. Other forces	1360	a. Temperature scaling for domain boundaries	1392
D. Waves	1360	3. Dynamics of dislocations	1392
1. Major wave modes	1360	J. 3D crystals	1394
2. Nonlinear waves	1362	1. Kinetics of 3D liquid-solid phase transitions	1394
E. Phase diagram	1363	a. Phaselets	1395
F. New physics: Examples	1364	b. Interfacial melting	1397
1. Novel classes of non-Hamiltonian systems	1364	IV. Summary and Outlook	1398
a. Examples of non-Hamiltonian dynamics	1365	Acknowledgments	1399
i. Variable charges	1365	References	1399
ii. Plasma wakes	1367		
b. Kinetics of particles with variable charges	1368		
i. Kinetic equation	1368		
ii. Heating	1369		
2. Charge-induced runaway coagulation	1369		

I. INTRODUCTION

While the field of “dusty plasmas” has been established as a subdiscipline of plasma science for several decades—with topics in astrophysics (Morfill and Scholer, 1987), planet formation (Hewins *et al.*, 1996), solar system research (Lucas *et al.*, 1985), planetary rings (Greenberg and Brahic, 1984), atmospheric lightning (Betz *et al.*, 2008), and plasma technology (Bouchoule, 1999) as prominent examples—the field of “complex plasmas” is relatively new and received its initial boost

*gem@mpe.mpg.de

in 1994 when liquid and crystalline plasmas were discovered (Chu and I, 1994; Hayashi and Tachibana, 1994; Thomas *et al.*, 1994). Since then this field has grown dramatically, so that now about 500 publications are recorded annually. This growth in interest rests on three main pillars.

A. Complex plasmas as a new state of soft matter

Complex plasmas are composed of a weakly ionized gas and charged microparticles. The name was originally chosen in analogy to “complex liquids,” which defines the class of soft matter systems that exist in the liquid form. The important point (which incidentally also marks the difference with respect to most naturally occurring dusty plasmas) is that the microparticles are the dominant component as regards energy and momentum transport so that these systems can be “engineered” as practically single-species media. Naturally the detailed physics of interaction between the components determines the “material” properties of complex plasmas—they are thermodynamically open non-Hamiltonian systems and can exist in gaseous, liquid, and solid forms.

Since the discovery of plasma crystals in 1994, there has been much discussion whether these special plasmas may be regarded as a new “state of matter.” The dominant component (the microparticles) is clearly supramolecular, so the question quickly reduces to: Are complex plasmas the new (plasma) state of soft matter?

According to Pierre-Gilles de Gennes, who introduced the term “soft matter,” this describes a class of materials that are “supramolecular, exhibit macroscopic softness, and have metastable states and a sensitivity of their equilibrium to external conditions.” Such materials typically have energies of about room temperature, i.e., they are far above quantum states.

Complex plasmas satisfy all these criteria: The principal supramolecular component (microparticles) naturally obeys classical mechanics. As shown in this review, complex plasmas exhibit macroscopic softness (e.g., surface wave modes), have metastable states (e.g., crystalline or glassy domains), and the equilibrium structure depends on external conditions (such as boundaries and forces applied).

Interestingly, the discovery of the liquid and crystalline states of complex plasmas has therefore substantially extended our picture of the hierarchy of soft matter states, as shown in Fig. 1: If we view soft matter in the simplest way as a mixture of “supramolecular” and “molecular” components, then complex plasmas represent that state where the molecular component is gaseous or ionized, whereas the supramolecular component can exist in solid, liquid, and gaseous or plasma forms, in an analogous way to regular matter.

The increased complexity of soft matter provides enormous richness in possible forms that these materials can attain. Here, of course, lies a large part of the interest in studying such systems—both from the fundamental physics or chemistry point of view and from the many

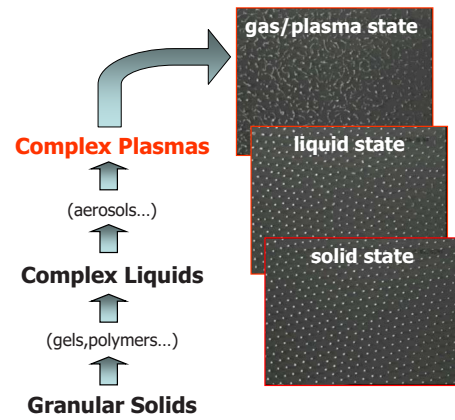


FIG. 1. (Color online) Hierarchy of soft matter states.

possible applications. Complex plasmas are the latest addition to this large and productive field. Because of its special properties, summarized below, this plasma state of soft matter is ideal for fundamental research of strong coupling phenomena at the most elementary—the kinetic (individual particle) level.

Consequently, in the last dozen years a large amount of research has been invested to determine the physics of complex plasmas, starting with the elementary processes such as charging and binary interactions, and continuing with the more complex collective effects, strong coupling phenomena, etc. Remarkable progress has been made, which is documented in recent books and review articles (Tsytoich, 1997; Shukla and Mamun, 2001; Fortov *et al.*, 2005; Vladimirov *et al.*, 2005; Fortov, Iakubov, and Khrapak, 2007; Tsytoich *et al.*, 2008; Shukla and Eliasson, 2009). For this reason we will not discuss the elementary processes in great depth; rather we present a concise review of the current status, and also include advances in new physical phenomena, such as new classes of non-Hamiltonian systems and new regimes of runaway coagulation. The main focus of this “prospective review” will be on the second pillar.

B. Complex plasmas as a model system to study generic strong coupling phenomena

Here we make use of the following unique properties of strongly coupled complex plasmas:

- The microparticles (the principal component) are individually observable.
- The characteristic length scales (e.g., the interaction or coupling length and mean particle separation) are a few 100’s of μm so that complex plasmas are optically thin up to a few 10’s of cm in size—allowing complete three-dimensional diagnostics.
- The characteristic dynamical time scales associated with microparticles (e.g., the inverse Einstein frequency) are in the range of tens of milliseconds, allowing studies of fully resolved individual particle dynamics.

- The rate of momentum or energy exchange between microparticles can substantially exceed the damping rate due to neutral gas friction (i.e., the dynamics of individual particles is virtually undamped), providing a direct analogy to regular liquids and solids in terms of the internal atomistic dynamics.
- The complex plasma systems are very versatile, as might be suspected given the four components (electrons, ions, neutral atoms, and charged microparticles), allowing research into a vast range of structural and temporal self-organization processes.
- Complex plasmas can be manipulated in different ways (e.g., using electrostatic and/or magnetic forces, thermal gradients, light pressure, etc).

These properties of complex plasmas allow us to study a large range of linear, nonlinear, critical, etc. processes (at the fully resolved kinetic level) experimentally for the first time. This provides researchers with a unique opportunity to go beyond the limits of continuous media down to the smallest length scale (the interparticle distance) and thus to explore physical processes from the onset of cooperative phenomena to large strongly coupled systems. In this review we focus on generic processes and emphasize the links to other fields in physics (interdisciplinarity). We discuss recent advances in the atomistic dynamics of liquids and solids, kinetics of stable shear flows, hydrodynamic instabilities at the discreteness limit and the transition to turbulence, nanofluidics, fundamental stability principles of condensed matter, crystallization and melting in two-dimensional (2D) and three-dimensional (3D) systems, “electrorheological” phase transitions, etc.

C. Complex plasma applications

In many important industrial processes (e.g., plasma vapor deposition, chip production, and etching) dust particles are produced as a matter of course during the production process in the plasma reactors (Bouchoule, 1999). Control and removal remains a key issue in future technology (Roca i Cabarrocas *et al.*, 2002). Similar concerns exist in plasma fusion, where the possibility of producing radioactive and toxic dust in plasma-wall interactions is an important design issue that needs to be solved (Federici *et al.*, 2001; Castaldo *et al.*, 2007; Smirnov *et al.*, 2007). There are many other topics that could be discussed, such as plasma medicine (Stoffels *et al.*, 2002; Laroussi and Lu, 2005), plasma biology (e.g., for segregation and size sorting of biological large molecules), plasma nanofluidics (e.g., for functionalizing surfaces so that they become hydrophilic), which may develop into major future technologies. These are some of the emerging topics that will occupy many researchers in the years to come, and which no doubt will all benefit from complex plasma research—be it through straightforward technology transfer or joint application projects.

While in this review we concentrate on topics related to basic science, in our summary we also discuss these emerging applications.

II. BASIC PROPERTIES OF COMPLEX PLASMAS

A. Charging of particles

The particle charge is one of the most important parameters of complex plasmas. It determines the particle interactions with plasma electrons and ions, with electromagnetic fields, between the particles themselves, etc. Hence all studies of complex plasmas necessarily begin with a model describing the particle charging. We mostly focus on gas-discharge plasmas, where the charging is due to the collection of electrons and ions from the plasma, so that the charge is determined by the competition between the electron and ion fluxes on the particle surface. Other processes which can also affect charging (e.g., secondary, thermionic and photoelectric emission of electrons from the particle surface) are discussed only briefly. We address problems such as stationary particle charge, kinetics of the charging, the effect of ion-neutral collisions, the self-consistent effect of the presence of dust, and charge fluctuations.

1. Isotropic plasmas

In the absence of emission processes, the charge of a dust particle immersed in a plasma of electrons and ions is negative. This is because initially, when the particle is uncharged, the electron thermal flux on the particle surface is much larger than the ion flux (the electrons have much higher thermal velocity). The resulting negative charge on the particle leads to repulsion of the electrons and attraction of the ions. The absolute magnitude of the charge grows until the electron and ion fluxes on the particle surface are balanced. On longer time scales, the charge is practically constant and experiences only small fluctuations around its equilibrium value. The stationary surface potential of the dust particle φ_s is determined by the electron temperature T_e , viz., $-\varphi_s \sim T_e/e$. The proportionality coefficient depends on the particular regime which is realized for the electron and ion fluxes to the particle surface.

One of the most frequently used approaches to describe the electron and ion fluxes collected by the particle is the the orbital-motion-limited (OML) approximation (Chung *et al.*, 1975; Allen, 1992; Goree, 1994). In the OML approach three major assumptions are employed: (i) The dust grain is isolated in the sense that other grains do not affect the motion of electrons (ions) in its vicinity, (ii) electrons (ions) do not experience collisions during their approach to the grain, and (iii) there are no barriers in the effective potential. Then the cross section for electron (ion) collection is determined from the laws of conservation of energy and angular momentum, and is given by $\sigma(v) = \pi a^2 (1 - 2e\varphi_s/mv^2)$ for $e\varphi_s < \frac{1}{2}mv^2$ and zero otherwise. Here m and e are the electron (ion) mass and charge (with the appropriate sign) and v denotes the velocity relative to the dust particle of radius a . The electron (ion) current to the particle surface is determined by the integral over the corresponding velocity distribution function $I = en \int v \sigma(v) f(v) d^3v$,

where n is the electron (ion) number density. Using the Maxwellian velocity distribution of plasma particles, we get after the integration

$$I_e = \sqrt{8\pi a^2 n_e v T_e} e^{-z}, \quad I_i = \sqrt{8\pi a^2 n_i v T_i} (1 + \tau z). \quad (1)$$

Here we introduced the following dimensionless parameters: $z = |Q|e/aT_e$, which is the normalized magnitude of the particle charge Q , and $\tau = T_e/T_i$, which is the electron-to-ion temperature ratio. Typically, in low-pressure gas discharge plasmas used in experiments the ionization fraction is very low ($\sim 10^{-6}$ – 10^{-7}); electrons have a temperature about a few eV, whereas ions are effectively cooled to room temperature by collisions with neutrals, so that $T_i \approx T_n$ and hence $\tau \sim 10$ – 100 ; the particle size a usually ranges from ~ 1 to $\sim 10 \mu\text{m}$. It is assumed that the particle charge and surface potential are related to each other via $Q = a\phi_s$. This “vacuum” relation is usually a good approximation for small particles (viz., when a is much smaller than the relevant screening length λ , see next section), which is typical for experimental conditions.

The evolution of the dust grain charge is governed by $\dot{Q} = I_i - I_e$ so that the stationary charge Q_0 is determined from the current balance, $I_e = I_i$. We define the charging frequency Ω_{ch} (inverse charging time) as the relaxation frequency for small deviations of the charge from the stationary value: $\Omega_{\text{ch}} = -d(I_i - I_e)/dQ|_{Q_0}$. Using Eq. (1), we obtain

$$\Omega_{\text{ch}} = \frac{1+z}{\sqrt{2\pi}} \frac{a}{\lambda_{Di}} \Omega_{pi}, \quad (2)$$

where $\lambda_{Di} = \sqrt{T_i/4\pi e^2 n_i}$ is the ion Debye radius and $\Omega_{pi} = v_{Ti}/\lambda_{Di}$ is the ion plasma frequency. In deriving Eq. (2) the limit $\tau \gg 1$ is assumed. Note that the charging frequencies for the thermionic and photoelectric mechanisms are derived by [Khrapak et al. \(1999\)](#) and [Khrapak and Morfill \(2001\)](#).

In the framework of the OML approximation, the dimensionless surface potential z depends on two parameters: the electron-to-ion temperature ratio and the gas type (electron-to-ion mass ratio). In Fig. 2, values of z are presented for different gases (H, He, Ne, Ar, Kr, and Xe) as functions of τ ([Fortov et al., 2005](#)). The particle potential decreases with τ and increases with the gas atomic mass. For typical values of $\tau \sim 10$ – 100 , the dimensionless charge is in the range $z \sim 2$ – 4 . For a particle with $a \sim 1 \mu\text{m}$ and $T_e \sim 1 \text{ eV}$, the characteristic charge is $|Q| \sim (1\text{--}3) \times 10^3 e$.

Analysis of charge fluctuations due to the discrete nature of charging was performed by [Cui and Goree \(1994\)](#) and [Matsoukas and Russell \(1997\)](#). The fluctuations can be described as a stationary, Gaussian, and Markovian process [the so-called Ornstein-Uhlenbeck process, which was originally adopted to describe the stochastic

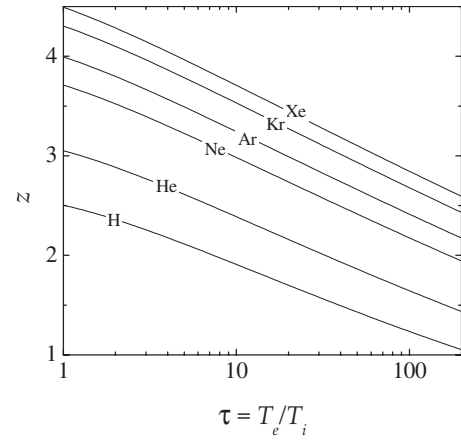


FIG. 2. Charge of a microparticle in low-pressure gas-discharge plasmas. Dimensionless charge $z = |Q|e/aT_e$ of an isolated spherical particle is shown as a function of electron-to-ion temperature ratio $\tau = T_e/T_i$ for isotropic plasmas of different gases. From [Fortov et al., 2005](#).

behavior of the velocity of a Brownian particle ([Uhlenbeck and Ornstein, 1930](#))]. We derive the main properties of charge fluctuations in the framework of the OML approximation (generalization to other charging mechanisms is trivial). The deviation of the particle charge from its equilibrium value, $Q_1(t) = Q(t) - Q_0$, obeys the Langevin equation $\dot{Q}_1 + \Omega_{\text{ch}} Q_1 = q(t)$, where $q(t)$ is the stochastic term describing random acts of electron or ion collections ([Matsoukas and Russell, 1997](#)). The function $q(t)$ satisfies the following properties: $\langle q(t) \rangle = 0$ and $\langle q(t)q(t') \rangle = 2I_0 \delta(t - t')$, where I_0 is the equilibrium current of electrons and ions [i.e., $I_e(Q_0) = I_i(Q_0) \equiv I_0$, see Eq. (1)]. The charge autocorrelation function decays exponentially,

$$\langle Q_1(t)Q_1(t') \rangle = \langle Q_1^2 \rangle \exp(-\Omega_{\text{ch}}|t - t'|), \quad (3)$$

where the relative charge dispersion is $\sigma_Q^2 \equiv \langle Q_1^2 \rangle / Q_0^2 \approx (1+z)^{-1} |e/Q_0|$ (assuming $\tau \gg 1$).

A remarkable advantage of the OML approximation is that the cross sections are independent of the potential distribution around the grain. This is, however, only true when the potential satisfies certain conditions.

The first condition is associated with finite dust density in experiments and is known as the effect of “closely packed” grains. When the interparticle separation Δ is smaller than the characteristic length of interaction between ions (electrons) and the dust grain, then the ion (electron) trajectories are affected by the presence of neighboring particles, thus influencing grain charging ([Barkan et al., 1994](#)).

The second condition is because the OML theory presumes the absence of a barrier in the effective potential energy of electrons (ions), $U_{\text{eff}} = U(r) + (b/r)^2 E$. Here U and E are the electrostatic and kinetic energy of the electron (ion), respectively, and b is the impact parameter with respect to the grain. The barrier is absent for

repulsive interaction, i.e., for electrons, but it can emerge for ions: The (negative) electrostatic energy scales as $U \propto 1/r$ close to the grain, and approaches zero rapidly (exponentially) at large distances (Al'pert *et al.*, 1965; Lampe *et al.*, 2000), so that the (positive) centrifugal part dominates in these limits. However, at intermediate distances an interplay between the electrostatic and centrifugal parts can create a barrier in the effective potential. This barrier could cause reflection of some (low-energy) ions approaching a grain, which would lead to a decrease in the ion current compared to OML theory and, hence, to an increase in $|Q|$. If the fraction of the reflected ions is small then the corrections to OML are also small. For the Yukawa interaction potential (see Sec. II.B) we can write the condition of the OML applicability in the form $\sqrt{2z\tau(a/\lambda)} \leq \ln[z\tau(a/\lambda)]$ (Khrapak *et al.*, 2004). For typical complex plasma parameters $z \sim 1$ and $\tau \sim 100$ we get that OML is applicable for $a/\lambda \leq 0.2$. This corresponds to grains smaller than $\sim 10 \mu\text{m}$, which is typical for most laboratory experiments.

The third condition is due to ion-neutral collisions. In the OML approach collisions of electrons and ions with neutrals are neglected on the basis that their mean-free paths are large compared to the plasma screening length (Goree, 1994). However, theory, numerical simulations, and experiments showed that ion-neutral charge-exchange collisions in the vicinity of a small probe or dust grain can lead to a substantial increase in the ion current to the surface even when the ion mean-free path ℓ_{in} is larger than λ (Zobnin *et al.*, 2000; Lampe, Gavrichchaka, *et al.*, 2001; Khrapak *et al.*, 2005; Hutchinson and Patacchini, 2007). An increase in the ion current can considerably suppress the grain charge. In the weakly collisional regime for ions, characterized by $\ell_{in} \gtrsim R_0$ [where R_0 is determined by $U(R_0) = T_i$], the net ion current on the grain is

$$I_i \approx \sqrt{8\pi} a^2 e n_i v_{Ti} [1 + z\tau + 0.1(\lambda/\ell_{in})z^2\tau^2].$$

For typical dusty plasma parameters $z \sim 1$ and $\tau \sim 100$ collisions can affect particle charging even when the mean-free path is an order of magnitude larger than the screening length. Thus, ion-neutral collisions can be the main process affecting particle charging in the bulk of gas discharges.

2. Anisotropic plasmas

Complex plasmas are often subject to electric fields. For example, in ground-based experiments with rf discharges the particles can levitate in the (pre)sheath above the lower electrode. The electric field causes the plasma to drift relative to the dust component. This in turn can affect the particle charge by changing the collection cross sections and velocity distribution functions of ions and electrons. Usually, the drift of electrons is negligible (relative to their thermal velocity) while the ion drift is large. In this case the electron current to the particle surface is given by Eq. (1), while for ions the

current can be calculated by integrating the OML collection cross section over the appropriate velocity distribution. Calculations showed (Whipple, 1981; Uglov and Gnedovets, 1991) that the charge is practically constant when the ion drift velocity u_i is smaller than the thermal velocity, $u_i/v_{Ti} \leq 1$, then the charge increases by a factor of 2–2.5 and attains a maximum at $u_i/v_{Ti} = (2-3)\sqrt{\tau}$, and decreases at larger u_i .

3. Other charging mechanisms

Note that the collection of ions and electrons from the plasma is not the only possible charging mechanism. Electrons can also be emitted from the particle surface due to thermionic, photoelectric, and secondary electron emission processes. The secondary emission could be due to energetic electrons with an energy of a few hundred eV or higher, or because of metastable neutrals. Field emission might also be important for submicron particles. All these processes are of importance for dust charging in some laboratory experiments, for instance, in thermal plasmas (Fortov *et al.*, 1996; Nefedov *et al.*, 1997, 1999; Khodataev *et al.*, 1998; Samaryan *et al.*, 2000) or in plasmas induced by UV irradiation (Fortov *et al.*, 1998), with photoelectric charging of dust particles (Sickafoose *et al.*, 2000), charging by electron beams (Walch *et al.*, 1995), etc. Under certain conditions, the particles can reach a positive charge, in contrast to the situation discussed previously.

B. Pair interaction between particles

The interaction between charged microparticles in complex plasmas can be affected, e.g., by the plasma absorption on the particle surface, by the variability of the particle charges, polarization, etc. Usually, the interparticle interaction (as well as screening and charging) can be calculated in the approximation of “isolated” particles. In this case, the electrostatic force acting on a particle with a charge Q and located at a distance \mathbf{r} from another particle is $-Qd\varphi/d\mathbf{r}$, where $\varphi(\mathbf{r})$ is the distribution of the electrostatic potential around the particle.

1. Isotropic plasmas

The potential $\varphi(r)$ around an isolated spherical particle in an isotropic plasma satisfies the Poisson equation with the boundary conditions $\varphi(\infty) = 0$ and $\varphi(a) = \varphi_s$. The relation between the surface potential and the particle charge is given by $d\varphi/dr|_{r=a} = -Q/a^2$. For Boltzmann electrons and ions their distributions can be linearized provided the condition $e|\varphi_s|/T \leq 1$ is satisfied. The surface potential is $\varphi_s = (Q/a)(1 + a/\lambda_D)^{-1}$, and for small particles, $a \ll \lambda_D$, we have

$$\varphi(r) = (Q/r)\exp(-r/\lambda_D), \quad (4)$$

where $\lambda_D^{-2} = \lambda_{De}^{-2} + \lambda_{Di}^{-2}$ is the linearized Debye length. Equation (4) is the Debye-Hückel (Yukawa) potential which is often used in complex plasmas. If the surface potential is not small compared to the temperatures of electrons and/or ions, then one can still use Eq. (4) at sufficiently large distances from the particle. In this case, Q should be replaced by some effective value (smaller than the actual particle charge).

Numerical calculations (Kennedy and Allen, 2003) of the particle potential in a plasma with Maxwellian ions show that there is a vacuumlike region near the particle surface where the potential scales as $\varphi(r) \propto r^{-1}$. Then there is a transition region where the potential profile can be well approximated by the Yukawa form (4) with an appropriately chosen screening length (although no strong physical arguments have been given to justify this approximation). At longer distances, typically more than several screening lengths, the long-range asymptote operates and the electrostatic potential can be written as $\varphi(r) \approx Qa/2r^2$ [assuming, as usual, $\tau \gg 1$ and $z \sim 1$ (Al’pert *et al.*, 1965)]. This asymptote is due to the fact that plasma is absorbed at the grain surface, which causes weak violation of the Boltzmann distribution (it holds for distances not exceeding the mean-free path of ions). Note that if the gas pressure is sufficiently high and hence the ion-neutral collisions are sufficiently frequent, the long-range asymptote (at distances about a few mean-free paths) can change to $\varphi(r) \propto r^{-1}$ (Khrapak *et al.*, 2008).

One also should mention a specific “shadowing” force which can be exerted between neighboring microparticles. The mutual distortion of the ion and/or neutral fluxes caused by the microparticles can lead to additional repulsion or attraction between them, with the corresponding potential scaling as $\propto r^{-1}$ (Tsyrovich, 1997; Lampe *et al.*, 2000). Strictly speaking, the shadowing forces are not pairwise since the interaction between (more than two) particles depends on their mutual arrangement. The shadowing force appears to be similar to the depletion force in colloids [see, e.g., Meijer and Frenkel (1994)], although the physical mechanisms responsible for them are completely different.

2. Anisotropic plasmas

As mentioned in the previous section, strong electric fields are often present in laboratory conditions (e.g., in rf sheaths or dc striations). This induces an ion drift and, hence, creates a perturbed region of plasma density around the particle, caused by downstream focusing of ions—the so-called “plasma wake.” One can apply the linear dielectric response formalism [see, e.g., Aleksandrov *et al.* (1984)] to calculate the potential distribution in the wake. This approach is applicable provided ions are weakly coupled to the particle (i.e., the region of nonlinear electrostatic interaction around the particle is small compared to the plasma screening length). Note that larger ion drift velocities imply better applicability of the linear theory. The electrostatic potential created

by a pointlike charge at rest is defined in this approximation as

$$\varphi(\mathbf{r}) = \frac{Q}{2\pi^2} \int \frac{e^{i\mathbf{k}\cdot\mathbf{r}} d\mathbf{k}}{k^2 \varepsilon(0, \mathbf{k})}, \quad (5)$$

where $\varepsilon(\omega, \mathbf{k})$ is the anisotropic plasma permittivity. Using a certain model for the permittivity, one can calculate the anisotropic potential distribution (Nambu *et al.*, 1995; Ishihara and Vladimirov, 1997; Xie *et al.*, 1999; Lapenta 2000; Lemons *et al.*, 2000). The potential profile can also be obtained from numerical modeling (Melandsø and Goree, 1995; Lampe *et al.*, 2000; Winske, 2001; Lapenta, 2002; Vladimirov *et al.*, 2003).

Physically, the generation of plasma wakes in anisotropic dusty plasmas is similar to the generation of electromagnetic waves by a particle which is placed in a moving medium (Ginzburg, 1996), and the analogy with the Vavilov-Cherenkov effect can be useful. The potential is no longer monotonic within a certain solid angle downstream from the particle, but has a well pronounced extremum (maximum for a negatively charged particle). Numerical modeling shows that the shape of the wake potential is sensitive to the ion-neutral collisions (Hou *et al.*, 2003) and the electron-to-ion temperature ratio which governs Landau damping (Lampe, Joyce, and Ganguli, 2001). In typical situations, these mechanisms can effectively “smear out” the oscillatory wake structure, leaving a single maximum.

We illustrate how the wake potential depends on the plasma flow. The ion drift velocity is conveniently characterized by the value of the “thermal” Mach number $M_T = u_i/v_{Ti}$. The pronounced anisotropic wake structure appears in both subthermal and superthermal regimes of the drift (both regimes are ubiquitous for typical experimental conditions). In this context, we mention the work of Lampe *et al.* (2000) where some examples of the wake structures, calculated numerically for different plasma conditions, are presented (see Fig. 3).

First we consider subthermal ion drift, $M_T \lesssim 1$. The potential profile in this case can be calculated from Eq. (5) analytically within the Bhatnagar-Gross-Krook (BGK) approach for the ion-neutral collision integral (Schweigert, 2001; Ivlev, Zhdanov, Khrapak, and Morfill, 2005). The far-field potential has a well-known $\propto r^{-3}$ asymptote (Montgomery *et al.*, 1968). By combining this with the near-field Yukawa core, in the case of small collisionality (viz., small ratio of the ion-neutral collision frequency to the ion plasma frequency), we can approximate the potential by the following expression (Kompaneets, 2007):

$$\varphi(r, \theta) = Q \left[\frac{e^{-r/\lambda_D}}{r} - 2 \sqrt{\frac{2}{\pi}} \frac{M_T \lambda_D^2}{r^3} \cos \theta - \left(2 - \frac{\pi}{2} \right) \frac{M_T^2 \lambda_D^2}{r^3} (3 \cos^2 \theta - 1) \right] + o(M_T^2/r^3), \quad (6)$$

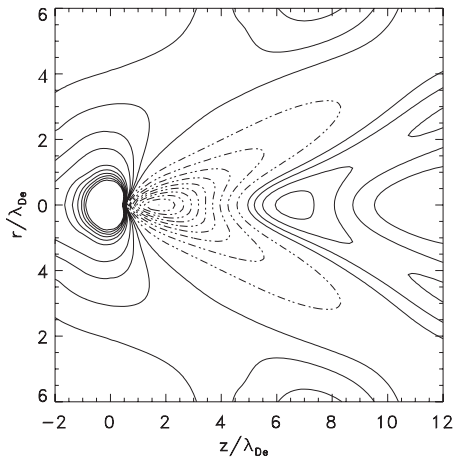


FIG. 3. Plasma wake. The complex structure of the wake potential $\varphi(\mathbf{r})$ (plasma flows to the right). Calculations are for collisionless ions with a shifted Maxwellian distribution (drift velocity $u_i = 7.5v_T$) and for Boltzmann electrons (temperature $T_e = 25T_i$). The (negatively charged) grain is at the center of the left-most node, solid and dashed curves indicate contour lines for negative and positive potentials, respectively, distance is in units of λ_{De} . From [Lampe et al., 2000](#).

where θ is the angle between \mathbf{r} and \mathbf{u}_i . Equation (6) shows that microparticles attract each other in a certain solid angle along the flow, and repel in the transverse direction. Such behavior is usually observed in ground-based experiments—particles levitating in, e.g., (pre)sheaths of rf discharges ([Melzer, Schweigert, et al., 1996](#)) form stable vertical “strings.” This result highlights the importance of the self-consistent consideration of the ion kinetics where the ion-neutral collisions are properly taken into account. Indeed, the (somewhat arbitrary) use of, e.g., a shifted Maxwellian ([Wang et al., 1981](#)) to model a flowing plasma yields attraction between particles in the transverse direction, which contradicts observations.

In some ground-based experiments particles levitate in regions where the electric field is so strong that the thermal Mach number can be significantly larger than unity; also, the collisionality can be rather high. Then Eq. (6) is no longer applicable. Recent calculations [based on the constant-cross-section model for the ion-neutral collision integral; [Kompaneets et al. \(2007\)](#)] take both effects into account, and the resulting interaction potential is in excellent agreement with the direct measurements (performed for $M_T \sim 10$).

C. Momentum exchange and other forces acting on particles

The forces acting on microparticles in complex plasmas can be conditionally divided into “internal” forces due to mutual interactions between microparticles, and “external” forces due to interactions with other plasma species (i.e., neutrals, ions, and electrons), as well as other electric, magnetic, and thermal forces.

1. Momentum exchange

We consider interactions between species i and j which are characterized in terms of the corresponding momentum exchange rate ν_{ij} . The momentum exchange between microparticles and other species plays an important role in complex plasmas. For example, the momentum transfer in collisions with the neutral gas “cools down” the system of microparticles, introducing some damping. The forces due to the momentum transfer from electrons and ions to the charged grains (the electron and ion drag forces) often determine static and dynamical properties of microparticles, affect wave phenomena, etc. And, the most important, the momentum exchange in grain-grain collisions and its competition with the momentum transfer in grain-neutral collisions governs transport, fluid properties, phase transitions, etc. As pointed out in the introduction, complex plasmas can be engineered as essentially a “single-species particle fluid” (when the interactions between the grains dominate), or as a “particle laden gas” (when the interactions with the background medium are of similar or greater importance).

For the grain-neutral collisions the momentum exchange (neutral damping) rate is ([Epstein, 1924](#))

$$\nu_{dn} = \delta(8\sqrt{2\pi/3})(m_n/m_d)a^2n_n v_{T_n}. \quad (7)$$

The value of the numerical factor δ depends on the exact process of neutral scattering from the particle surface. For example, $\delta=1$ for the cases of complete absorption and specular reflection, while $\delta=1+\pi/8$ for diffuse scattering with full accommodation. The latter value is more consistent with recent experimental results ([Liu et al., 2003](#)). Since the notation for the neutral damping rate is used throughout, for the sake of convenience below we omit the subscript and simply employ ν .

As regards the grain-grain collisions as well as ion-grain collisions, the regimes of the momentum exchange are determined by the scattering parameter β , which is the ratio of the bare Coulomb interaction energy at the screening length scale λ to the mean kinetic energy (temperature). Assuming typical experimental conditions, for ion-grain collisions $\beta_{di} = |Q|/\lambda T_i \sim z\tau(a/\lambda) \sim 0.1-30$, and for grain-grain collisions $\beta_{dd} = Q^2/\lambda T_d \sim |Q/e|(T_i/T_d)\beta_{di} \sim 10^4-10^6$ ([Hahn et al., 1971](#); [Khrapak et al., 2002](#)). The weak scattering regime, $\beta \lesssim 1$, is similar to the Coulomb scattering occurring in conventional plasmas ([Barnes et al., 1992](#)), where the momentum exchange rate does not depend on the sign of the interaction. For the strong scattering, $\beta \gg 1$, the repulsive interaction is similar to that between hard spheres of radius $\approx \lambda \ln 2\beta$ ([Baroody, 1962](#); [Khrapak et al., 2004](#)), whereas for the attractive interaction the potential barrier appears (see Sec. II.A) and then scattering is determined by the position of the barrier.

For grain-grain collisions the regime $\beta_{dd} \gg 1$ is typical so that the analogy with hard-sphere collisions can be used (Khrapak *et al.*, 2004). The momentum exchange rate is then

$$\nu_{dd} \approx (4\sqrt{2\pi}/3)n_d v_{Td} \lambda^2 \ln^2 2\beta_{dd}.$$

The binary collision approach for the interparticle interactions is naturally valid as long as the system is sufficiently dilute. As the number density of microparticles grows the coupling with increasing number of neighbors becomes important, so that eventually the collective modes take over and the momentum exchange rate scales proportional to the Einstein frequency $\sim \Omega_E$ (see Sec. II.D). The crossover from the binary to the collective momentum exchange regime is determined by the condition that the radius of the effective hard-sphere interaction $\approx \lambda \ln 2\beta_{dd}$ is comparable to the interparticle distance $\approx \Delta$, which naturally has the leading scaling coinciding with the strong-coupling condition $\Gamma_S \sim 1$ (see Sec. II.E).

The ion drag force—the momentum transfer from the flowing ions to charged microparticles—is an inevitable and exceptionally important factor in complex plasmas. Ion flows are usually induced due to “global” large-scale electric fields that can be either caused by natural inhomogeneities in a discharge plasma (ambipolar fields) or induced by external sources to manipulate microparticles (see Sec. II.D). For typical experimental conditions the ion drag is pointed in the direction opposite to the electric force, and their competition usually determines global structures in complex plasmas (Goree *et al.*, 1999; Morfill *et al.*, 1999; Samsonov and Goree, 1999). For subthermal flows ($M_T \ll 1$), the ion drag force F_{id} is reduced to a particularly simple expressions in the regimes of weak and strong collisional coupling. For the weak coupling we directly employ results valid for $\beta_{di} \leq 5$ (Khrapak *et al.*, 2002; Khrapak, Ivlev, *et al.*, 2003),

$$F_{id} \approx \sqrt{2/9\pi}(T_i/e)^2 \Lambda \beta_{di}^2 M_T, \quad (8)$$

where $\Lambda(\beta_{di}) \approx -e^{\beta_{di}/2} \text{Ei}(-\beta_{di}/2)$ is the modified Coulomb logarithm integrated over the Maxwellian distribution function. Equation (8) yields the scaling $F_{id} \propto (Q/\lambda)^2$. In the linear regime $\beta_{di} \ll 1$ the logarithm is reduced to $\Lambda \approx \ln \beta_{di}^{-1}$, which is identical to the results of the Coulomb scattering theory (Barnes *et al.*, 1992). In the opposite regime of strong coupling, $\beta_{di} \gg \beta_{cr} \approx 13$, one should replace $\Lambda \beta_{di}^2$ with $2 \ln^2 \beta_{di}$ in Eq. (8). In this case the force depends logarithmically on Q and λ . Note that for $M_T \ll 1$ the screening length is determined by ions, $\lambda \approx \lambda_{Di}$, since the electron temperature is typically two orders of magnitude higher than the ion (neutral) temperature.

2. Other forces

If a temperature gradient is present in a neutral gas, then the particle experiences a thermophoretic force. This force is due to the asymmetry in the momentum transfer from neutrals and is directed towards lower gas temperatures. In the case of full accommodation of neutral ions colliding with the particle surface the thermophoretic force is given $\mathbf{F}_{th} \approx -3.3(a^2/\sigma_{nn})\nabla T_n$ (Rothermel *et al.*, 2002). Thus, the thermophoretic force is proportional to the temperature gradient, depends on particle radius and gas type (through the cross section of neutral-neutral collisions, σ_{nn}), but does not depend on the gas pressure. For particles of about $1 \mu\text{m}$ radius and mass density $\sim 1 \text{ g/cm}^3$ in argon gas, F_{th} is comparable to the force of gravity at $|\nabla T_n| \sim 10 \text{ K/cm}$.

The neutral drag force can be also important when gas is flowing relative to the particles. The Knudsen number $\text{Kn} = (\sigma_{nn} n_n a)^{-1}$ in complex plasmas is typically quite large and the gas flow velocity u_n is small compared to the thermal velocity of neutrals v_{T_n} . Then $F_n = m_d \nu u_n$, where the momentum exchange rate ν is given by Eq. (7). The neutral drag force can be employed to exert controllable stresses and induce shear flows in complex plasmas (see Sec. III.C).

D. Waves

The charged dust grains embedded in plasmas not only change the electron-ion composition and thus affect conventional plasma wave modes (e.g., ion-acoustic waves), but also introduce new low-frequency modes associated with the microparticle motion, alter dissipation rates, give rise to instabilities, etc. Moreover, the particle charges vary in time and space, which highlights important qualitative differences between complex plasmas and usual multicomponent plasmas. Depending on the magnitude of the electrostatic coupling between microparticles, complex plasmas can be in weakly coupled (gaseouslike) or strongly coupled (liquidlike) states, and they can self-organize to spontaneously form crystalline structures (see Sec. II.E).

Complex plasmas observed in laboratory or space experiments usually form strongly coupled liquid or crystalline states. At the same time, for weakly coupled plasmas the theoretical analysis of the wave modes and major instabilities can be performed in the most simple form. Therefore we first consider major wave properties of gaseous complex plasmas, and then discuss features peculiar to the waves in strongly coupled regimes.

1. Major wave modes

The role of charged microparticles in the (quasineutral) plasma composition is characterized in terms of the ion-to-electron density ratio which, in turn, can be conveniently measured by the Havnes parameter P (Havnes *et al.*, 1987),

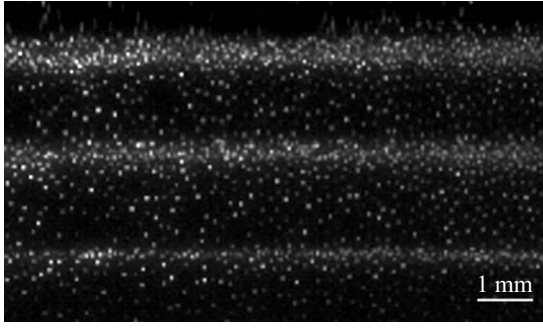


FIG. 4. Spontaneous excitation of dust waves observed in laboratory experiments. The experiments were carried out in a argon rf discharge at a pressure of 23 Pa with particles of 1.28 μm diameter. From [Schwabe et al., 2007](#).

$$n_i/n_e - 1 = |Q/e|n_d/n_e \equiv P. \quad (9)$$

In the gaseous regime only longitudinal acoustic waves are sustained—the so-called dust-acoustic (DA) mode. The phase velocity does not depend on the dust temperature, and in the long-wavelength regime $k\lambda_D \ll 1$ and the limit $\tau \gg 1$ it can be written as ([Rao et al., 1990](#))

$$C_{\text{DA}} \approx \sqrt{\frac{|Q/e|P T_i}{1 + P m_d}}.$$

The dust waves, either self-sustained or excited externally, have been seen in numerous experiments under quite different conditions ([Merlino et al., 1998](#); [Zobnin et al., 2002](#); [Fortov et al., 2003](#); [Khrapak, Samsonov, et al., 2003](#); [Piel et al., 2006](#); [Annibaldi et al., 2007](#); [Schwabe et al., 2007](#); [Thomas et al., 2007](#)). Figure 4 shows an example of self-excited DA waves in a rf discharge plasma. A peculiarity of the DA waves is that the charge-to-mass ratio of the dust grains is typically 10^8 – 10^{10} times smaller than that of the ions and, therefore, the dust waves have relatively low frequencies, ~ 10 – 100 Hz.

Wave properties of strongly coupled plasmas significantly deviate from those of ideal gaseous plasmas. There are a number of different theoretical approaches to study waves in strongly coupled systems: These are, e.g., the quasilocalized-charge approximation ([Kalman and Golden, 1990](#)) employed for complex plasmas by [Rosenberg and Kalman \(1997\)](#) and [Kalman et al. \(2000\)](#), the multicomponent kinetic approach by [Murillo \(1998, 2000\)](#), and the generalized hydrodynamic (viscoelastic) approach applied by [Kaw and Sen \(1998\)](#), [Xie and Yu \(2000\)](#), and [Kaw \(2001\)](#). The latter is probably the most physically “transparent” approach which allows us to track the evolution of the dispersion properties of complex plasmas in a broad range of electrostatic coupling, from the ideal gaseous state up to the strongly coupled state—when the system crystallizes. There have also been molecular dynamics (MD) simulations of the wave modes in strongly coupled complex plasmas ([Winske et al., 1999](#); [Ohta and Hamaguchi, 2000a](#)), which are in reasonably good agreement with the results of the above mentioned theoretical approaches.

In the framework of the viscoelastic model, parameters of the stress operator, i.e., shear viscosity η and Maxwell relaxation time τ_M (see Sec. III.B), are determined by the correlation part of the electrostatic interaction energy [which is a function of the coupling and screening parameters Γ and κ , see Eq. (11)]. For the liquid phase in the range $1 \lesssim \Gamma \lesssim 200$ the correlation energy (normalized by T_d) can be well approximated by the scaling $u = a\Gamma + b\Gamma^{1/4} + c + d\Gamma^{-1/4}$ ([Farouki and Hamaguchi, 1994](#)), where the coefficients a , b , c , and d are some functions of the screening parameter κ . In the one-component plasma (OCP) limit, $\kappa = 0$, the Monte Carlo (MC) simulations ([Slattery et al., 1980](#)) yield $a \approx -0.89$, $b \approx 0.94$, $c \approx -0.80$, and $d \approx 0.18$. The dependence of the coefficients on the screening parameter is rather weak ([Farouki and Hamaguchi, 1994](#)), e.g., $a(\kappa) \approx -0.89 - 0.10\kappa^2 + 0.0025\kappa^4 + \dots$, which means that the OCP results are quite applicable for moderate κ . The relation between the viscosity and the relaxation time is given by $\eta = -\frac{1}{20}(u + \frac{5}{3}\Gamma \partial u / \partial \Gamma) v_{Td}^2 \tau_M$ ([Ichimaru et al., 1987](#)). The viscosity itself can be deduced from the results of numerical simulations and experiments ([Saigo and Hamaguchi, 2002](#); [Salin and Caillol, 2002, 2003](#); [Nosenko and Goree, 2004](#)).

In addition to longitudinal DA waves, strongly coupled media may also sustain transverse shear waves ([Kaw and Sen, 1998](#); [Kaw, 2001](#)). In the hydrodynamic regime $\omega\tau_M \ll 1$ we obtain an ordinary damped shear mode in viscous liquids, $\omega \approx -\frac{4}{3}i\eta k^2$. In the opposite elastic regime $\omega\tau_M \gg 1$ we obtain a nondispersive acoustic mode, $\omega/k \approx \sqrt{\frac{4}{3}\eta/\tau_M}$, which is analogous to elastic shear waves in solids. The self-excited shear waves in liquid complex plasmas have been observed experimentally ([Pramanik et al., 2002](#)).

We now consider waves in plasma crystals. In this case they are referred to as dust-lattice (DL) modes, and their phase velocities $C_{l,t} = \lim_{k \rightarrow 0} (\omega_{l,t}/k)$ can be written as ([Peeters and Wu, 1987](#); [Wang et al., 2001](#); [Zhdanov, Quinn, et al., 2003](#)) $C_{l,t} = C_{\text{DL}} F_{l,t}(\kappa)$, where subscripts l and t denote the longitudinal and transverse polarization, respectively, and

$$C_{\text{DL}} = \sqrt{Q^2/m_d \lambda_D},$$

is the DL velocity scale. The magnitude of C_{DL} is of the order of a few cm/s for typical experimental conditions ([Nunomura et al., 2000, 2002](#)). The exact formulas for the functions $F_{l,t}(\kappa)$ are rather complicated. However, for a practical range of κ the functions can be well approximated by simple polynomial expansions: For a 2D hexagonal lattice, the leading κ terms give $F_l \approx 2.69\kappa^{-1}$ and $F_t \approx 0.51\kappa^{-1/2}$ ([Peeters and Wu, 1987](#); [Zhdanov, Quinn, et al., 2003](#)); for the 3D case, the longitudinal function depends on the lattice type, $F_l \approx 5.0(7.0)\kappa^{-3/2}$ for a bcc (fcc) lattice, whereas the transverse function $F_t \approx 0.19\kappa^{-1/2}$ is the same for both lattices ([Wang et al., 2001](#)). For arbitrary κ one can obtain the phase velocities of all modes in the long-wavelength regime using the

results for the elastic constants of Yukawa crystals [see, e.g., [Robbins et al. \(1988\)](#)].

Depending on the phase state—(liquid or solid)—one can choose different time scales to characterize collective dynamics of microparticles. For liquid and amorphous solid complex plasmas the dust plasma frequency $\Omega_{pd} = \sqrt{4\pi Q^2 n_d / m_d}$ can be used as the measure, whereas for crystals the modes depend on a particular lattice structure so that the Einstein frequency Ω_E is the more appropriate scale. The ratio Ω_E / Ω_{pd} is a (monotonously decreasing) function of the screening parameter κ , and for different lattices it typically varies between a few and a few tenths ([Robbins et al., 1988](#)). To avoid confusion, we use Ω_E^{-1} as the characteristic dynamical time scale for both liquids and solids.

2. Nonlinear waves

Nonlinear phenomena in complex plasmas are very diverse, due to the large number of different wave modes which can be sustained. Waves can become nonlinear as a result of different processes, which are not necessarily external forcing or wave instabilities—these can also be regular collective processes of nonlinear wave steepening. In the absence of dissipation (or when the dissipation is small enough), nonlinear steepening can be balanced by wave dispersion which, in turn, can result in the formation of solitons. When the dissipation is large, it can overcome the role of dispersion and then the balance of nonlinearity and dissipation can generate shock waves. In many cases the lowest-order nonlinear terms are quadratic, and then the weakly nonlinear soliton dynamics is governed by the Korteweg–de Vries (KdV) equation ([Karpman, 1975](#)). For solitons of arbitrary amplitude, the Sagdeev pseudopotential method is convenient ([Sagdeev, 1966](#)): In particular, this method allows us to determine the upper value of the Mach number beyond which the dispersion is no longer sufficient to balance the nonlinearity and, thus, a collisionless shock is formed due to “collective” dissipation. The “conventional” dissipation is often determined by viscosity, and then the shock waves can be described by the KdV-Burgers equation ([Karpman, 1975](#); [Shukla, 2003](#)).

There is a rich variety of mechanisms which determine nonlinear and dispersive properties of strongly coupled complex plasmas. A comprehensive investigation of nonlinear particle dynamics can give us an opportunity to study fundamental wave phenomena (mode interaction, umklapp processes, phonon scattering on defects, etc.) at the kinetic level. We discuss several experiments on nonlinear waves in complex plasmas.

Longitudinal dust solitary waves of moderate amplitude were observed in experiments by [Nosenko, Nunomura, and Goree \(2002\)](#); [Samsonov et al. \(2002\)](#) performed in rf discharges at low pressures ($p \approx 1.8\text{--}2$ Pa). The solitons were excited in crystalline monolayers by electrical pulses or by laser beams. The equation for the nonlinear wave dynamics is ([Samsonov et al., 2002](#); [Zhdanov et al., 2002](#))

$$\frac{\partial^2 u}{\partial t^2} + \nu \frac{\partial u}{\partial t} = C^2 \frac{\partial^2}{\partial x^2} \left(u + \ell^2 \frac{\partial^2 u}{\partial x^2} + \frac{1}{2} \Lambda u^2 \right). \quad (10)$$

Here $u = \partial \delta \mathbf{r} / \partial \mathbf{x} \approx -\delta n_d / n_d$ is the particle density modulation expressed via the longitudinal derivative of the (in-plane) displacement, C is the long-wavelength (isotropic) DL phase velocity, ℓ^2 is the dispersion coefficient which generally can have either sign (it has the dimension of squared length), and Λ is the nonlinearity coefficient. Without the frictional dissipation, Eq. (10) is readily reduced to the KdV equation by employing the stretched coordinates. The soliton can only exist when ℓ^2 and Λ have opposite signs so that the following relations can be fulfilled: $-\frac{1}{3}\Lambda A = 4\ell^2 / L^2 = M^2 - 1$, where A and L are the soliton amplitude and width, respectively, and $M = V / C$ is the Mach number for the soliton velocity ([Samsonov et al., 2002](#)). The Mach number is a convenient control parameter which defines the soliton profile, $-u = A \cosh^{-2}(\xi / L)$, with $\xi = x - Vt$.

In 2D hexagonal lattices ([Zhdanov et al., 2002](#)), ℓ^2 is always positive and has a weak dependence on the direction of propagation, and Λ is always negative and can depend on the direction substantially, especially at $\kappa \geq 1$. Such a combination of signs implies that only compressive ($A > 0$) supersonic ($M > 1$) solitons can propagate in crystalline monolayers, as observed in experiments. For $\kappa \geq 1$, one can calculate the parameters of Eq. (10) using the results for a 1D string ([Samsonov et al., 2002](#)): $C^2 = C_{\text{DL}}^2 \kappa^2 [G(\kappa) / \kappa]''$, $\ell^2 = \frac{1}{12} \lambda_{\text{D}}^2 \kappa^2 [G''(\kappa) / \kappa]'' / [G(\kappa) / \kappa]''$, and $\Lambda = \kappa [G(\kappa) / \kappa]''' / [G(\kappa) / \kappa]''$, where $G(\kappa) = -\ln(e^\kappa - 1)$. This relatively simple theoretical model provides good agreement with experiments. If the neutral gas pressure is low enough, the friction does not destroy the soliton ([Samsonov et al., 2002](#)). The perturbation simply slows down, approaching the asymptote $V = C$, and the form of the soliton changes in accordance with the analytical solution (i.e., the amplitude decreases and the width increases, keeping the soliton relation $AL^2 = \text{const}$). Thus, one can speak about a weakly dissipative soliton when the dissipation time scale $\sim \nu^{-1}$ exceeds the time scale of the wave itself $\sim \Omega_E^{-1}$.

For the theoretical description of dust shock waves, the generalized hydrodynamic approach has been proposed ([Kaw and Sen, 1998](#); [Shukla, 2003](#)). This approach suggested that in a strongly coupled regime weak shocks cannot be (generally) described by the KdV-Burgers equation ([Kaw and Sen, 1998](#)). In experiments, “pure” shocks were only observed so far in 2D crystals ([Samsonov et al., 2004](#)). (Here the term “pure” implies that the momentum exchange in dust-dust collisions prevails over the momentum loss due to neutral gas friction, $\Omega_E, \nu_{dd} \gg \nu$, so that again complex plasmas have properties of single-species fluids.) These shocks caused melting of the crystal behind the front, as shown in Fig. 5. As the shock propagated and weakened it was seen that the melting ceased. Further propagation of the pulse was in the form of a soliton, as described above.

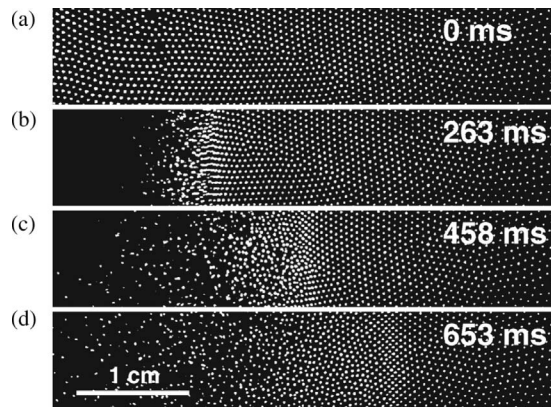


FIG. 5. Dust shock wave propagating in a monolayer hexagonal lattice. Experiments were performed in argon rf discharge at pressure of 1–2 Pa, with particles of $8.9\mu\text{m}$ diameter. Particles were illuminated by a horizontal laser sheet of $200\text{--}300\mu\text{m}$ thickness. Initially undisturbed particles (a) were swept from left to right (by applying an electric pulse), forming a shock with a sharp front (b), (c). The lattice melted behind the front. At later times (d) the shock weakened due to the neutral drag and a soliton was formed. From Samsonov *et al.*, 2004.

Dispersion relations of dust modes in complex plasmas suggest that irrespective of the plasma state the phase velocity attains the maximal value in the long-wavelength limit. For acoustic modes this velocity (the “sound speed” C) is finite and therefore, similar to conventional media, the supersonic perturbations (i.e., with Mach number $M = V/C > 1$) are always localized behind the object which produces these perturbations (this can be a rapidly moving charged particle or a bunch of particles, biased probe, etc.). The perturbation front has a conical form in the 3D case and therefore it is called a “Mach cone.” In the 2D case the same name is adopted, although the front is a planar V-shaped perturbation. The opening angle μ of the front at large distances from the object (where the nonlinearity should not play an important role) is determined by the well-known relation $\sin \mu = C/V \equiv M^{-1}$.

In laboratory complex plasmas the Mach cones were generated in 2D plasma crystals by single particles spontaneously moving beneath the monolayer along straight trajectories (Samsonov *et al.*, 1999, 2000) or by the radiation pressure of a focused laser beam (Melzer *et al.*, 2000). The wake reveals a multiple cone structure behind the front, as shown in Fig. 6. Generally, the wake structure is determined by the dispersion and nonlinear properties of particular wave modes excited behind the front (Dubin, 2000; Zhdanov *et al.*, 2002; Nosenko *et al.*, 2003). The formation of the second cone (with smaller opening angle) behind the first one can be ascribed to the shear (transverse) wave front (Nosenko *et al.*, 2003; Nosenko, Goree, *et al.*, 2002) because the (longitudinal) sound speed is larger than the shear phase velocity. It was suggested that the Mach cones (wakes) can be excited in space dusty plasmas—e.g., in planetary rings by big boulders (Havnes *et al.*, 1995, 1996) moving through

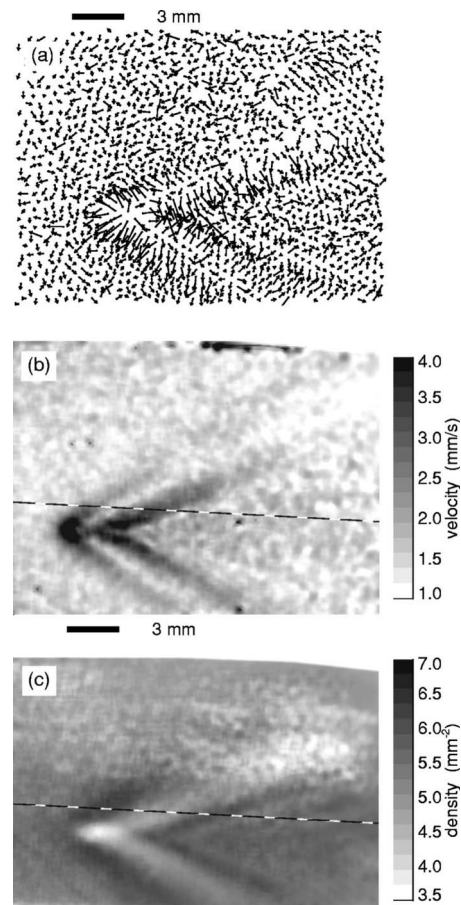


FIG. 6. Mach cone observed in a monolayer hexagonal lattice. Experiments were performed in krypton rf discharge at pressure 1.2 Pa, with particles of $8.9\mu\text{m}$ diameter. The cone was excited by a supersonic particle which moved spontaneously beneath the monolayer. (a) Particle velocity vector map, (b) gray-scale speed map, and (c) gray-scale number density map. From Samsonov *et al.*, 2000.

the dust at a velocity that is somewhat higher than the local sound speed. The observation of such Mach cones could be used for “long-distance diagnostics” of the conditions inside the rings.

E. Phase diagram

One fundamental characteristic of an interacting many-particle system is the coupling strength between particles. The coupling strength is measured in units of the potential energy of interaction between neighboring particles normalized by their mean kinetic energy. For a screened (short-range) Coulomb interaction the coupling strength is characterized by two parameters since the interaction has a length scale. These are the coupling parameter Γ determined by the magnitude of the bare Coulomb interaction and the screening parameter κ

$$\Gamma = Q^2/T_d\Delta, \quad \kappa = \Delta/\lambda, \quad (11)$$

where T_d characterizes mean kinetic energy (temperature) of the particles and λ is the appropriate screening

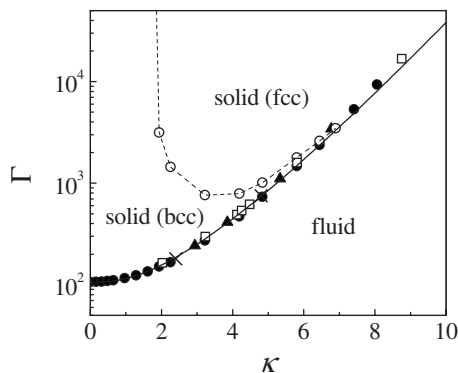


FIG. 7. Phase diagram of Debye-Hückel systems, obtained from numerical modeling. Open circles correspond to the bcc-fcc phase boundary (Hamaguchi *et al.*, 1997). The fluid-solid phase boundary (melting line) is marked by squares (Stevens and Robbins, 1993), solid circles (Hamaguchi *et al.*, 1997), and triangles (Meijer and Frenkel, 1991). The crosses correspond to jumps in the diffusion constant, observed in the simulations of dissipative Debye-Hückel systems (Vaulina and Khrapak, 2001; Vaulina *et al.*, 2002). The solid line represents the analytic approximation of the melting line, the dashed line is the fit to the numerical data judged by eye.

length (e.g., in isotropic plasmas $\lambda \approx \lambda_D$). The coupling strength is characterized by the screened coupling parameter $\Gamma_S = \Gamma \exp(-\kappa)$, and the system is usually called strongly coupled when $\Gamma_S \geq 1$. Note that the coupling parameter is related to the grain-grain scattering parameter β_{dd} introduced in Sec. II.C via $\beta_{dd} = \Gamma \kappa$.

Most theories developed so far to describe the properties of complex plasmas employ the following model: negatively charged particles are trapped within the plasma volume due to some confining force (usually of electrostatic character) and interact with each other via the isotropic Debye-Hückel (Yukawa) repulsive potential, with the screening determined by the plasma electrons and ions. This model gives a simplified picture of complex plasma behavior and is not applicable to some experiments, especially when the plasma anisotropy plays an important role (see Sec. II.B). Moreover, this model does not take into account variations of particle charges, long-range interactions, the exact form of the confining potential, etc. However, the model was shown to be useful in providing qualitative results which are confirmed by experiments, and hence it should be considered as a reasonable basis from which more sophisticated models might be constructed in future.

Besides complex plasmas, particles interacting with a Debye-Hückel potential have been extensively studied in different physical systems ranging from elementary particles to colloidal suspensions. Not surprisingly, their phase diagrams have received considerable attention. Various numerical methods (usually, MC or MD simulations) have been employed (Kremer *et al.*, 1986; Robbins *et al.*, 1988; Meijer and Frenkel, 1991; Stevens and Robbins, 1993; Hamaguchi *et al.*, 1997; Vaulina and Khrapak, 2001; Vaulina *et al.*, 2002). Figure 7 shows the phase diagram of the Debye-Hückel system in the (Γ, κ) plane,

summarizing available numerical results. For sufficiently strong coupling, $\Gamma > \Gamma_M$, where $\Gamma_M(\kappa)$ denotes the melting curve, there are solid fcc and bcc phases, whereas for $\Gamma < \Gamma_M$ the system is in a fluid state. The bcc phase is stable at small κ , while fcc is stable at larger κ . The triple point is at $\Gamma \approx 3.47 \times 10^3$ and $\kappa \approx 6.90$ (Hamaguchi *et al.*, 1997). The melting curve is given by $\Gamma_M e^{-\kappa(1 + \kappa + \frac{1}{2}\kappa^2)} \approx 106$ (Vaulina and Khrapak, 2000), which yields good agreement with the results of numerical simulations at $\kappa \leq 10$ (see Fig. 7).

There are different phenomenological criteria for the crystallization (melting), which are often practically independent of the exact form of the interparticle interaction, and therefore many of them are applicable to complex plasmas. Best known is the Lindemann criterion (Lindemann, 1910), according to which melting of the crystalline structure occurs when the ratio of the root-mean-square particle displacement to the mean interparticle distance reaches a value of ≈ 0.1 – 0.2 for 3D systems and ≈ 0.16 – 0.2 for 2D systems (Zheng and Earnshaw, 1998; Nunomura *et al.*, 2006; Saija *et al.*, 2006). Another criterion was suggested by Hansen and Verlet (1969) who observed that in 3D hard-sphere systems the first maximum of the static structure factor is ≈ 2.85 at the melting curve [for inverse-power-law interaction potentials $\propto r^{-n}$ this value varies in the range from ≈ 2.6 for $n=1$ to ≈ 3.0 for $n=12$ (Hansen and Schiff, 1973)]. For 2D systems, to our knowledge, this criterion has not been systematically tested so far. There also exists a crystallization criterion for the pair correlation function proposed by Raveche *et al.* (1974): For inverse-power-law interactions, the critical ratio of the first (non-zero) minimum to the first maximum lies in the range from ≈ 0.1 (for $n=1$) to ≈ 0.26 (for hard spheres). A simple dynamic crystallization criterion, similar to some extent to the Lindemann criterion, was proposed by Löwen *et al.* (1993). According to this criterion, crystallization occurs when the diffusion constant (normalized to $\Omega_E \Delta^2$) reduces below a certain value. This critical value depends on the dissipation ratio ν/Ω_E , and in the single-species (nondissipative) regime it has a distinct asymptote of ≈ 0.0032 (Ohta and Hamaguchi, 2000b; Vaulina *et al.*, 2002). This dynamical criterion holds for both 2D and 3D systems (Löwen, 1996).

F. New physics: Examples

1. Novel classes of non-Hamiltonian systems

So-called “open” systems are systems that may exchange energy and matter. These can be systems in contact with reservoirs, driven and constrained systems, etc. (Hoover, 1985; Evans and Morriss, 1990; Tuckerman *et al.*, 2001; Chakrabarti *et al.*, 2004). At the microscopic level, interactions between particles in such systems do not conserve the symmetry (invariants) peculiar to “closed” systems, and the use of Hamiltonian equations is not always useful to describe them. Since real systems should always be regarded, in some sense, as open, at both the microscopic and macroscopic levels, it may be

that non-Hamiltonian equations may provide a more realistic description of their behavior. One should note, however, that despite their ubiquity and importance, a fully consistent formulation of the statistical mechanics of non-Hamiltonian systems has never been presented.

A remarkable property of nonlinear open systems is the *self-organization* (Prigogine, 1980; Hasegawa, 1985)—a spontaneous emergence of stable spatial (or temporal) structures, which are often referred to as “dissipative structures,” since dissipation plays a constructive role in their formation. Dissipative structures are the manifestation of nonequilibrium phase transitions, with well-known examples being, the formation of convection (Bénard) or turbulent (Taylor) vortices (Cross and Hohenberg, 1993), or lane formation (Chakrabarti *et al.*, 2004) (see also Figs. 19 and 20). In order for such transitions to occur, three following basic requirements have to be satisfied: (i) Dissipation is necessary, to balance the external influx of energy. (ii) The structures may emerge only in systems described by nonlinear equations. (iii) There must be a relevant control parameter entering particular solutions of the equations, which ensures breaking of symmetry (*viz.*, transition) above a certain threshold.

Complex plasmas are non-Hamiltonian systems, not only because of conventional friction of grains against the background neutral gas, but also due to specific plasma interactions that give rise to new classes of non-Hamiltonian dynamics. Under certain conditions these interactions result in spontaneous excitation of individual and collective particle motion (Zhakhovski *et al.*, 1997; Morfill *et al.*, 1999; Vaulina *et al.*, 1999; Ivlev *et al.*, 2003; Morfill, Rubin-Zuzic, *et al.*, 2004). Next we consider a few examples of such dynamics.

a. Examples of non-Hamiltonian dynamics

i. Variable charges. Generally, the individual particle charges in complex plasmas fluctuate randomly with time around some equilibrium value which, in turn, is some function of the spatial coordinates (Fortov *et al.*, 2005).

The simplest class of non-Hamiltonian dynamics is realized when the charge is a function of the coordinates (Zhakhovski *et al.*, 1997), $Q = Q(\mathbf{r})$: The force $Q\mathbf{E}$ acting on a particle in a potential electric field $\mathbf{E}(\mathbf{r}) = -\nabla\varphi(\mathbf{r})$ cannot be expressed in terms of a gradient of a scalar function because $\nabla \times (Q\nabla\varphi) \equiv \nabla Q \times \nabla\varphi$ is not equal to zero in the general case. The dynamics is Hamiltonian only when the charge gradient is collinear with the electric field (in this case, the force depends on a single longitudinal coordinate and therefore it can always be written as a derivative of some scalar function over the coordinate). It is noteworthy that the nonpotential electrostatic force $Q\mathbf{E}$ is similar to the buoyancy force $T\mathbf{g}$ entering the Boussinesq equations, which drives free convection in conventional fluids [see Eq. (25)]: The local charge $Q(\mathbf{r})$ plays the role of the local fluid temperature $T(\mathbf{r})$, and the electric field the role of gravity \mathbf{g} . The experimentally observed vortices are well recovered in

numerical simulations (Vaulina *et al.*, 2000).

Another example is the so-called “delayed charging” effect (Nunomura *et al.*, 1999; Ivlev *et al.*, 2000; Pustyl'nik *et al.*, 2006), which stems from the fact that the charging frequency Ω_{ch} [see Eq. (2)] of a particle is finite. Therefore, the charge of a moving particle experiences some delay with respect to its equilibrium local value $Q(\mathbf{r})$ so that the dynamics is also non-Hamiltonian for 1D motion. Moreover, if $|Q(\mathbf{r})|$ increases along \mathbf{E} (which is always the case for particles levitating in ground-based experiments), then the absolute value of the *momentary* charge is smaller than $|Q(\mathbf{r})|$ when the particle moves along \mathbf{E} , and larger when the particle moves back. Thus, the work done over the oscillation period is always positive—the particle acquires energy from the electric field. The oscillations grow exponentially provided the energy gain is higher than the friction dissipation, which requires $2\nu_{\text{dn}} \lesssim (\ell_E/\ell_Z)\Omega_v^2/\Omega_{\text{ch}}$. Here $\ell_E = |E|/|\nabla E|$ and $\ell_Z = |Z|/|\nabla Z|$ are the spatial scales of the field and charge inhomogeneity, respectively (usually $\ell_E \ll \ell_Z$) and Ω_v is the eigenfrequency of the confined particle.

Now we consider random charge variations (fluctuations) assuming a constant equilibrium value Q (Vaulina *et al.*, 1999; Ivlev *et al.*, 2000). In experiments, the vertical particle confinement is usually determined by the balance of electrostatic and gravity forces $m_d g = QE$, and the equation of the vertical motion is determined by the charge fluctuation $Q_1(t)$,

$$\ddot{x} + \nu\dot{x} + \Omega_v^2[1 + Q_1(t)/Q]x = gQ_1(t)/Q. \quad (12)$$

Using the stochastic properties of the charge fluctuations [see Eq. (3)], it can be easily shown (Vaulina *et al.*, 1999) that for typical conditions $\nu \ll \Omega_v \ll \Omega_{\text{ch}}$ the mean energy of vertical oscillations associated with the random force at the right-hand side of Eq. (12) saturates at $\sim \sigma_Q^4 |Q/e| m_d g^2 / 2\nu\Omega_{\text{ch}}$, as it follows from the fluctuation-dissipation theorem (here σ_Q^2 is the relative dispersion of charge fluctuations, see Sec. II.A). In addition to this heating, the charge variations can trigger the parametric instability of the oscillations (Ivlev *et al.*, 2000), due to the random variations in the oscillation frequency in Eq. (12). Then the mean energy grows exponentially with time, similar to that in the case of delayed charges discussed above.

Spontaneous vertical oscillations of particles that can be caused by these mechanisms are ubiquitous in complex plasmas. For example, a drastic increase in vertical oscillations has been observed in the sheath of rf and dc discharges upon pressure decrease (Nunomura *et al.*, 1999; Misawa *et al.*, 2001; Pustyl'nik *et al.*, 2006). In some cases the energy of these oscillations exceeds room temperature by a few orders of magnitude.

For a set of particles, we have to define the mutual interactions. We again consider the role of spatial variations. The electrostatic potential created at \mathbf{r} by a charge located at \mathbf{r}_i is $\varphi_i(\mathbf{r}) = Q(\mathbf{r}_i)\varphi_{\text{unit}}(|\mathbf{r} - \mathbf{r}_i|)$, where $\varphi_{\text{unit}}(r)$ is the (isotropic) potential of a unit charge. The resulting electric field is $\mathbf{E}_i(\mathbf{r}) = -Q(\mathbf{r}_i)(\partial/\partial\mathbf{r})\varphi_{\text{unit}}(|\mathbf{r} - \mathbf{r}_i|)$. Hence, particles i and j interact via the force

$$\mathbf{F}_{ij} = -Q(\mathbf{r}_i)Q(\mathbf{r}_j)(\partial/\partial\mathbf{r}_i)\varphi_{\text{unit}}(|\mathbf{r}_i - \mathbf{r}_j|). \quad (13)$$

Note that the mutual interactions are reciprocal, $\mathbf{F}_{ij} = -\mathbf{F}_{ji}$, so that the total momentum of the system is conserved.

Principal features of non-Hamiltonian dynamics with interactions (13) can be understood by considering a 1D system of two charged grains which can move along the x axis (Zhdanov *et al.*, 2005). The repulsing particles have to be confined externally. Generally, the confinement is electrostatic and, hence, charge dependent. However, since electrostatic forces are potential in the 1D case, we can always write the confinement force on a particle as $F_{\text{conf}} = -dU_{\text{conf}}/dx$. We now introduce a 2D space $\mathbf{x} = (x_1, x_2)$, with $x_{1,2}$ the particle coordinates, and define the external confinement potential as $U_{\text{ext}}(\mathbf{x}) \equiv U_{\text{conf}}(x_1) + U_{\text{conf}}(x_2)$. Then the equations of two particle motion can be written in the following vector form:

$$m(\ddot{\mathbf{x}} + \nu\dot{\mathbf{x}}) = -\partial U_{\text{ext}}/\partial\mathbf{x} - Q_1Q_2(\partial\varphi_{\text{unit}}/\partial\mathbf{x}), \quad (14)$$

where $\varphi_{\text{unit}} = \varphi_{\text{unit}}(|x_2 - x_1|)$ and $Q_{1,2} \equiv Q(x_{1,2})$. In addition to the confinement and interaction forces, we introduced a friction force with the damping rate ν . One can see from Eq. (14) that the 1D dynamics of two particles is mathematically identical to 2D dynamics of a single particle. The dynamics is *nonconservative* because work W_{loop} done (due to mutual interactions) over a closed path (loop) ℓ in plane \mathbf{x} is not equal to zero. Using Stokes theorem, the work can be expressed via the integral over the surface S_ℓ bounded by the path

$$W_{\text{loop}} = \int_{S_\ell} (Q_1Q_2' + Q_1'Q_2)\varphi_{\text{unit}}' dx_1 dx_2,$$

where the prime denotes the derivative with respect to the argument.

The sign of W_{loop} is determined by the direction of motion along ℓ , i.e., the charge variations can serve as either a sink ($W_{\text{loop}} < 0$) or a source ($W_{\text{loop}} > 0$) of the energy. In the latter case the motion of interacting particles can be unstable. In dissipative systems one can expect that at the nonlinear stage motion converges asymptotically to a limit cycle, with the balance between the energy gain and frictional loss, $W_{\text{loop}} - 2\nu\tau\langle K \rangle = 0$, where τ is the oscillation period and $\langle K \rangle$ is the mean kinetic energy averaged over τ . We see that the magnitude of the work done over path ℓ is determined by the area S_ℓ . This implies that when $\nu \rightarrow 0$ the contour ℓ of periodic motion (if such motion is possible at all) should degenerate into some line, so that S_ℓ tends to zero as well.

The non-Hamiltonian dynamics of many particles with variable charges can be investigated using numerical MD simulations (Zhdanov *et al.*, 2005). The simplest case is the 2+2 particle system, where two outer particles are fixed and two inner particles are movable. Particles interact via the Yukawa potential $\varphi_{\text{unit}}(x) = e^{-x/\lambda}/x$ with the screening length λ , and the spatial dependence of the charge is given by a stepwise function $\propto \tanh[(x - x_{\text{jump}})/\sigma_{\text{jump}}]$ varying along the x axis by the magnitude

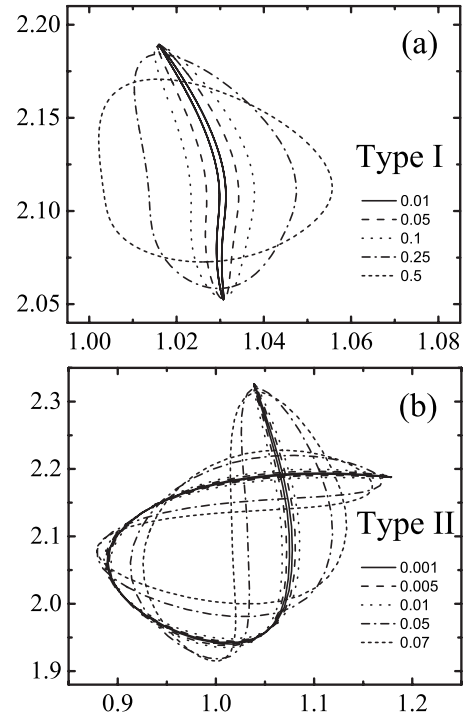


FIG. 8. “Mutual” phase portraits of self-excited particle oscillations triggered by spatially varying charges. Two particles perform a 1D motion, their coordinates (x_1, x_2) form periodic trajectories that are shown for several values of damping rate, the highest values are chosen in the vicinity of the self-excitation cutoff. By varying initial momentums of the particles, one can obtain attractors of type I (a) or II (b). Coordinates are measured in units of the screening length λ and the damping rate is normalized by the frequency scale $\sqrt{Q^2/m\lambda^3}$. Adapted from Zhdanov *et al.*, 2005.

ΔQ , where x_{jump} is the position of the charge “jump” and $\sigma_{\text{jump}} \ll x_{\text{jump}}$ is the width of the jump. The initial interparticle distance Δ is determined from the equilibrium condition. It was found that spontaneous oscillations set in when the magnitude of the charge gradient exceeds a certain threshold: When the initial (equilibrium) coordinates of the particles are relatively far from x_{jump} (a few σ_{jump}), which implies relatively weak charge variations, the oscillations decay and the mean kinetic energy falls off as $\propto e^{-2\nu t}$. When the initial position of one of the particles is sufficiently close to x_{jump} (about σ_{jump} or less), so that the charge variations are strong enough, the kinetic energy does not decay. On the contrary, $\langle K \rangle$ eventually saturates at a constant level and the oscillations become periodic, converging asymptotically to the attractors shown in Fig. 8. Varying initial conditions it was found that two different types of attractor are possible, either type I [Fig. 8(a)] or type II [Fig. 8(b)], with no regular correspondence to the initial conditions (e.g., initial particle momenta). One can see that the oscillation contours become narrower and have a tendency to degenerate into a single line as the damping rate ν decreases. On the other hand, there exists a critical friction beyond which self-sustaining oscillations are no longer possible. The width and length of the oscillation con-

tours at the critical ν are roughly the same, indicating that the area S_ℓ of the contour is about to achieve its maximum.

ii. *Plasma wakes.* Another class of non-Hamiltonian dynamics occurs when charged grains (we assume for simplicity that the charges are constant) are embedded in a flowing plasma, with ions moving relative to grains due to, e.g., ambipolar diffusion. The screening cloud around a charged grain is no longer spherically symmetric, which gives rise to higher (dipole, quadruple, etc.) moments in the mutual interaction. As discussed in Sec. II.B, the screening cloud in this case is usually referred to as a “plasma wake,” instead of the “Debye sphere” in the isotropic case. One should point out the fact that in some cases the mathematical description of wakes is identical to the equations describing, e.g., hydrodynamic interactions of bubbles in conventional fluid flows (Beatus *et al.*, 2006).

In order to understand the dynamics of such systems, one should note that complete ensembles of elementary charges in complex plasmas can be conveniently subdivided into two distinct categories: a subsystem of bound charges at the grain surface and a subsystem of free plasma charges in the surrounding wakes. Plasma wakes play the role of a “third body” in the mutual grain-grain interaction and, hence, make the pair interaction *nonreciprocal* (Melzer *et al.*, 1999): The force exerted by a wake of grain 1 on grain 2 is generally not equal to the force of wake 2 acting on grain 1. Thus, in contrast to the case of variable charges, the total particle momentum is no longer conserved. The center-of-mass motion is governed by (Kompaneets, 2007)

$$m(\ddot{\mathbf{r}}_c + \nu \dot{\mathbf{r}}_c) = \frac{1}{2} Q (\partial/\partial \mathbf{r}_r) [\varphi(-\mathbf{r}_r) - \varphi(\mathbf{r}_r)] + \mathbf{F}_{\text{ext}}. \quad (15)$$

Here $\mathbf{r}_c = \frac{1}{2}(\mathbf{r}_1 + \mathbf{r}_2)$ and $\mathbf{r}_r = \mathbf{r}_2 - \mathbf{r}_1$ are the center-of-mass and relative coordinates, respectively, and $\varphi(\mathbf{r}_r)$ [$\neq \varphi(-\mathbf{r}_r)$] is an anisotropic wake potential [see Eq. (6)]. In addition to the mutual interactions, in Eq. (15) we introduced a force \mathbf{F}_{ext} which describes the interaction of grains with a (constant) external electric field (assuming constant charges, this field may be presented as a gradient of some scalar function). Equation (15) shows that one can easily construct such a loop ℓ for the motion of the center of mass that the work W_{loop} done by the nonreciprocal interaction over the loop is not equal to zero,

$$W_{\text{loop}} \propto \int_{S_\ell} (\partial/\partial \mathbf{r}_c) \times (\partial/\partial \mathbf{r}_r) [\varphi(-\mathbf{r}_r) - \varphi(\mathbf{r}_r)] dS_\ell.$$

This occurs when \mathbf{r}_c and \mathbf{r}_r are correlated (e.g., due to resonances) so that $(\partial/\partial \mathbf{r}_c) \times (\partial/\partial \mathbf{r}_r) \neq 0$ and the dynamics of interacting particles is not conserved.

Such nonconservative dynamics results in spontaneous heating of complex plasmas. As an example, we consider recent experiments on melting of a crystalline monolayer (Ivlev *et al.*, 2003). The microparticles were levitated in the strong vertical electric field of the sheath above a planar rf electrode and confined horizontally by

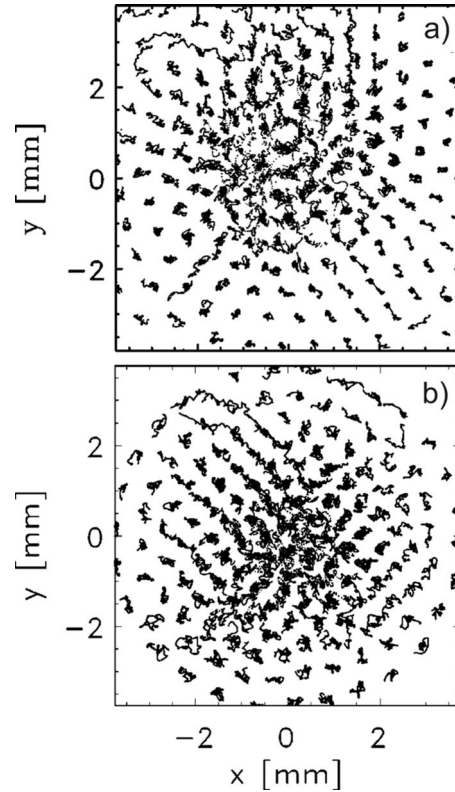


FIG. 9. Melting of 2D crystal. (a) Top view of the particle monolayer in the experiment with $8.9 \mu\text{m}$ particles in argon at pressure of 2.8 Pa. The particles are in the crystalline state, until the density exceeds a certain threshold and the monolayer melts. Trajectories over 3.1 s after the melting starts. (b) Top view of the particle monolayer in the MD simulation with parameters similar to the experiment. In both cases, the average kinetic energy of particles in the center saturated at ~ 30 eV. From Ivlev *et al.*, 2003.

a weak radial field. When the number of particles in the monolayer exceeded a certain threshold (correspondingly, the interparticle distance decreased, with the smallest distance in the center due to the radial confinement) the monolayer started melting, from the center to the periphery. The horizontal particle trajectories during the melting process are shown in Fig. 9(a). Simultaneously, oscillations in vertical direction were triggered. It was possible to stop the melting by increasing the pressure—the system always returned to a stable crystalline monolayer.

The experiment was simulated using a MD code which contains a first-principles representation of the short-range shielded Coulomb forces and the wake forces due to the streaming ions. In the numerical simulations the basic findings of the experiment could be reproduced: When the number of particles in the simulation exceeded a certain threshold, the monolayer melted. In such unstable cases the interparticle distance in the center of the monolayer was close to the experimentally measured values. The melting developed in a manner similar to the experiment [see Fig. 9(b)]. With increasing pressure (neutral friction) the system became stable. Finally, when the particle interaction was reduced

to a spherically symmetric potential (without wakes) the system was always stable, indicating that the wakes play the decisive role in the melting.

Quantitative conditions for the melting onset can be derived from the following simple model (Ivlev and Morfill, 2001): Negatively charged particles of charge Q and mass m are separated horizontally by a distance Δ and interact via a (spherically symmetric) screened potential. The excess positive charge of the wake q is approximated by a pointlike charge located at distance δ downstream from the particle. Vertically, the particles are confined in a potential well with their eigenfrequency Ω_v . It is known that in a crystalline monolayer, in addition to conventional in-plane acoustic modes (dust-lattice waves, see Sec. II.D), there also exists an out-of-plane optical mode associated with vertical particle oscillations (Samsonov *et al.*, 2005). The in-plane (\parallel) and out-of-plane (\perp) modes are coupled due to the particle-wake interaction. The coupling is weak when the branches $\omega_{\parallel}(k)$ and $\omega_{\perp}(k)$ are far away from each other, but becomes strong at the resonance, when they intersect. This happens when the number density of particles exceeds a threshold. Then the branches are modified and form a hybrid branch in the vicinity around the intersection point, where the resonance coupling can drive an instability with the growth rate

$$\text{Im } \omega \approx |q\delta/Q\Delta|(\Omega_0^2/\Omega_v) - \nu, \quad (16)$$

where $\Omega_0 = \sqrt{Q^2/m\Delta^3} \approx \Omega_{pd}$. One can see from Eq. (16) that the coupling part is proportional to the dipole moment of the wake $q\delta$ and the instability is suppressed when the damping is sufficiently high. It is remarkable that such a simple model not only recovers all qualitative features seen in the experiment, but also gives good (within $\approx 5\%$) quantitative agreement.

An additional mechanism contributing to the mode coupling can be due to spatial charge variations and/or variations in the screening, and this effect might significantly affect the instability (Kompaneets *et al.*, 2005; Yarovshenko *et al.*, 2005). Note that the non-Hamiltonian dynamics of dust grains due to nonreciprocity of the particle-wake interactions (and/or charge-screening variations) can also cause melting of 3D crystals (Melzer, Schweigert, *et al.*, 1996).

To conclude, it is worth mentioning yet another type of collective instability triggered by charge variations (Fortov *et al.*, 2000, 2003; Zobnin *et al.*, 2002). According to Eq. (9), charged microparticles in 3D complex plasmas affect the volume charge composition, so that the electron-to-ion density ratio varies with the dust density n_d . This, in turn, disturbs the balance between electron and ion fluxes to the grain and hence Q becomes a function of n_d . This effect can cause instability of the DA wave (see Sec. II.D) propagating in a plasma with an external electric field: The wave-correlated charge variations result in nonzero (average) work done by the electric force, and the sign of this work is determined by the orientation of the wave vector with the respect to the electric field. Such an instability is triggered when the

density of dust particles exceeds a critical value.

b. Kinetics of particles with variable charges

Since ensembles of particles with variable charges are generally non-Hamiltonian systems, the use of thermodynamic potentials to describe them is not really justified. An appropriate way to investigate the evolution of such systems is to use the kinetic approach (Ivlev *et al.*, 2004; Ivlev, Zhdanov, Klumov, and Morfill, 2004). As long as properties of the charge variations are known, one can consider the dynamics and kinetics of the grains independently from the plasma kinetics.

i. Kinetic equation. In the absence of external fields, the kinetics of charged grains is governed by the mutual collisions and collisions with neutrals, so that the kinetic equation is

$$df/dt = \text{St}_d f + \text{St}_n f. \quad (17)$$

The grain-neutral collision integral does not depend on particle charges and can be written in the usual Fokker-Planck form (equivalent to the Langevin equation).

As regards the grain-grain collisions (here we investigate dilute gaseous ensembles and hence focus on the binary interactions only), one should note one important point (Ivlev, Zhdanov, Klumov, and Morfill, 2005): Generally, we cannot use the collision integral in the classical Boltzmann form, because its derivation employs the unitarity relation (Lifshitz and Pitaevskii, 1981). This relation is not necessarily satisfied for ensembles with variable charges: Naturally, the grain-grain collision integral applies only for those transitions occurring (between different kinetic states) in the subsystem of charged grains. Due to the exchange of energy with free plasma charges, the subsystem of grains is not conservative—the momentum exchange during a collision is affected by the charging processes. Therefore the unitarity relation can be fulfilled only after the summation over the complete set of states, including those corresponding to the subsystem of the plasma charges. Thus, we have to write the collision integral in the most general form,

$$\begin{aligned} \text{St}_d f(\mathbf{p}) = & \int [w(\mathbf{p}', \mathbf{p}'_1; \mathbf{p}, \mathbf{p}_1) f(\mathbf{p}') f(\mathbf{p}'_1) \\ & - w(\mathbf{p}, \mathbf{p}_1; \mathbf{p}', \mathbf{p}'_1) f(\mathbf{p}) f(\mathbf{p}_1)] d\mathbf{p}_1 d\mathbf{p}' d\mathbf{p}'_1. \end{aligned} \quad (18)$$

Here $w(\mathbf{p}, \mathbf{p}_1; \mathbf{p}', \mathbf{p}'_1)$ is a probability function for a pair of colliding particles with momenta \mathbf{p} and \mathbf{p}_1 to acquire momenta \mathbf{p}' and \mathbf{p}'_1 , respectively, after the scattering. Equation (18) accounts for all possible transitions $(\mathbf{p}', \mathbf{p}'_1) \rightarrow (\mathbf{p}, \mathbf{p}_1)$ (sources) and $(\mathbf{p}, \mathbf{p}_1) \rightarrow (\mathbf{p}', \mathbf{p}'_1)$ (sinks), and then is averaged over \mathbf{p}_1 . The function w can be determined by solving the mechanical problem of the binary scattering with a given interaction between particles.

The mechanics of binary grain collisions can be conveniently considered in terms of the center-of-mass and relative coordinates. (Below we consider grains of the same mass, although all results can be straightforwardly generalized for an arbitrary mass ratio.) For a pair of

particles with momenta \mathbf{p} and \mathbf{p}_1 , the center-of-mass and relative momenta are $\mathbf{p}_c = \frac{1}{2}(\mathbf{p} + \mathbf{p}_1)$ and $\mathbf{p}_r = \mathbf{p}_1 - \mathbf{p}$, respectively. In the absence of external forces, the center-of-mass momentum is conserved, and the relative momentum is changed during the collision,

$$\mathbf{p}'_c = \mathbf{p}_c, \quad \mathbf{p}'_r = \mathbf{p}_r + \mathbf{q}. \quad (19)$$

For constant charges, the absolute value of the relative momentum, $p_r \equiv |\mathbf{p}_r|$, is conserved, and only the direction changes (elastic scattering) (Landau and Lifshitz, 1976). Charge variations also cause p_r variations (Ivlev, Zhdanov, Klumov, and Morfill, 2005). Hence, the exchange of the relative momentum can be divided into elastic and inelastic parts, $\mathbf{q} = \mathbf{q}_0 + \delta\mathbf{q}$: The elastic part keeps the magnitude of the relative momentum constant, $|\mathbf{p}_r + \mathbf{q}_0| = p_r$. The vector of inelastic momentum exchange $\delta\mathbf{q}$ is parallel to \mathbf{p}'_r , and its magnitude is $\delta q = p'_r - p_r$.

The kinetics of particles with variable charges has an important hierarchy of time scales (Ivlev, Zhdanov, Klumov, and Morfill, 2005): Each interparticle collision is accompanied by (i) elastic momentum exchange \mathbf{q}_0 , which provides the relaxation of the distribution function to the Maxwellian equilibrium (Lifshitz and Pitaevskii, 1981) while keeping the mean kinetic energy of the particles E constant: and (ii) inelastic momentum exchange $\delta\mathbf{q}$, which causes variation in E . Due to the relative smallness of the charge variations, the resulting inelastic momentum exchange is small as well, $\delta q \ll q_0$. This implies that process (ii) is much slower than process (i). Therefore, the velocity distribution remains close to the Maxwellian form, $f(\mathbf{p}) \approx f_M(\mathbf{p})$, with the temperature $T = \frac{2}{3}E$ (Landau and Lifshitz, 1978).

Thus the temperature is the only parameter that determines the evolution of the ensemble. This implies that the system can be treated with fluid equations: The momentum equation [with the friction force $-\nu\mathbf{v}$ added, see Eq. (25)] remains unaffected since the charge variations conserve the net momentum. The equation for temperature $T = \int (p^2/3m) f d\mathbf{p}$ acquires a new source term due to charge variations, in addition to the sink term due to friction. In accordance with Eq. (17), these terms are determined by

$$\dot{T} = \int (p^2/3m) (St_d f + St_n f) d\mathbf{p}. \quad (20)$$

For the grain-neutral collisions the integral is $-2\nu(T - T_n)$. For the grain-grain collisions, one can expand the integrand into a series over δq . Retaining the linear and quadratic terms and integrating in parts, we obtain (Ivlev, Zhdanov, Klumov, and Morfill, 2005)

$$\int p^2 St_d f d\mathbf{p} \approx \frac{1}{2} \int (p_r \mathcal{A} + \mathcal{B}) f_M(\mathbf{p}_c) f_M(\mathbf{p}_r) d\mathbf{p}_c d\mathbf{p}_r, \quad (21)$$

where $\mathcal{A}(\mathbf{p}_c, \mathbf{p}_r) = \int \delta q \tilde{w} d\delta q$ and $\mathcal{B}(\mathbf{p}_c, \mathbf{p}_r) = \frac{1}{2} \int (\delta q)^2 \tilde{w} d\delta q$ are the Fokker-Planck coefficients (van Kampen, 1981; Lifshitz and Pitaevskii, 1981), $\tilde{w}(\mathbf{p}_r, \mathbf{p}_c; \delta q)$

$\equiv w(\mathbf{p}, \mathbf{p}_1; \mathbf{p}', \mathbf{p}'_1)$, and the momenta are related by Eq. (19). The smallness of coefficients \mathcal{A} and \mathcal{B} is ensured by the smallness of the charge variations (for constant particle charges, the inelastic momentum exchange is equal to zero and hence $\mathcal{A} = \mathcal{B} = 0$).

ii. *Heating*. Irrespective of which type of charge variations plays the major role (charge inhomogeneity or fluctuations) the interparticle interaction can be distinguished in terms of the interaction strength: For particles interacting via a short-range screened electrostatic potential (with the screening length λ), the measure of the interaction strength is the scattering parameter $\beta_{dd} = Q^2/\lambda T$ (see Sec. II.C). When β_{dd} is large enough, the interaction is of the hard-spheres type. In the opposite case, when the ratio is small, the interaction is of the Coulomb type, similar to that between electrons and ions in usual plasmas. Below these two limits are referred to as the low-temperature and high-temperature regimes, respectively, with the transition temperature given by $T_{tr} = Q^2/\lambda$. Equations (20) and (21) result in the following equation for the particle temperature (Ivlev, Zhdanov, Klumov, and Morfill, 2005):

$$\dot{T} \sim \alpha T^\gamma - 2\nu(T - T_n). \quad (22)$$

The coefficient α and exponent γ in the source term depend on the temperature regime. In the case of inhomogeneous charges, the exponent is $\gamma = 3/2$ for $T \ll T_{tr}$ and $\gamma = 1/2$ for $T \gg T_{tr}$, respectively. We see that in the low-temperature regime the temperature exhibits an explosionlike growth provided the friction rate ν is low enough. At higher temperatures, however, the growth is always saturated [see Fig. 10(a)]. For the fluctuating charges we have $\gamma = 2$ and $\gamma = 1$ for the low- and high-temperature regimes, respectively. This means that, unlike the case of inhomogeneous charges, the temperature does not saturate but can grow exponentially at $T \gg T_{tr}$ [see Fig. 10(b)]. Numerical MD simulations fully support the theoretically predicted scalings.

2. Charge-induced runaway coagulation

Coagulation (or aggregation, clustering) is important for various processes in different branches of physics and chemistry, for instance polymerization (Flory, 1953), transitions in colloidal systems (Jullien and Botet, 1987), plasma etching (Boufendi and Bouchoule, 1994), planet formation (Lissauer, 1993), etc. In many cases coagulation can be considered as an irreversible process of cluster merging due to the pair interaction of smaller clusters (Meakin, 1991). Different aspects of the aggregation theory for uncharged systems were studied in detail in the last two decades (see, e.g., Ernst, 1986; Meakin, 1991; Kempf *et al.*, 1999, and references therein).

Experimental study of coagulation in a cloud of micron-size particles embedded in a rarefied neutral gas is important for understanding the nature of the coagulation process (Blum *et al.*, 2000). During a recent series of the PKE-Nefedov experiments (Nefedov *et al.*, 2003) performed onboard the International Space Station

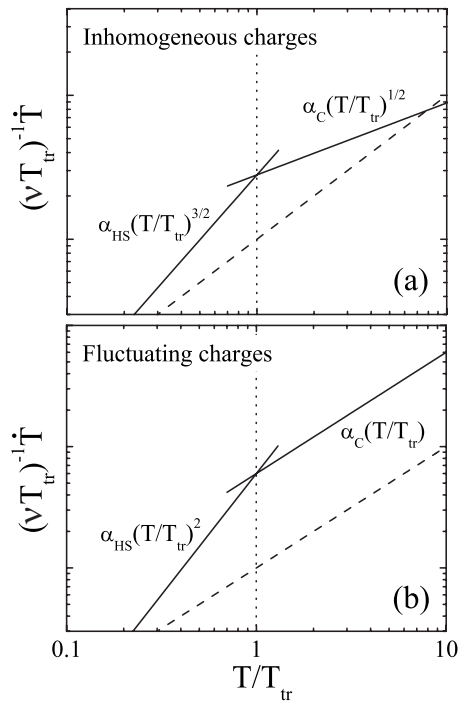


FIG. 10. Self-heating in a system of particles with variable charges. Asymptotic behavior of the particle kinetic temperature is shown for (a) inhomogeneous charges and (b) fluctuating charges. The transition temperature T_{tr} separates the hard-sphere (low-temperature, $T \ll T_{tr}$) and Coulomb (high-temperature, $T \gg T_{tr}$) collisional regimes. Solid lines correspond to the source (charge variation) term in Eq. (22), α_{HS} and α_C denote coefficients for the hard-spheres and Coulomb regimes, respectively. Dashed line correspond to the friction term. From Ivlev, Zhdanov, Klumov, and Morfill, 2005.

(ISS), the coagulation of micron-size monodisperse particles was investigated in a neutral gas under microgravity (Ivlev *et al.*, 2002; Konopka *et al.*, 2005). In several experimental runs up to $\sim 10^6$ microparticles were injected into the chamber filled with neutral gas. The mass spectrum of the resulting particle clusters (number of clusters n and accumulating mass m) was measured. When the number density of injected particles was small $n(m)$ had a cutoff, as shown in Fig. 11(b) and particles coagulated homogeneously throughout the chamber volume. The results changed dramatically when the number density exceeded a certain threshold: In this case, $n(m)$ had no apparent cutoff at large m but exhibited a power-law tail [see Fig. 11(a)]. Simultaneously, the growth of a single large agglomerate occurred, accumulating $\sim 10^4$ – 10^5 particles in a few seconds. The coagulation process developed many orders of magnitude faster than was expected. A large agglomerate was formed while the aggregation among smaller clusters was still going on.

It is well known that in some systems of particles with ongoing coagulation a special kind of phase transition called “gelation” is possible (see, e.g., Ernst, 1986; Lee, 2000, and references therein). At a certain gelation moment, t_{gel} the ensemble becomes unstable against the

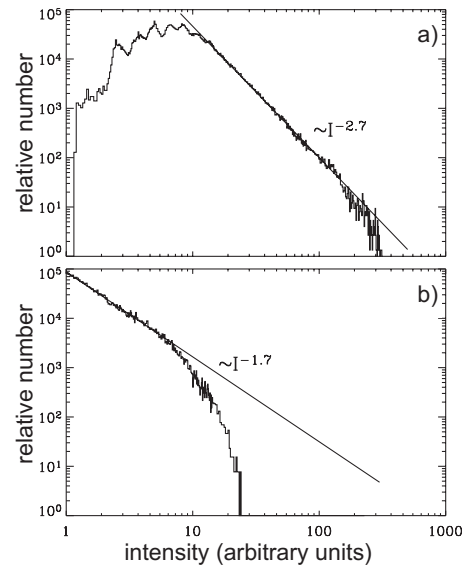


FIG. 11. Spectra of coagulated clusters. Intensity spectrum of clusters deduced from images taken shortly after the injection of (a) large and (b) small number of microparticles ($3.4 \mu\text{m}$ diameter). The reflected light intensity I , of coagulated clusters reveals a power-law intensity distribution function. Considering clusters as fractal aggregates, the high-mass part of the mass spectrum can be retrieved from the intensity distribution ($I \propto m^{2/D_f}$, where D_f is the fractal dimension). The “runaway” aggregates that are formed (a) are detached from the shown smooth spectrum and contain up to $\sim 10^5$ microparticles. From Konopka *et al.*, 2005.

formation of a single cluster of infinite mass. This process is also called “runaway growth.” The gelation develops if the coagulation rate increases sufficiently steeply with the mass. Mathematically, this is because at $t = t_{gel}$ the distribution function for such kernels is no longer bounded exponentially at the high-mass end, but scales as $n(m, t_{gel}) \propto m^{-\tau}$ with $2 < \tau < 3$. The total mass of the finite size clusters is not conserved in this case, but there is a nonzero mass flux at $m \rightarrow \infty$, which causes the formation of the infinite gel particle. The gel particle therefore accumulates a mass comparable with the total mass of the system so that the mass dispersion diverges. One can see that the essential features peculiar to the gelation transition were observed in coagulation experiments with charged particles (Konopka *et al.*, 2005).

Further investigation of the experimental data (Konopka *et al.*, 2005) showed that the clusters were charged, positively or negatively, with no detectable overall charge preponderance. The charge magnitude of individual clusters was at least a few thousand electron charges. The charging processes in neutral gases are very different from those in plasmas, where the charging is due to the absorption of electrons and ions and the charge of the cluster is a certain function of the size (see Sec. II.A). In a neutral gas, by contrast, the external sources of charging are absent and the total (initial) charge of the system is conserved.

The role of charge-induced interactions in the coagulation process was analyzed by Ivlev *et al.* (2002), who

proposed a theory of pair clustering in conservative charged systems. The simplest mean-field approach to describe the aggregation process is to generalize the Smoluchowski coagulation equation (Smoluchowski,

1917) for the case of two independent variables: the cluster mass m and the charge Q . Then the kinetic (coagulation) equation for the distribution function of clusters $n(m, Q, t)$ can be written in the following form:

$$\begin{aligned} \frac{\partial}{\partial t} n(m, Q, t) = & \frac{1}{2} \int_0^m dm' \int_{-\infty}^{\infty} dQ' K(m', Q'; m - m', Q - Q') n(m - m', Q - Q', t) n(m', Q', t) \\ & - n(m, Q, t) \int_0^{\infty} dm' \int_{-\infty}^{\infty} dQ' K(m', Q'; m, Q) n(m', Q', t), \end{aligned} \quad (23)$$

where $K(m', Q'; m, Q)$ is the coagulation rate coefficient (kernel) or the probability for a pair of clusters, (m', Q') and (m, Q) , to merge. The kernel is obviously symmetric with respect to the pair exchange, $K(m', Q'; m, Q) = K(m, Q; m', Q')$, and at large m and $|Q|$ it has algebraic asymptotics. The kernel is averaged over the velocity distribution $K(m', Q'; m, Q) = \langle v_r \sigma(a', Q'; a, Q; v_r) \rangle$, where $v_r = |\mathbf{v} - \mathbf{v}'|$ is the relative velocity of the clusters. When clusters are in thermal equilibrium with an ambient gas we have the equipartition velocity dispersion $\langle v_r \rangle \propto m_*^{-1/2}$, with $m_* = mm'/(m + m')$ the reduced mass of the pair. The merger cross section σ is a function of the effective aggregate radius a . The explicit relation between a and m is given by the appropriate scaling law with fractal dimension D_f , i.e., $m \propto a^{D_f}$ (Meakin, 1991). For different aggregation processes the fractal dimension can vary from $D_f \approx 3$ (dense or compact clusters) down to ≈ 1.4 – 1.5 [fluffy aggregates, see Meakin (1991) and Kempf *et al.* (1999)]. Note that the coagulation equation can be written in a discrete form as well [Ernst (1986), for instance, to resolve the low-mass and low-charge distribution], and then the summation should be used in Eq. (23). However, the continuous form (23) is more convenient and quite sufficient because at large m (and $|Q|$) the summation can be replaced by the integration.

Obtaining exact solutions of the coagulation equation is not a simple task even in the charge-independent case. The solutions with arbitrary initial conditions are known only for a few types of the kernel (e.g., $K = \text{const}$, $\propto m + m'$, and $\propto mm'$) (Ernst, 1986). The asymptotic solutions for the high mass tail are also known for $K \propto m^\mu m'^\nu$ (with $\max\{\mu, \nu\} \leq 1$). No analytic solutions are known for the charge-dependent kernels. However, the major features of the aggregation process can be understood by analyzing moments of the distribution function, $M_{i,j}(t) = \int dm \int dQ m^i Q^j n(m, Q, t)$ (e.g., $M_{1,0}$ and $M_{0,1}$ are the total mass and charge, respectively). Equations for $M_{i,j}(t)$ are derived by multiplying Eq. (23) with $m^i Q^j$ and integrating over m and Q .

A major contribution to the charge-induced interparticle interaction and hence to the merger cross section is

provided by the charge-charge and charge-dipole (induced) interactions, $U_{\text{ch}} \propto r^{-1}$ and $U_d \propto r^{-4}$, respectively (Ivlev *et al.*, 2002). The long-range charge-charge interaction works selectively—it enhances coagulation when clusters are oppositely charged and inhibits it otherwise. The analysis performed for U_{ch} shows that, although the resulting coagulation rate is enhanced by a factor of $\sim \langle Q^2 a^{-1} \rangle / T_d$ (which can be as large as $\sim 10^3$ at the initial stage of the coagulation), the mean cluster mass does not grow with time faster than linearly and therefore U_{ch} alone cannot trigger the observed anomalously rapid aggregation. On the other hand, the charge dispersion $\langle Q^2 \rangle$ decreases with time due to the charge-charge enhanced coagulation (we assume $\langle Q \rangle = 0$, as observed in experiments), while the average cluster size $\langle a \rangle$ increases. Therefore, eventually $\langle Q^2 a^{-1} \rangle$ becomes smaller than T_d and the induced charge-dipole interaction prevails. Since U_d is attractive irrespective of the charge sign, the resulting coagulation is always enhanced. The corresponding coagulation rate can be expressed as $K(m', Q'; m, Q) = m^\mu m'^\nu |Q'|^\varepsilon + m'^\mu m^\nu |Q|^\varepsilon$, where $1 \leq \varepsilon \leq 2$ is the charge exponent and the values of mass exponents μ and ν ($\mu + \nu \equiv \lambda$) can be obtained from the asymptotic behavior of the general expression for K in the limit $a/a' \gg 1$ (Ernst, 1986). Analysis shows that the charge-dipole interaction can relax the condition for gelation dramatically. The resulting equations for $M_{i,j}(t)$ yields the following gelation condition (Ivlev *et al.*, 2002):

$$\lambda + \frac{1}{2} \varepsilon > 1, \quad (24)$$

in contrast to $\lambda > 1$ for the charge-free case (Ernst, 1986; Lee, 2000).

We compare the gelation conditions for the charge-dipole and pure geometrical coagulation. Equation (24) shows that in the presence of charge-induced interactions the kernel need not necessarily be a steep function of mass—for the charge exponent $\varepsilon = 2$ the mass exponent λ is sufficient to be just positive. Smaller λ implies higher values of the fractal dimension D_f of clusters. Using Eq. (24) we get the critical D_f which are necessary to start the gelation: For charge-dipole coagulation with ε

$=2$ we have $\lambda = D_f^{-1} - \frac{1}{2}$, and the gelation condition is $D_f < 2$; with $\varepsilon=1$ we have $\lambda = \frac{3}{2}D_f^{-1} - \frac{1}{2}$, and $D_f < \frac{3}{2}$. In contrast, for geometrical coagulation we have $\lambda = 2D_f^{-1} - \frac{1}{2}$, and the gelation is possible for $D_f < \frac{4}{3}$.

Clusters produced due to Brownian motion are very fragile and fluffy, with an average value of the fractal dimension of $\approx 1.8-2$ (Kempf *et al.*, 1999). Therefore the charge-induced gelation of thermal clusters is quite likely, whereas the occurrence of gelation due to geometrical coagulation is practically impossible because too low values of D_f are necessary for that.

III. KINETIC STUDIES OF LIQUIDS AND SOLIDS WITH COMPLEX PLASMAS

As a starting point, we consider the following question: How relevant are liquid or solid plasmas to study classic phenomena in conventional condensed media? The implication is clear—if they are relevant, we have opened up a completely new kinetic approach, which will then have a major impact in a field of great future potential. As pointed out in the introduction, one interesting aspect of strongly coupled complex plasmas is that although they are intrinsically multispecies systems, the rate of momentum exchange through mutual (electrostatic) interactions between microparticles can exceed that of interactions with the background neutral gas significantly—thus providing an essentially single-species system for kinetic studies. Moreover, comparison in terms of similarity parameters (e.g., Reynolds, Rayleigh, or Weber numbers for fluids) suggests that liquid complex plasmas can be like conventional liquids (e.g., water)—but observed at the atomistic level.

Because of these unique properties, complex plasmas can indeed serve as a powerful new tool for investigating fluid flows on (effectively) nanoscales, including the all-important mesoscopic transition from collective hydrodynamic behavior to the dynamics of individual particles, as well as nonlinear processes on scales that have not been accessible for studies so far. Of particular interest could be kinetic investigations of the onset and nonlinear development of hydrodynamic instabilities. Individual particle observations can provide crucial new insights—e.g., whether the coarse-grained concept of basic hydrodynamical instabilities (Kelvin-Helmholtz, Rayleigh-Taylor, Richtmyer-Meshkov, etc.) is still adequate on interparticle distance scales, whether there are any microscopic origins of instabilities (in particular, what are the trajectories that can trigger instabilities), etc. Another important issue is the atomistic structure and dynamics of fluids—in particular, what are the critical changes that occur in the (atomic) structure of solids that give them the ability to flow, are there any characteristic patterns in microscopic dynamics associated with that transition, what are the conditions to form supercooled liquids and glassy states, etc.

Regarding the solid phases, the current interest where highly resolved dynamical measurements in complex plasmas may bring significant advances lies in domain

boundaries and defects—associated with excited crystal lattice states and even grain boundary melting and the premelting phenomenon (Gleiter, 1989; Phillpot and Wolf, 1990; Alsayed *et al.*, 2005; Pusey, 2005). This is of relevance in understanding possible kinetic scenarios of both crystal-crystal phase transitions (in particular, in the context of externally constrained systems) and crystal-liquid transitions (especially in 2D). Other areas of interest are annealing, phonons, shock melting, and various nonlinear phenomena.

A. Relevance to conventional fluids

The obvious necessary conditions for fluid complex plasmas to be an appropriate medium to study the kinetics of conventional fluids are (i) transport coefficients are not affected by friction, which requires the time scale of individual particle dynamics $\sim \Omega_E^{-1}$ (see Sec. II.D) to be much shorter than the friction time scale ν^{-1} ; and (ii) all relevant length scales should be much larger than the discreteness scale Δ , so that the model of continuous media can be well applied. Another essential assumption is that the background gas remains at rest—this allows us to consider complex plasmas as a single-species fluid with a weak background friction proportional to the local velocity (Ivlev, Zhdanov, and Morfill, 2007): Collisions with microparticles do not affect diffusive motion of neutrals as long as the diffusion length at time scales $\sim \ell_{nd}/v_{T_n}$ exceeds the complex plasma size L , which yields $\ell_{nn}\ell_{nd} \gtrsim L^2$. The mean-free path of neutral particles due to collisions with micron-size particles, $\ell_{nd} = (\pi a^2 n_d)^{-1}$, is usually about a few meters, whereas the mean free path of neutral-neutral collisions (say, at pressures ~ 3 Pa) is $\ell_{nn} \sim 0.3-1$ cm. Thus, the assumption that neutral particles remain unaffected is well satisfied for typical system sizes $L \lesssim 10$ cm.

To demonstrate the relevance of complex plasmas to conventional fluids, we consider an example of free thermal convection. This phenomenon occurring in fluids outside equilibrium combines “typical fingerprints” of conventional hydrodynamics, such as shear flows and the associated dissipation, heat conduction, etc. As pointed out, the neutral gas friction in complex plasmas does not usually play a role in atomistic processes of the interparticle interaction, but certainly is important at much longer time scales related to the overall hydrodynamic flows. Therefore, the appropriate question here is: How (if at all) the friction changes the flow patterns and the onset of the convection in comparison to the friction-free (i.e., conventional fluid) case?

The onset of free thermal convection in fluid complex plasmas was analyzed by Ivlev, Zhdanov, and Morfill (2007) using the Oberbeck-Boussinesq equations modified due to background friction. The deviation of the particle velocity and kinetic temperature from the hydrostatic equilibrium (i.e., constant temperature and zero velocity, with pressure changing as $\rho \mathbf{g} \cdot \mathbf{r}$ and $\rho = \text{const}$) is given by (Cross and Hohenberg, 1993)

$$\partial_t \mathbf{v} + (\mathbf{v} \cdot \nabla) \mathbf{v} + \nu \nabla^2 \mathbf{v} = -\nabla(p/\rho) + (\eta/\rho) \nabla^2 \mathbf{v} - \beta \mathbf{g} T,$$

$$\partial_t T + \mathbf{v} \cdot \nabla T + 2\nu T = \chi \nabla^2 T \quad (25)$$

[here $\beta = \rho^{-1}(\partial\rho/\partial T)_p$ is the thermal expansion]. Equations (25) are complemented with the continuity equation $\nabla \cdot \mathbf{v} = 0$. For the Rayleigh problem, when a temperature difference Θ is maintained between two infinite parallel plates separated in the z direction by a distance L , the unperturbed temperature profile (without convection) is determined by $d^2 T_0/dz^2 = \alpha^2 T_0$. This yields $T_0(z) = \Theta \sinh(\alpha z/L)/\sinh \alpha$, where

$$\alpha = L/L_{\text{fr}} \quad (26)$$

is the ratio of the geometrical scale L to the length $L_{\text{fr}} = \sqrt{\chi/2\nu}$ of the temperature decay due to friction. In the frictionless limit we have $\alpha = 0$ and retrieve the linear profile, $T_0(z) \rightarrow (z/L)\Theta$. Using standard normalization one derives the governing equation that depends not only on the Rayleigh number $R = g\rho\beta\Theta L^3/\eta\chi$ but also on the Prandtl number $P = \eta/\rho\chi$ [not to be confused with the Havnes parameter P introduced in Eq. (9)]. The latter dependence occurs here because the decay of velocity happens at the scale length $\sqrt{P}L_{\text{fr}}$.

One can distinguish two limiting cases of weak ($\alpha \ll 1$) and strong ($\alpha \gg 1$) friction. These limits are referred to as the quasiclassical and friction-dominating Rayleigh-Bénard convection, respectively. The solution of Eq. (25) in the former limit yields the critical Rayleigh number with the corresponding critical wave number (normalized by L),

$$\begin{aligned} R^{\text{cr}} &\approx 1708 + \alpha^2(22.2P^{-1} + 136), \\ k^{\text{cr}} &\approx 3.12 + \alpha^2(0.002P^{-1} + 0.05). \end{aligned} \quad (27)$$

From Eq. (27) one can conclude that for $\alpha \lesssim 1$ the onset of convective instability remains practically unaffected by friction and hence the classical criterion can still be applied. This is a remarkable result because it shows that in fact the friction can be neglected even though the scale of the frictional dissipation is of similar magnitude as the hydrodynamic scale of the problem.

Even more striking is that in the friction-dominated case, irrespective of the value of α , the convection is not eliminated—it is just rescaled. Indeed, in this limit the problem does not depend on the geometrical scale L —the only remaining length scale is L_{fr} . Then the conventional Rayleigh number R and the wave number k are renormalized as $R_\infty \equiv \alpha^{-3}R$ and $k_\infty \equiv \alpha^{-1}k$. The critical values also depend on the Prandtl number and in the range $0.1 < P < 10$ can be given by

$$R_\infty^{\text{cr}} \approx 49P^{-0.35+0.068 \ln P}, \quad k_\infty^{\text{cr}} \approx 0.62P^{-0.13+0.011 \ln P}. \quad (28)$$

In comparison with the classical case with $R^{\text{cr}} \approx 1708$ and $k^{\text{cr}} \approx 3.12$, now R_∞^{cr} has a rather strong dependence on P and is smaller by a factor of 10–100. Figure 12 shows an example of the convection cell [for different P the shape of the cell remains practically the same and the actual size scaling is proportional to $k_\infty^{\text{cr}}(P)$]. Compared with

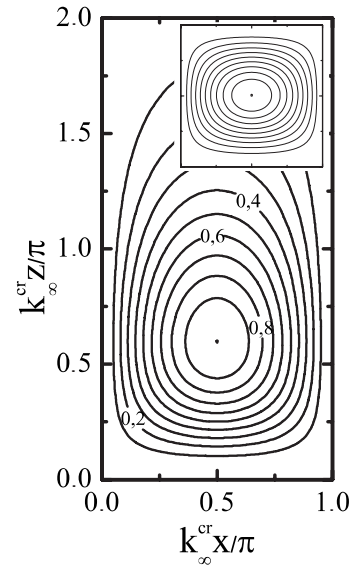


FIG. 12. Convection cell of the most unstable mode in the renormalized Rayleigh (friction-dominating) limit. Streamlines with the indicated vorticity magnitudes are drawn for the Prandtl number $P=0.2$. Coordinates are normalized by the corresponding critical wave number k_∞^{cr} , Eq. (28). For comparison, the inset shows the convection cell in the classic Rayleigh (frictionless) regime. From Ivlev, Zhdanov, and Morfill, 2007.

the almost square cell of the classical convection, the cell is asymmetric and somewhat stretched in the z direction since the temperature gradient is inhomogeneous and the upper boundary is at infinity.

The problem discussed highlights one remarkable property of complex plasmas: They provide us with a unique bridge that links colloidal systems (characterized by fully damped motion of microparticles) with virtually undamped systems, where weak friction does not affect atomistic dynamics but is revealed at much longer hydrodynamic time scales. By varying the gas pressure we can control the damping ratio ν/Ω_E and thus observe how the crossover from the colloidal to conventional single-species fluid regimes affects the hydrodynamic behavior. Later we address this property several times, when discussing different hydrodynamic phenomena occurring in complex plasmas and their relevance to conventional hydrodynamics.

B. Atomistic dynamics in fluids

Depending on the particle density and/or kinetic temperature, the dynamics of fluids at the atomistic level may exhibit very different behavior. At sufficiently high temperatures (low densities), fluids are known to be dynamically homogeneous in the sense that fluctuations at all relevant spatial and temporal scales (say, down to about the interparticle distance and the inverse Einstein frequency) are independent and statistically identical. Relaxation processes in such liquids obey the well-known Debye exponential law.

The situation changes dramatically when the temperature decreases [see, e.g., March and Tosi (2002)]. As the

freezing point approaches, particles become less mobile because their motion is stronger coupled to the neighbors and, therefore, fluctuations in neighboring regions become more correlated. The “caging effect” sets in, when at shorter time scales particles exhibit prolonged oscillatory motion in potential traps (cages) created by their neighbors. In the supercooled fluid regime, *dynamical heterogeneity* becomes the dominant feature: Particles move in increasingly cooperative manner creating dynamically correlated mesoscopic domains (Fischer, 1993; Sillescu, 1999; Reichman *et al.*, 2005; Saltzman and Schweizer, 2006). Decoupling of slow (the so-called alpha and beta) relaxation from rapid (molecular) relaxation occurs, with the former being related to the mesoscopic cooperative restructuring and the latter to the local in-cage motion (Götze and Sjogren, 1992; Stillinger, 1995; Götze, 1999). Different relaxation regimes have essentially different scaling laws. The beta regime (manifested by a plateau in the evolution of the relaxation function close to the glass transition) usually follows a power-law scaling whereas the ultimate alpha relaxation (which determines overall transport properties) typically exhibits a stretched-exponential decay ($\propto e^{-(t/\tau_\alpha)^\beta}$, the so-called Kohlrausch-Williams-Watts law with $0 < \beta < 1$). Eventually, below the glass transition point, the long-time alpha relaxation is frozen, accompanied by complete arrest of structural relaxations and only local in-cage motions remain.

Understanding the properties of supercooled fluids, especially in the vicinity of the glass transition, is one of the most controversial issues in contemporary physics of fluids (Jäckle, 1986; March and Tosi, 2002), with a number of mutually exclusive interpretations of various aspects of the complex supercooled fluids behavior currently being discussed.

For instance, there are at least two different scenarios of the dynamical heterogeneity resulting in the stretched-exponential relaxation at long times (Sillescu, 1999; Reichman *et al.*, 2005; Saltzman and Schweizer, 2006): One scenario relates this to the spatial heterogeneity, where relaxation occurs exponentially in each spatial domain and the relaxation time is different in each domain. Another scenario relates the heterogeneity to fluctuations in the stochastic activation processes (occurring in a spatially homogeneous medium), where cage escape that results in the long-term relaxation is induced by random thermal noise, so that the exponential decay is averaged over some distribution of the relaxation time scales.

Another major issue is the temperature dependence of the alpha-relaxation time scale τ_α (and related transport coefficients, e.g., viscosity). For numerous liquids it has been shown (Götze and Sjogren, 1992; Fischer, 1993) that the dependence is of the Arrhenius type ($\tau_\alpha \propto e^{E/T}$, where E may be viewed as an activation energy), but below a certain temperature (which is usually higher than the glass transition temperature T_g but lower than the melting temperature) a crossover to the super-Arrhenius type occurs ($\tau_\alpha \propto e^{\tilde{E}/(T-T_0)}$, the so-called Vogel-

Fulcher-Tammann law, where T_0 is somewhat lower than T_g). There are, however, many examples (Fischer, 1993; March and Tosi, 2002) when the temperature dependence in the crossover region is better approximated by a diverging power law $[\tau_\alpha \propto (T-T_c)^{-\gamma}]$ with typically $2 \leq \gamma \leq 2.5$, where the critical temperature T_c is somewhat higher than or almost coincides (e.g., in colloids) with the calorimetric value of T_g . Such dependence is in excellent agreement with the mode-coupling theory of the glass transition (Götze and Sjogren, 1992; Götze, 1999). There is a long ongoing discussion whether T_0 has any physical meaning, or “it appears as a mere artifact of the data fitting” and “ T_c marks the only physically significant crossover from liquid to glass behavior.”

Another important question is: What is the dependence of the structural glass transition on the spatial dimensionality? In particular, what is the role of geometrical frustration that is essential for the glass transition [see, e.g., Shintani and Tanaka (2006)]. Although geometrical frustration is impossible in 2D, the glass formation nevertheless has been observed in many numerical simulations of 2D polydisperse systems of hard disks as well as some systems with soft interaction potentials (Perera and Harrowell, 1999; Santen and Krauth, 2000; Bayer *et al.*, 2007).

Most of these features characterizing supercooled fluids (especially dynamical heterogeneity) are quite general. The particular form of the binary interaction potential plays only a minor role—the described properties have been reported for many model atomic systems, e.g., colloids, viscous silica, network-forming liquids (Reichman *et al.*, 2005). This gives us grounds to expect the behavior of supercooled fluids to be fairly universal.

Liquid complex plasmas can be considered as one of the best candidates to investigate the kinetics of 2D and 3D fluids in general and of supercooled fluids. Weak neutral damping plays a constructive role here, allowing us to control the cooling rate and therefore to bring the fluid to a desirable degree of overcooling [and vary the glass transition temperature, see, e.g., March and Tosi (2002)]. Along with the controversies mentioned above, kinetic investigations of supercooled fluids with complex plasmas may help us get a deeper insight into other major issues, e.g., which elementary mechanisms determine the stability of supercooled fluids against crystallization (Jäckle, 1986), what is the kinetics of the glass transition and how do the relevant processes such as arrest of the structural relaxation and loss of ergodicity evolve (Fischer, 1993; Sillescu, 1999), what microscopically determines the variation in the transport properties (especially self-diffusion) in the supercooled state (Saltzman and Schweizer, 2006), etc. Particularly interesting would be the investigation of the rapid relaxation regime where, e.g., the so-called “boson peaks” may appear as an excess contribution to the usual Debye density of states [see, e.g., Schirmacher *et al.* (1998) and Zorn (2003)]. Liquid complex plasmas (where the atomistic dynamics is practically undamped) are apparently the only available model system where the rapid relaxation can be studied at the kinetic level.

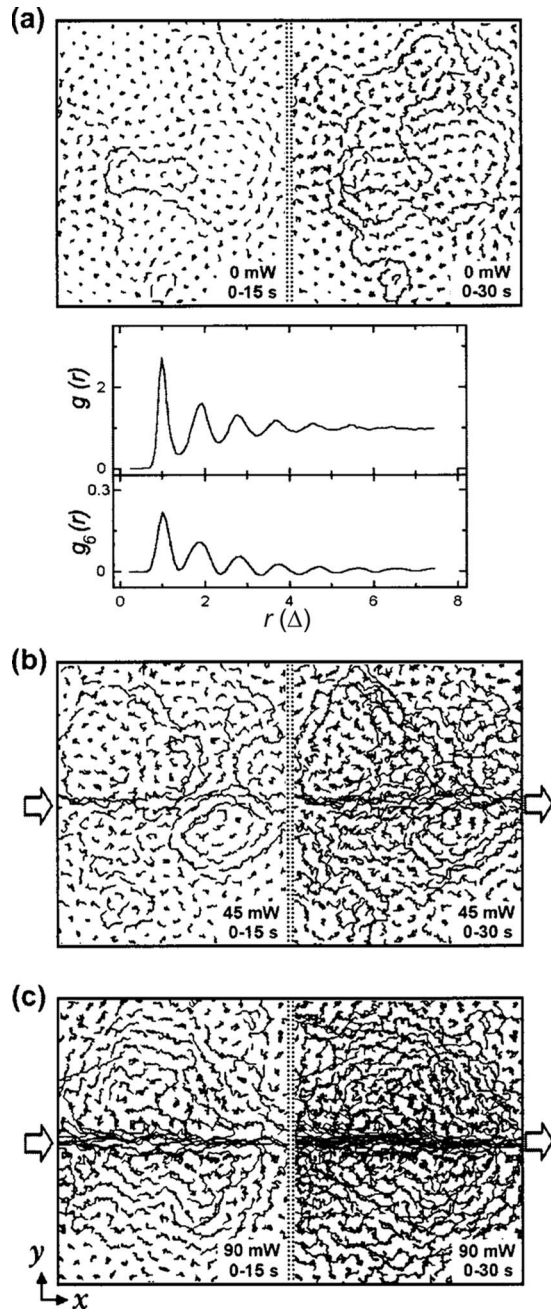


FIG. 13. Dynamical heterogeneity seen in quasi-2D liquid complex plasmas. (a) Trajectories of $7 \mu\text{m}$ diameter particles with 15 and 30 s exposure times for the laser-free liquid state. Shown below are the pair correlation functions of particle positions $g(r)$ and bond orientations $g_6(r)$. Particle trajectories in the laser-enhanced vortex motion under (b) 45 and (c) 90 mW laser power. The arrows indicate the position and direction of the laser beam. Adapted from [Juan *et al.*, 2001](#).

Atomistic behavior in liquid states has been observed in numerous experiments with 2D and quasi-2D strongly coupled complex plasmas ([Juan *et al.*, 2001](#); [Lai and I, 2002](#); [Woon and I, 2004](#); [Nunomura *et al.*, 2006](#); [Ratynskaia *et al.*, 2006](#); [Huang and I, 2007](#); [Liu and Goree, 2007, 2008](#)). As an example, we consider one particular experiment performed by [Juan *et al.* \(2001\)](#). Figure 13(a) shows a snapshot where most particles are mutually con-

finied by (quasiordered) neighbors, and exhibit caged motion with small amplitude oscillations. However, there is a certain fraction of particles that are in a rearrangement state. Spatially, one can observe coherent cage-escape events—strings or vortices surrounding crystallites (ordered domains) with the size of a few Δ . Usually, a local rearrangement ceases after the involved particles jump a distance of $\approx \Delta$ and then reenter the new caged state. Particles may start coherent rearrangement only after accumulation of sufficient “constructive” perturbations, and then transfer the excess energy to the neighbors through mutual interactions. The coherent motion is rapidly smeared out unless further constructive perturbation occurs at a time scale smaller than the momentum relaxation time.

Introducing external stress greatly enhances the formation of microvortices. Figures 13(b) and 13(c) show an experiment by [Juan *et al.* \(2001\)](#), where external stress in liquid complex plasmas was introduced by a laser. One can see that the intensity of microvortices gradually decays with distance from the shear source to the remoter regions. The observations can be reasonably explained by the following phenomenology: Even in a stress-free cool liquid, thermal agitation can distort the caging potential of neighboring particles through changing the particle’s relative positions, transfer energy to particles, and induce vortexlike escape over caging barriers. But introducing an external stress breaks the symmetry and further promotes forward jumping. In the low stress regime, when any rearrangement occurs at a low rate, the motion is still strongly constrained by caging. Increasing the stress level further usually promotes the rearrangement, although the advection can sometimes be jammed, forming local solidlike regions. Assisted by thermal fluctuations, the stressed particles will find the easiest “percolation” paths for rearrangement and branch off the stressed zone. The vacancy left behind can be filled up by the trailing particles or particles in the neighborhood of the laser beam, thus forming the vortices originated from the laser zone. Under the strong mutual particle interaction, these vortices quickly relax through cascaded excitations of new vortices with decaying strength in remote regions.

As mentioned above, observation at the individual particle level may shed light on what elementary processes determine the rich variety of unusual properties peculiar to supercooled fluids. In addition, knowledge of the fully resolved particle kinetics would allow us to calculate basic transport properties of the system from first statistical principles and compare the results with existing models ([Hansen and McDonald, 1986](#)). The common approach is to employ the Green-Kubo formalism that yields transport coefficients expressed in terms of time integrals over the relevant microscopic autocorrelation functions (such as velocity, shear stress, and energy flux for self-diffusion, shear viscosity, and heat conduction, respectively). This standard theory, however, is based on the assumption that the time integrals converge and therefore excludes an important class of processes called fractional Gaussian noises, which lead to particle trajec-

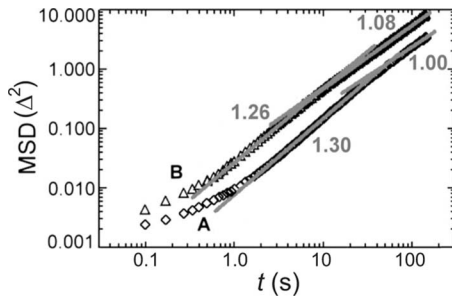


FIG. 14. Mean squared displacement of particles in quasi-2D strongly coupled complex plasmas. Curves A and B indicate experiments performed at different temperatures with particles of $7 \mu\text{m}$ diameter. One can see a transition from subdiffusive behavior (dominated by in-cage motion) to the long-time normal diffusion, mediated by a short superdiffusive stage (associated with cage-escape events). Adapted from [Lai and I, 2002](#).

tories described in terms of the fractional Fokker-Planck dynamics. For these processes the mean square displacement (MSD) scales as $\propto t^{2H}$, where H is the Hausdorff exponent: For $H=1/2$ we have standard diffusion, for $H<1/2$ the resulting motion is subdiffusive, and for $H>1/2$ the motion is superdiffusive. Standard diffusion theory also fails if the velocity probability distribution function is non-Gaussian but has algebraic tails, so that the velocity variance diverges.

Statistical analysis of individual particle trajectories in complex plasmas at sufficiently low temperatures (high densities) usually reveals subdiffusion at short and intermediate time scales (which are at the same time much longer than the “in-cage” oscillation time $\sim \Omega_E^{-1}$), with the crossover to normal diffusion at much longer times ([Lai and I, 2002](#); [Nunomura et al., 2006](#)), as shown in Fig. 14. (The crossover can be mediated by a relatively short superdiffusive stage.) On the other hand, several experiments ([Ratynskaia et al., 2006](#); [Liu and Goree, 2007, 2008](#)) demonstrated persisting superdiffusive long-time behavior. Figure 15 shows examples of such a system, where this anomaly was attributed to a combination of spatial (Levi flights) and temporal (long-range memory) nonlocalities ([Ratynskaia et al., 2006](#)). One should bear in mind that the long-time superdiffusion in complex plasmas has been observed either in relatively small and inhomogeneous systems [see, e.g., experiment by [Ratynskaia et al. \(2006\)](#), where superdiffusion might be triggered by boundary or confinement effects], or in systems with noticeable large-scale flow [which enhances transport and therefore increases asymptotical long-time value of H ; see, e.g., experiment by [Liu and Goree \(2008\)](#)]. One should also mention that in other systems (e.g., colloids) superdiffusive behavior apparently has never received reliable confirmation ([Reichman et al., 2005](#)).

It is generally accepted that above the glass transition fluids have properties of a viscoelastic medium ([Jäckle, 1986](#); [Fischer, 1993](#); [March and Tosi, 2002](#)). The simplest model that can be employed to describe diffusion in

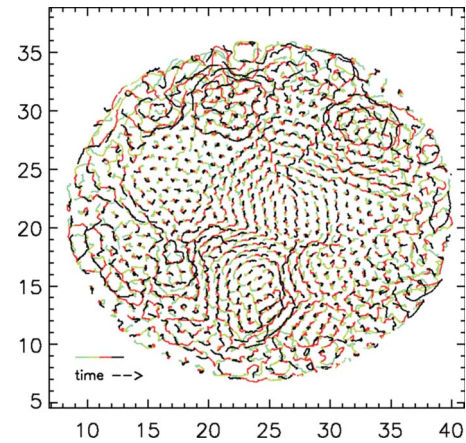


FIG. 15. (Color online) Example of nonequilibrium (anomalous) dynamical heterogeneity. Particles of $7.2 \mu\text{m}$ diameter formed an inhomogeneous disk-shaped monolayer. Color-coded trajectories over about 10 s are shown, distance is in units of mean interparticle spacing. From [Ratynskaia et al., 2006](#).

such media is based on a linear viscoelastic Langevin equation with a single relaxation time, $\dot{\mathbf{v}} + (\nu/\tau) \int_{-\infty}^t e^{-(t-t')/\tau} \mathbf{v}(t') dt' = \mathbf{f}(t)$, where \mathbf{f} is a random force (per particle) that satisfies the fluctuation-dissipation theorem and τ is the memory relaxation time ([Hansen and McDonald, 1986](#); [van Zanten and Rufener, 2000](#)). Assuming long-range memory, $\nu\tau \gg 1$, the qualitative behavior of the MSD derived from this simple approach has the distinct features observed in experiments: short ballistic motion, $\text{MSD} \approx 3\nu^2 t^2$, for $t \leq \sqrt{\tau/\nu}$ with crossover to a plateau, $\text{MSD} \approx \text{const}$, and eventual transition to normal diffusion, $\text{MSD} \approx 6\nu^2 \tau^{-1} t$, at $t \geq \tau$. Of course, quantitative agreement can only be received with more sophisticated models, e.g., by employing the nonlinear Langevin equation based on the formalism of the dynamic density functional theory ([Saltzman and Schweizer, 2006](#)). Such an approach, in particular, provides a treatment of activated barrier hopping—the process which can restore ergodicity close to the glass transition ([Sillescu, 1999](#)). Employing similar approaches to describe self-diffusion in fluid complex plasmas one can directly retrieve the alpha-relaxation time scale τ_α as a function of temperature and density.

A similar approach can also be employed to describe the flow of supercooled fluids under external stress. The essential feature of a viscoelastic flow is that it displays elastic deformation on short temporal and spatial scales but looks more like a viscous flow on larger scales. In the framework of the linear Maxwell model [see, e.g., [Landau and Lifschitz \(1986\)](#)], the strain γ is a superposition of two components: the elastic contribution responds to the stress through Hooke’s law, $\sigma = G\gamma$, and the viscous contribution through Newton’s relation, $\sigma = \eta\dot{\gamma}$, where G and η are the high-frequency Young’s modulus and static shear viscosity, respectively. From these limiting relations follows the differential equation $G^{-1}\dot{\sigma} + \eta^{-1}\sigma = \dot{\gamma}$. The general solution expresses the stress

as a linear response on the time history of the strain rate with an exponentially decaying response function with the Maxwell time scale $\tau_M = \eta/G$. This classical model implies a separation between the elastic and hydrodynamic responses controlled by the Deborah number $\dot{\gamma}\tau_M$: The response is viscous at time scales $t \gg \tau_M$ and elastic for $t \ll \tau_M$, at intermediate time scales we have a complex Young's modulus (or viscosity). By measuring the response to external stresses at different frequencies one can obtain the complex Young's modulus, derive τ_M , and compare it with the results retrieved from the diffusion measurements.

To conclude, one should note that the Maxwell rheological model is only applicable for fluids which are sufficiently far from the glass transition. The model usually breaks down at the crossover from the Arrhenius to super-Arrhenius scaling (Fischer, 1993), and then more sophisticated nonlinear models based on the mode-coupling theory should be implemented (Fuchs and Ballauff, 2005; Holmes *et al.*, 2005). Depending on a particular form of the memory function, one can obtain acceleration of the relaxation processes resulting in either shear thinning or, in contrast, significant shear thickening. In extreme cases, the flow curve σ vs $\dot{\gamma}$ may become S shaped, indicating discontinuous shear thickening and stress-induced transition from a fluid to a jammed glassy state (Holmes *et al.*, 2005).

C. Kinetics of stable flows

We now take a closer look at the individual particle trajectories in a fluid that exhibits a macroscopic flow. In complex plasmas, one can easily induce various types of flows with controllable characteristics by applying laser beams or creating flows in the neutral gas (Fortov *et al.*, 2005). A clear advantage of such methods of particle manipulations is that the background plasma, and hence parameters of the interparticle interaction, remain unchanged, yet the characteristics of the particle flow (especially the flow shear rate) can be varied over an exceptionally broad range.

In fact, shear flows appear as an almost inevitable ingredient of more complicated flows. Even in the simplest case of laminar shear flows, many fundamental questions immediately arise: What is the kinetic structure of the flow (e.g., how does the transverse momentum relaxation occur)? What is the kinetics of non-Newtonian fluids (e.g., what determines the relevant time scales in the viscoelastic fluids)? What happens at shear fluid boundaries (e.g., how good is the Navier ansatz for the slip velocity and what is the corresponding slip length)? In the case of multiphase flows, many more fundamental problems turn up, especially those related to the shear boundaries. Probably, the most obvious one is the contact-line singularity problem: a movable intersection of the fluid-fluid interface with the solid wall is incompatible with the no-slip boundary condition (Qian *et al.*, 2006).

The simplest experimental configuration that allows us to encompass most of the issues mentioned above is a

2D monolayer of particles, and the easiest way to create shear flows in this case is to use laser manipulation. Figure 16 shows an example of such an experiment by Nosenko and Goree (2004), when particles formed an (almost perfect) hexagonal crystalline monolayer, and the shear flow was created by applying two counter-propagating laser sheets. Increasing the laser power and, hence, the level of shear stress, they observed that the particle suspension passed through four distinct stages: elastic deformation, defect generation while in a solid state, onset of plastic flow, and fully developed shear flow. Figure 16 presents data for the latter two stages. At the onset of plastic flow, Fig. 16(a), the particles hopped between equilibrium lattice sites. Domain walls developed, and they moved continuously. The crystalline order of the lattice in the shearing region deteriorated, broadening the peaks in the static structure factor (not shown here). At still higher levels of shear stress, the lattice fully melted everywhere, and a shear flow developed, Fig. 16(b).

In terms of the applied laser power (and hence the resulting stress), the onset of the plastic flow is a rather distinct phenomenon with well-defined yield stress, suggesting that simplest rheological models [e.g., modifications of the Bingham plastic model, see Meyers and Chawla (1998)] are quite appropriate to describe the shear-induced melting. On the other hand, the individual trajectories of “percolating” particles that identify the onset of the plastic flow are quite peculiar: They have a zigzaglike shape, jumping along the local principal vector of the hexagonal lattice, i.e., in the direction where the macroscopic lattice has the least yield stress.

At the stage of fully developed shear flow, the particle motion is highly irregular on a small scale compared to the interparticle spacing, but on a larger scale, it is like a laminar flow in a fluid. In this case, the liquidlike order of the particle suspension can be clearly identified from the diffusiveness of the structure factor. Particles are confined so that after flowing out of the field of view on one side, they circulate around the suspension's perimeter and reenter on the opposite side. Within the field of view, more than 95% of the time-averaged flow velocity is directed in the x direction, with less than 5% of the flow velocity diverted in the y direction. It is worth noting that for all values of the laser power used in the experiment the local velocity distribution of particles is (with very good accuracy) a Maxwellian one, although at the highest shear rates the mismatch between the longitudinal and transverse temperatures is as high as $\sim 30\%$. This means that the internal momentum and energy equilibration in the particle ensemble is fast enough to balance the heat released due to the shear flow and, hence, the concept of equilibrium viscosity (as a function of self-consistent temperature corresponding to a given flow regime) is well justified.

Numerical simulations (Saigo and Hamaguchi, 2002; Salin and Caillol, 2002) predict that the shear viscosity of complex plasmas depends on the concentration of microparticles, which is an essential feature of complex fluids. Moreover, recent experiments and simulations

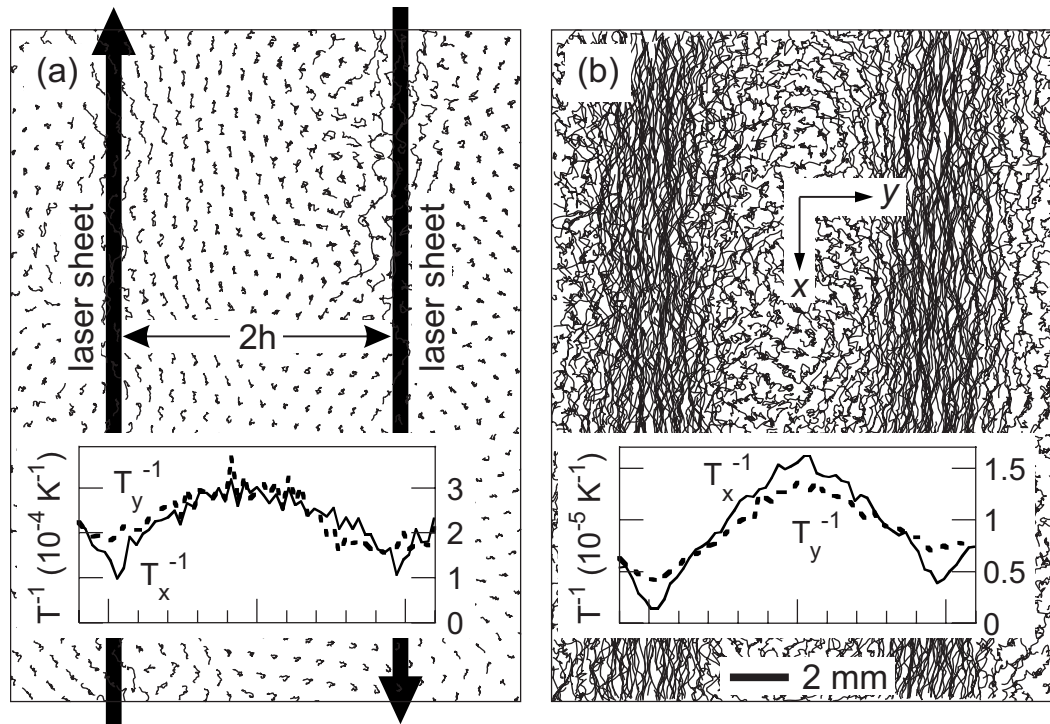


FIG. 16. Planar Couette flow in a 2D complex plasma. Initially crystalline microparticles of $8.09 \mu\text{m}$ diameter are sheared by two counterpropagating laser sheets. (a) At the onset of plastic flow, the particles hop between equilibrium lattice sites. (b) In a fully developed shear flow, the particle motion is highly irregular on smaller scales comparable with the interparticle spacing, but on larger scales it is like a laminar flow in a fluid. Trajectories over ≈ 1.7 s are shown. Adapted from [Nosenko and Goree, 2004](#).

([Nosenko and Goree, 2004](#); [Gavrikov et al., 2005](#); [Donko et al., 2006](#); [Ivlev, Steinberg, et al., 2007](#)) verified that the viscosity can exhibit significant shear thinning and/or thickening. This non-Newtonian behavior of complex plasmas occurs because the viscosity η is a function of the kinetic particle temperature which, in turn, is determined by the local viscous heat released due to shear flow and is proportional to $\eta\dot{\gamma}^2$. Based on this simple rheological model ([Ivlev, Steinberg, et al., 2007](#)), one can identify three distinct regimes for a qualitative dependence of the viscosity and the shear stress $\sigma = \eta\dot{\gamma}$ on the shear rate $\dot{\gamma}$: (i) At sufficiently low $\dot{\gamma}$ the viscosity remains constant and stress grows linearly with $\dot{\gamma}$, which corresponds to Newtonian fluids. (ii) Above a certain critical value of $\dot{\gamma}$ shear thinning is observed, which can be quite significant—the viscosity can decrease by an order of magnitude. (iii) At even higher $\dot{\gamma}$ the crossover to the shear thickening occurs. A remarkable rheological feature is that the viscosity decrease in the second regime can be so rapid that the $\sigma(\dot{\gamma})$ dependence may have an anomalous N-shaped profile. In this case the part of the curve with $d\sigma/d\dot{\gamma} < 0$ becomes unstable and the flow is accompanied by a discontinuity in $\dot{\gamma}$. This causes the formation of shear bands—a phenomenon often observed in complex fluids ([Salmon et al., 2003](#)). Thus, liquid complex plasmas can exhibit essential rheological features peculiar to classic non-Newtonian fluids.

Moreover, by combining different methods to induce shear flows (e.g., inhomogeneous gas flows and laser beams) one can directly measure the shear viscosity in

the entire range of shear rates—all the way to the limit where the discreteness enters and a fluid cannot be formally considered as a continuous medium. Probably, the most surprising result of such an investigation was that at extreme shear rates (up to $\dot{\gamma} \sim U/\Delta$, where U is the magnitude of the flow velocity and Δ is the interparticle distance), the formal hydrodynamic description with the Navier-Stokes equation still provides fairly good agreement with the experiment ([Ivlev, Steinberg, et al., 2007](#)).

It is worth mentioning that the transport coefficients of fluid complex plasmas, including the viscosity, could be calculated numerically for an arbitrary rate of the frictional dissipation ([Vaulina et al., 2002](#); [Vaulina and Dranzhevskii, 2007](#)). However, in contrast to steady-state structural properties (see Sec. II.E), the kinetics of individual particles in strongly dissipative systems (say, when $\nu/\Omega_E \geq 1$) would inevitably be different from that in conventional single-species fluids. Therefore, such systems would probably not be relevant for investigating the kinetics of the momentum transfer in shear flows. Next, where we focus on the kinetics of the energy transport, the importance of weak frictional dissipation becomes particularly clear.

D. Kinetics of heat transport

Thermal conductivity is an important property of matter that is essential in many engineering applications. At the same time, the behavior of thermal conductivity in various situations is governed by diverse fundamental

processes that occur at the atomistic (kinetic) level. Measurements of the thermal conductivity in regular matter are only possible at a macroscopic scale and therefore cannot resolve the details of the heat transfer processes at their atomistic level. The obvious reason for this is the lack of experimental techniques to study the motion of individual atoms. Therefore, liquid or solid complex plasmas also occupy an invaluable position of an experimental model system where the motion of individual atoms can be observed in real time.

Analysis of the heat transport, especially in 2D crystalline systems, is a controversial problem that has a long history: Some claim that the thermal conductivity of such systems diverges in the thermodynamic limit. Liquid systems are far less studied—one can mention a simulation of frictionless hard disks by Shimada *et al.*, (2000), where the thermal conductivity slowly diverged as well, and a theoretical study by Ernst *et al.* (1970), where the lack of a valid thermal conductivity was conjectured. Systems undergoing a phase transition, were not studied at all.

Recently, kinetics of the heat transport in liquid and solid complex plasmas was experimentally investigated (Fortov, Vulina, *et al.*, 2007; Nosenko *et al.*, 2008). Below we discuss on the experiment by Nosenko *et al.* (2008) in a 2D complex plasma that is undergoing a phase transition and therefore constitutes a mixture of crystalline and liquid phases. To melt the lattice locally and to control the temperature of the resulting liquid complex plasma, the laser-heating method has been employed so that particles were pushed randomly by the radiation pressure force. To produce a quasi-1D temperature gradient, with temperature varying mostly in the y direction, a narrow area which extended fully across the particle suspension in the x direction was heated, as shown in Fig. 17(a). Under these conditions, heat was mainly transferred by thermal conductivity in the region where the temperature gradient was high.

Figure 17(b) shows the resulting profiles of the kinetic particle temperature $T(y)$ measured for different values of the laser power. The particle suspension was melted in this temperature range, as can be seen from the analysis of the pair correlation function $g(r)$: Far from the laser-heated area, $g(r)$ has the characteristic appearance of the solid phase with notably many peaks, whereas inside the laser-heated area, $g(r)$ is typical for a liquid phase with a few peaks. (Note that the background temperature of the crystal T_b was naturally increasing with the applied laser power P_{laser} .) Also, according to the KTHNY theory (see Sec. III.1.2), a 2D solid melts via two second-order phase transitions: Estimates show that the two temperatures corresponding to the transitions lay well within the temperature range achieved in the experiment. Irrespective of the applied heating power P_{laser} , the measured temperature profiles are well fitted by the exponential function $T(y) \propto \exp(y/L_{\text{heat}})$, where the heat transport length L_{heat} turned out to be practically constant. In the framework of the continuous approach to the heat transport, such scaling implies that

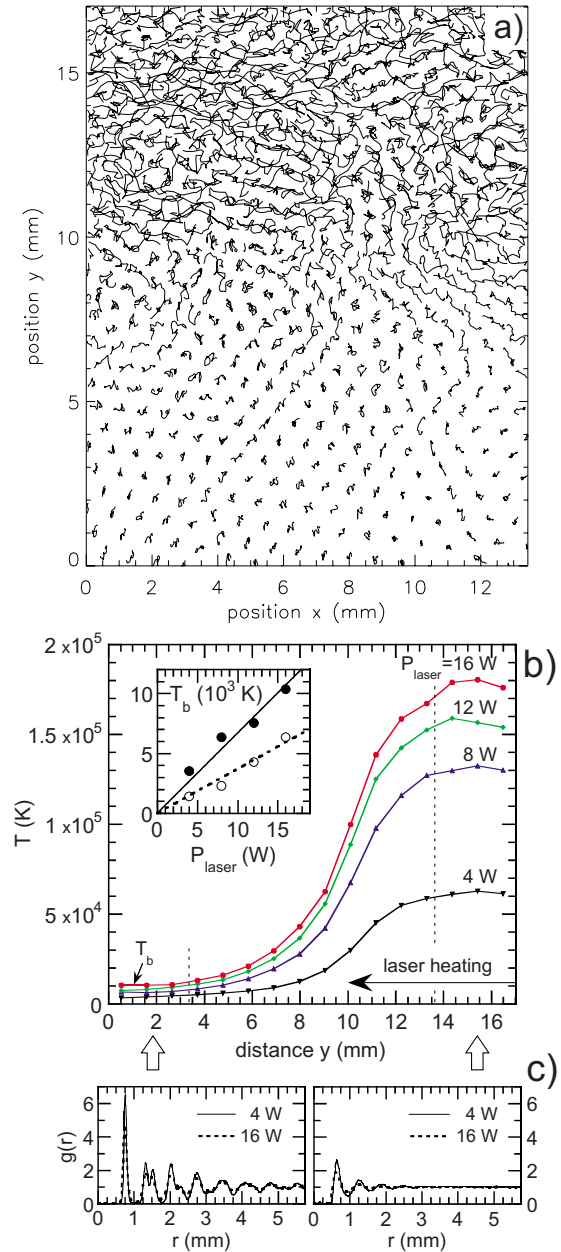


FIG. 17. (Color online) Heat transport in 2D complex plasmas. (a) Example of the particle trajectories (8.09 μm diameter, duration ≈ 1.7 s) in a 2D plasma crystal heated by a laser at power of $P_{\text{laser}}=16$ W (heated region $y > 13.6$ mm). (b) Profiles of the kinetic particle temperature as a function of the transverse coordinate y , for different values of P_{laser} . The inset shows the background particle temperature T_b . (c) Pair correlation function $g(r)$ far from the heated region (left) and inside the heated region (right), suggesting crystalline and liquid states, respectively. Adapted from Nosenko *et al.*, 2008.

L_{heat} is identical to the friction length $L_{\text{fr}} \equiv \sqrt{\chi/2\nu}$ [see Eq. (26)], and hence the thermal diffusivity χ is independent of T .

Thus, the heat transport in a 2D system that undergoes a phase transition turns out to be quite interesting: On the one hand, the experiment yielded the expected result that the thermal conductivity χ does not exhibit any major discontinuity at the liquid-solid phase

boundary—such behavior is well known in regular matter (March and Tosi, 2002). On the other hand, the values of χ obtained for different particle temperatures are almost the same. This result is not trivial, since individual phases, solid and liquid, are expected to have a temperature-dependent thermal conductivity. Nosenko *et al.* (2008) suggested that the dominant mechanism of thermal conduction in such systems is phonon scattering on heterogeneous fluctuations that occur in the melting region.

It is important to emphasize that although the measured temperature profile (*viz.*, the value of L_{heat}) is determined by friction, the thermal conductivity itself is solely determined by internal generic properties of the medium (the Yukawa system in our case) and does not depend on the damping: It was shown that the effective phonon scattering length ℓ_{ph} that actually determines the heat conduction ($\chi \approx \frac{1}{2} C_l \ell_{\text{ph}}$) is at least an order of magnitude smaller than the frictional phonon decay length ($\approx C_l / \nu$), where C_l is the measured longitudinal acoustic velocity (see Sec. II.D). This allows us to extrapolate knowledge about the kinetics of heat transport (gained with weakly damped complex plasmas) to regular condensed matter and, thus, to understand more about generic atomistic processes governing the thermal conductivity.

E. Hydrodynamics at the discreteness limit

The discreteness issue of continuous media can be formulated as follows: What is the smallest scale at which the conventional hydrodynamic description breaks down? Apparently, the answer depends on the particular problem under consideration: It is determined by the similarity variables (and hence the related physical parameters) that play the major role in the description of the macroscopic problem. For instance, for a planar shear flow this is, primarily, the Reynolds and Mach numbers, whereas for a flow past an obstacle or a droplet breakup this can be the Weber number. (Of course, one should remember that the basic parameters entering hydrodynamics such as viscosity or surface tension are quantities which are well defined only for sufficiently large systems.)

1. Basic hydrodynamic instabilities

To get the quantitative characteristics of hydrodynamic instabilities at the discreteness limit, we discuss the progress achieved recently in simulating large systems of discrete particles forming an interface. In particular, the microscopic origin of the Rayleigh-Taylor (RT) instability was explored in MD simulations.

Kadau *et al.* (2004) simulated the initial stage of the RT instability with a few million particles interacting via the Lennard-Jones potential and obeying undamped (Newtonian) dynamics. The appearance of the mixing layer as well as major scalings obtained from the simulations were shown to be in good agreement with classic hydrodynamic results.

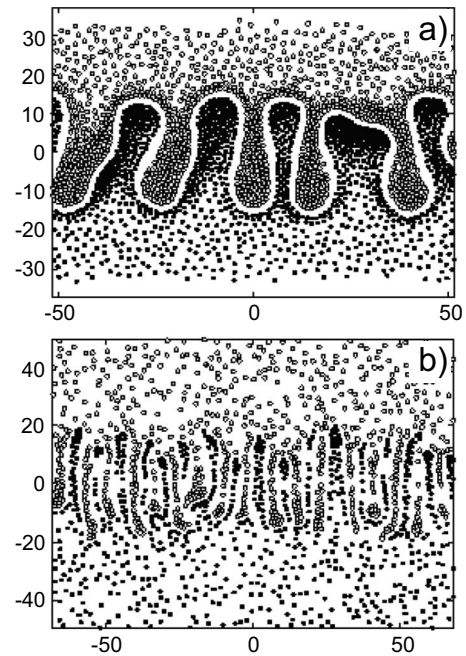


FIG. 18. MD simulation snapshots for an interface with externally driven colloids. Distances are measured in units of the particle hard-core radius, the starting configuration was an equilibrated horizontal interface at zero height. Particles in the upper fluid phase are driven downwards, whereas in the lower phase they are driven upwards (all forces are of the same magnitude). Examples of (a) high and (b) low surface tension are shown, with the lane formation onset seen in the latter case. Adapted from Wysocki and Löwen, 2004.

Wysocki and Löwen (2004) performed the complementary MD simulations of the RT instability in the fully damped (Brownian) regime peculiar to colloidal suspensions. In these simulations, two different scenarios were observed that occur for either high or low surface tension, as shown in Fig. 18.

The high-surface-tension scenario [Fig. 18(a)] is characterized by interfacial instability which is similar to the classical Rayleigh-Taylor instability (Chandrasekhar, 1961). As in the undamped case, the classical threshold value for the wavelength of unstable interface perturbations is confirmed. Development of the mixing layer at the initial stage has similar appearance to that seen in undamped Newtonian liquids (Kadau *et al.*, 2004), although at the later stage the interpenetrating bubbles and spikes do not develop into “mushrooms” but keep growing further aperiodically. The thickness of the mixing layer also increases as $\propto t$ with time instead of the classic $\propto t^2$ scaling. Phenomenologically, such a difference is because the governing equation for the Brownian dynamics does not contain the time derivative of the velocity. Therefore, in analogy with the classic case when spatial perturbations driven by a uniform external field exhibit “free” kinematic growth $\propto t^2$, the RT development in overdamped systems should reveal the linear temporal scaling.

When the interfacial surface tension is low enough [Fig. 18(b)], a completely different development is ob-

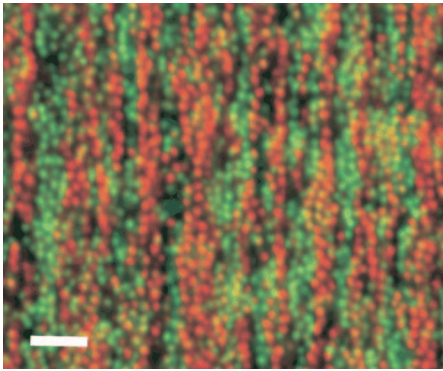


FIG. 19. (Color) Lane formation in experiments with driven colloidal suspensions. Steady-state self-organized flow of positively (green) and negatively (red) charged microparticles of $\approx 1 \mu\text{m}$ diameter is created by an external electric field in the vertical direction. Scale bar is $10 \mu\text{m}$. From [Leunissen *et al.*, 2005](#).

served: The particles penetrate the interface easily as a result of the driving field and form microscopic lanes. The structure of these lanes is very similar to that seen in numerical simulations ([Chakrabarti *et al.*, 2004](#)) and experiments ([Leunissen *et al.*, 2005](#)) with driven colloidal suspensions, as shown in Fig. 19. These results are obtained in the regime when the classical RT threshold for the unstable wavelength (calculated for given values of the surface tension and driving force) is smaller than the interparticle distance and hence a breakdown of hydrodynamics is expected. Therefore, the microscopic appearance of the RT instability might be completely different as the discreteness enters, and this conclusion is rather intuitive: The surface tension is the only stabilizing mechanism of the instability, and once this mechanism becomes negligible and hence allows growth at hydrodynamic scales smaller than the discreteness limit, the hydrodynamics itself becomes meaningless. On the other hand, the instability should develop in some form anyway, and the only imaginable picture for that are the interpenetrating strings, as observed in the simulations as well as in experiments.

In addition to colloidal suspensions ([Leunissen *et al.*, 2005](#)) and pedestrian zones ([Helbing *et al.*, 2000](#)) lane formation can be easily triggered in complex plasmas ([Morfill *et al.*, 2006](#); [Sütterlin, 2009](#)). As we already discussed, complex plasmas provide an important intermediate dynamical regime that is between classic undamped fluids and fully damped colloidal suspensions: In complex plasmas, the internal dynamics associated with the interparticle interaction is undamped whereas the large-scale hydrodynamics can be strongly affected by friction. Nevertheless, the mesoscopic appearance of lane formation in colloids and in complex plasmas is similar, which gives us grounds to believe that this phenomenon constitutes an ultimate generic form of the RT instability in any driven (strongly coupled) fluid.

Figure 20 shows an example of lane formation observed in complex plasmas with particles of different sizes ([Sütterlin, 2009](#)). The net force acting on particles

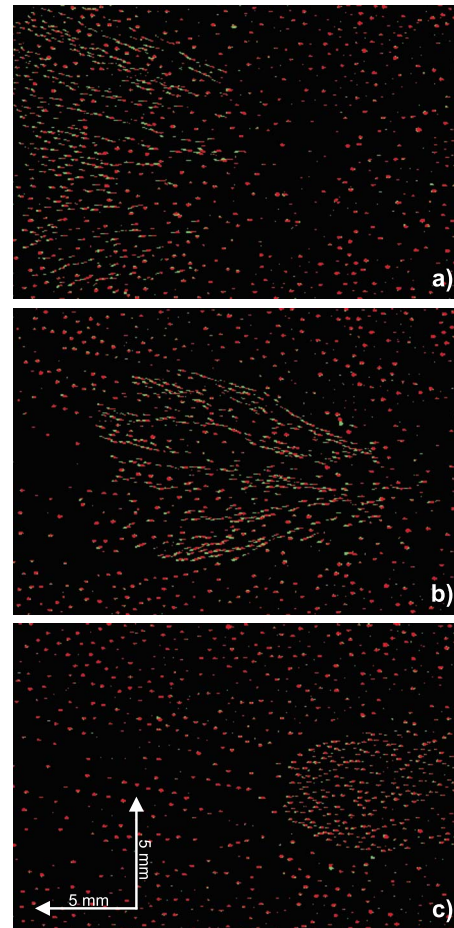


FIG. 20. (Color online) Lane formation in complex plasmas. A short burst of small ($3.4 \mu\text{m}$) particles injected into a cloud of large ($9.2 \mu\text{m}$) background particles are driven from left to right. Stages shown for (a) initial lane formation, (b) merging of lanes into larger streams, and (c) eventual droplet formation. Each panel is a superposition of two consecutive color-coded images ($1/50 \text{ s}$ apart) entire sequence is about 2.5 s long. From [M. Rubin-Zuzic](#).

in a discharge plasma (a combination of the electric and ion drag forces, see Sec. II.C) depends on the diameter and plays the role of an effective gravity pointed to the right (the force is relatively strong at the left edge and almost vanishing at the right edge of the figure). Initially, the large particles formed a background fluid in hydrostatic equilibrium. When a small fraction of individual small particles entered the system from the left, their sedimentation towards the right edge of the figure was accompanied by a remarkable self-organization sequence: First, the particles form strings flowing along the force field (a); then, as the field decreases, strings organize themselves into larger mesoscopic streams (b); and at the later stage, when the field almost vanishes, streams merge to form a spheroidal droplet with well-defined surface (c), indicating the transition to the regime when the effective surface tension should play the primary role ([Ivlev *et al.*, 2009](#)).

In order to investigate the RT instability in further detail, we consider examples of highly resolved shear

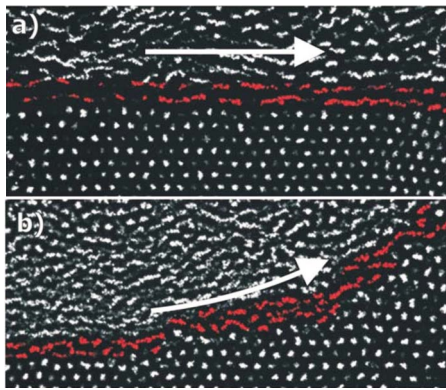


FIG. 21. (Color online) Two examples of highly resolved complex plasma flows. (a) Shear flow over a flat-surface plasma crystal and (b) flow over a curved-surface plasma crystal. Note the small angle perturbations in the particle trajectories in (a), and the considerably larger scattering in the curved flow in (b). Particles are of $6.8 \mu\text{m}$ diameter, the flow velocity is $\sim 1 \text{ mm/s}$. From Morfill, Khrapak, *et al.*, 2004.

flows observed in complex plasmas (Morfill, Khrapak, *et al.*, 2004) and shown in Fig. 21. Different flow topologies were observed, with the (average) flow lines either straight (a) or curved with a radius of curvature of about $80\text{--}100\Delta$ (b). The lower part of the microparticle cloud is at rest. Observations suggest that the width and the structure of the transition (mixing) layer strongly depends on the geometry. For the planar flow the interface is quite smooth, with the flow along a particular monolayer. The trajectories of individual flowing particles experience only weak deflections and the overall flow appears to be stable and laminar. In contrast, the curved flow interface has a curious rough structure, the flow is not laminar, a mixing layer is formed. It is also apparent that the mixing layer becomes unstable at the individual particle level. The microscopic behavior may be interpreted as the centrifugally driven Rayleigh-Taylor instability. Analyzing a whole sequence of such images, one can quantify elementary (discrete) perturbations in two ways: the fraction of interpenetrating (say, $\geq \Delta$) particles and the fraction of particles undergoing large-angle (say, $\geq 30^\circ$) collisions in the surface layer. For instance, for straight flow the quantities are (almost) 0% and $\sim 3\%$, for the curved flow $\sim 3\%$ and $\sim 30\%$. The latter can be understood kinetically in terms of the higher collision frequency with smaller impact parameter due to particle inertia at a curved surface. This has also been confirmed by numerical simulations conducted for similar geometry and flow conditions as in experiments. The topology of the mixing layer found in the simulations corresponds closely to the measurements, which supports the kinetic interpretation.

Following these considerations, one can argue that the Kelvin-Helmholtz (KH) instability at the discreteness limit also has a different appearance. In order to illustrate this point, we consider another example of the hydrodynamic behavior of liquid complex plasmas (Morfill, Rubin-Zuzic, *et al.*, 2004) shown in Fig. 22. Particles

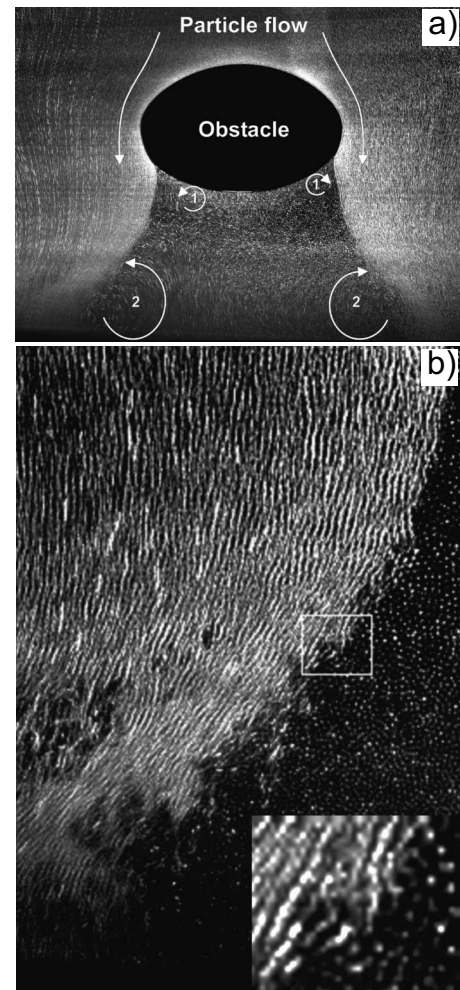


FIG. 22. Flow past an obstacle in fluid complex plasmas. (a) Overall topology of the $3.7 \mu\text{m}$ particle flow, the system is approximately symmetric around the vertical axis (exposure time 1 s). The flow leads to a compressed laminar layer, which becomes detached at the outer perimeter of the wake. The steady vortex flow patterns in the wake are illustrated. The boundary between the laminar flow and wake becomes unstable; a mixing layer is formed, which grows in width with distance downstream. (b) An example of the mixing layer (an enlargement of the left side, exposure time 0.05 s). The points (lines) represent traces of slow (fast) moving microparticles. The inset shows trajectories of individual particles in the mixing layer. From Morfill, Rubin-Zuzic, *et al.*, 2004.

were flowing around an “obstacle”—the void of size $\sim 100\Delta$. One can see stable laminar shear flow around the obstacle, the development of a downstream “wake” exhibiting stable vortex flows, and a mixing layer between the flow and the wake. The enlargement of the mixing layer [Fig. 22(b)] shows that the flow is quite unstable at the kinetic level, with instabilities becoming rapidly nonlinear. The width of the mixing layer grows monotonically with distance from the border where the laminar flow becomes detached from the obstacle. The growth length scale is of the order of a few Δ , i.e., much smaller than the hydrodynamic scales $n(dn/dx)^{-1}$ or $u(du/dx)^{-1}$, which would be expected macroscopically in

fluids and which refer to the RT or KH instability, respectively. This rapid onset of surface instabilities followed by mixing and momentum exchange at scales $\sim \Delta$, i.e., the smallest interaction length scale available, is not consistent with conventional macroscopic fluid instability theories. While this could not be expected at the kinetic level, it points to new physics and, possibly, a hierarchy of processes that is necessary to describe interacting fluid flows: first, binary collision processes provide particle and momentum exchange on discreteness scales (a few Δ), then collective effects (due to the correlations defining fluid flows) take over and propel this discrete instability to macroscopic scales, creating cascades of growing clumps characterized by increased vorticity.

Although the onset of the instability shown in Fig. 22 occurs at scales $\sim \Delta$, its further development is in good agreement with the simplest conceptual picture of the continuous jet turbulence: It is well known that the mixing between a jet and its surroundings occurs in two stages [see, e.g., Tennekes and Lumley (1972)]. During the first stage (which is a distinct peculiarity of jets), a shear layer is formed immediately downstream of the jet source, between jet stream and surroundings. As one moves downstream, there is an early linear-instability regime, involving exponential growth of small perturbations introduced at the jet source. Beyond this development stage, in the nonlinear KH instability regime, the dynamics of large-scale vortex formation and merging become the defining feature of the transitional shear flow. Apparently, the observed clump cascading fully mimics this scenario, which suggests again that the similarity of the coarse-grained hydrodynamics is preserved down to the physical discreteness limit.

Unfortunately, so far in experiments with complex plasmas it was impossible to observe the second stage typical to any developed turbulence—when vortices (clumps) break down, leading to a more disorganized flow regime characterized by smaller-scale vortices. The spectral energy content at this stage should be consistent with the Kolmogorov's inverse cascade theory of turbulence. These processes develop at much longer time scales, when the neutral friction plays an important role and simply “freezes out” free hydrodynamic motion. In order to observe this turbulent stage in experiments, one needs to decrease the neutral gas pressure substantially and to increase the size of the complex plasmas.

These examples suggest a naive microscopic picture of the hydrodynamic instabilities: It is not unreasonable to conclude that many instabilities have a kinetic analog or trigger and that the most effective trigger mechanism is provided by binary large angle scattering in localized structures and/or inhomogeneities of scales comparable to the particle correlation length. However, the mathematical techniques required to quantify the kinetic behavior and to transfer this to macroscopic scales still need to be developed.

2. Viscosity-modulation instability

Flows of complex fluids in long tubes at rather low Reynolds numbers show various instabilities that are absent in the case of Newtonian one-phase fluids (Goldsmith and Mason, 1967; Cox and Mason, 1971; Koch and Hill, 2001). Numerous ideas and theories were suggested to explain part of these phenomena [see, e.g., de Gennes (1979); Nozieres and Quemada (1986); Papoular (1987)] but most of them still remain unexplained. In this context, it is noteworthy to mention a novel type of hydrodynamic instability that can develop in fluids with *density-dependent* viscosity (Steinberg *et al.*, 2008). Complex plasmas are not the only example of such fluids—in fact, there exists a broad class of complex fluids (suspensions, emulsions, colloids, or other dispersed fluids) that have a rather strong dependence of the viscosity on density, governed by Einstein's law (Batchelor, 1953; Landau and Lifschitz, 1987). This suggests that the instability mechanism might be quite general.

According to Steinberg *et al.* (2008), essential ingredients that may result in this instability are density-dependent viscosity, two (or three) dimensionality of the flow, and compressibility: Due to mass conservation, small perturbations that cause increase (decrease) in a flow velocity result in a density decrease (increase). These variations in the density lead to the viscosity modulation and via the momentum equation provide a feedback for the velocity. At some conditions the feedback becomes positive and triggers the instability. The only factor stabilizing the instability is the fluid elasticity.

A rigorous linear stability analysis can be performed by solving the corresponding boundary-value problem. We consider a plane Couette flow between two parallel plates separated by a distance L moving in opposite directions with the velocity U . For fluids of constant viscosity, this situation is known to be absolutely stable against linear subsonic perturbations. However, when the variation in the dynamic viscosity η with density ρ is characterized by the exponent $\epsilon = d \ln \eta / d \ln \rho$, the analysis shows (Steinberg *et al.*, 2008) that an instability is possible for $\epsilon > 4/3$, and then it is triggered if the flow shear rate $\dot{\gamma} = U/L$ exceeds a certain threshold. For sufficiently large values of $\epsilon - 4/3$, the threshold is given by $\epsilon \dot{\gamma}_{\text{th}} \approx \rho C^2 / \eta$, where C is the sound velocity in the fluid. The most dangerous density perturbations are those at $\approx \pi/4$ with respect to the flow direction. Such an instability develops for sufficiently large wave numbers, $k \gg \rho C / \eta$, i.e., also when the spatial scale of density perturbations approaches the discreteness limit Δ , unless there are new physical effects that may come into play.

Such an instability may develop in very viscous fluids [e.g., low molecular weight polystyrene or α -D-glucose (Archer *et al.*, 1997)] with viscosity $\sim 3 \times 10^5$ P and $\epsilon \sim 100$. For the sound velocity $C \sim 10^5$ cm/s, one then gets $\dot{\gamma}_{\text{th}} \sim 10^3$ s $^{-1}$ a value that is achievable at $L \sim 1$ cm. In this case we find the Reynolds number $\text{Re} = \rho \dot{\gamma}_{\text{th}} L^2 / \eta \sim 10^{-2}$ and the Mach number $M = \dot{\gamma}_{\text{th}} L / C \sim 10^{-2}$. In complex plasmas, where the scaling exponent

ϵ is usually well above the critical value of $4/3$, the instability should be observed, e.g., for the shear flow shown in Fig. 22 (with $\dot{\gamma} \sim 10^2 \text{ s}^{-1}$), where the instability condition is well satisfied.

F. Confined fluids

As fluid systems are engineered to smaller scales, down to the atomic size, the special effects associated with the confinement of fluids become increasingly important. The behavior of such systems is a fundamental problem in technology (areas such as lubrication, adhesion, nanofluidics, microchannel spectrometry, surface functionalization, etc.). The general consensus is that the smaller the system, the more important the confinement even for intrinsic properties (Hummer *et al.* 2001; de Mello, 2006; Heller *et al.*, 2006; Whitby and Quirke, 2007). It is inevitable that there will be new physics associated with finite size effects, due to surface interactions and reduced dimensionality. From the application point of view, understanding the functionalization of nanoflow surfaces to achieve the desired form of hydrophobic or hygroscopic behavior (for a given fluid) in the absence or presence of external fields (which would give rise to nano-electrorheology or electro-osmotic flows) is clearly one of the aims—and no doubt there are many others (Miller *et al.*, 2001; Vaitheeswaran *et al.*, 2004).

There have now been many studies of confined flow systems, e.g., nanoporous materials (ordered or disordered), thin fluid films, microchannels, etc. Amongst the areas of interest are topics such as demixing (segregation) of biological fluid components, flows in nanocapillaries, the effects of confinement on the fluid structure and on freezing and melting [for a recent review, see Alba-Simionesco *et al.* (2006) and Whitby and Quirke (2007), and references therein]. The optimum way to study the basic (generic) physics is to employ a system where kinetic measurements are possible at all relevant length and time scales. Currently the only systems capable of satisfying all these requirements are complex plasmas. In Sec. III.G complex plasmas are shown to have electrorheological properties under certain conditions and that it is possible to “design” the binary interaction potential between the particles using external fields (Ivlev *et al.*, 2008; Kompaneets *et al.*, 2009). This will provide great opportunities for future basic and applied research in a number of fields in condensed matter physics and beyond, and in particular for confined (nano)systems.

In this section we concentrate specifically on the first studies involving liquid complex plasmas, their “kinetic structure” in confined channel flows, and the dependence on the confinement potential. All confined flow experiments with complex plasmas have so far been conducted on the ground, i.e., the microparticles are suspended against gravity in the sheath region above the lower electrode. Horizontal confinement is affected by nonconducting glass walls (which then attain floating potential), by conducting segmented electrodes (that can be actively powered and can be used to transport the

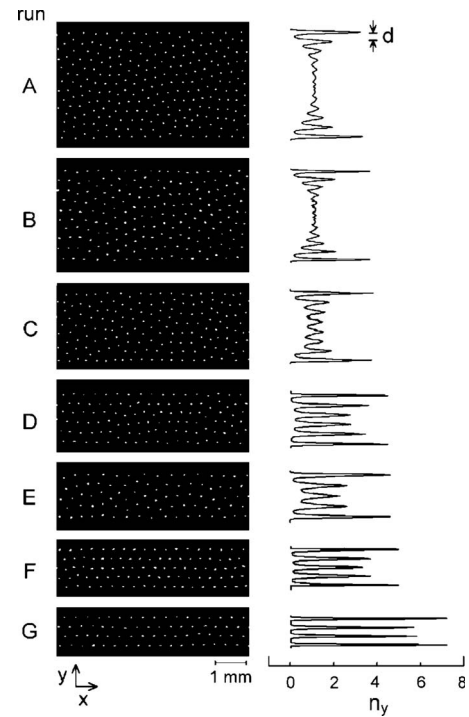


FIG. 23. Liquid complex plasmas in narrow channels. The typical snapshots of the $7 \mu\text{m}$ particle configurations and the transverse particle density distributions n_y for different experiments with decreasing number of layers N (width measured in units of the interparticle spacing), from 11 to 3. From Teng *et al.*, 2003.

particles), or by conducting metal channels placed on the lower electrode.

Teng *et al.* (2003) reported on the microscopic observation of the confinement-induced layering in quasi-2D complex plasma liquids. Two parallel vertical plates were put on a horizontal rf electrode surface to laterally confine particles and, hence, to form mesoscopic channels down to a few interparticle spacings in width. Microscopically, the particle mutual interaction tends to generate ordered triangular lattice-type domains with small amplitude position oscillations, which can be reorganized through string- or vortex-type hopping activated by thermal noise. However, the boundaries suppress the nearby transverse hopping. Figure 23 shows some snapshots of particle configurations and the corresponding transverse density distribution for different number of layers, N . Basically, at larger N , the density profiles with their decaying oscillation from both boundaries manifest the confinement-induced (two to three) almost frozen outer layers near each boundary, which sandwich the more disordered isotropic liquid with a flat density profile in the center region. The transition to the layered structure up to the center at $N \leq 7$ is evidenced by the appearance of sharp peaks of the density profile. Similar structure was observed in a series of experiments with the so-called “dusty balls”—3D spheroidal clusters consisting of a few thousand particles, which have a shell structure (of three to four layers) near the surface and a

liquid (amorphous) state in the central bulk (Arp *et al.*, 2004).

Investigations of shear flows generated in sheared glassy materials (such as foams, micelles, dense colloids, and dense granular systems) inside mesoscopic channels show shear banding—the flow tends to separate into bands with different shear rates through local stress relaxation [see, e.g., Weaire and Hutzler (2000)]. The flow it causes the formation of the outer shear bands in which the mean shear rate, the velocity fluctuations, and the structural rearrangement rate are all enhanced, and leaves a weakly perturbed center band. Such behavior is in contrast to the mean velocity profile with a uniform shear rate for a bulk Newtonian flow between two oppositely moving parallel plates. The velocity profile depends on the rheology of the system [e.g., in foams as well as complex plasmas there is a significant shear thinning; see, e.g., Janiaud *et al.* (2006) and Sec. III.C].

Using the same experimental setup as in Teng *et al.* (2003), the atomistic dynamics of the shear flow in a quasi-2D mesoscopic complex plasma liquid has been studied by Chan *et al.* (2004). Due to the formation of the nearby layered structure shown in Fig. 23, the persistent and directional slow drive from the external stress along the boundary enhances cage-escape structural rearrangements which cascade into the liquid through a many-body interaction. It was found that the flow consists of two outer shear bands, about three interparticle distances in width, adjacent to the boundaries and a central small-shear zone. The former has higher levels of both longitudinal and transverse velocity fluctuations. The shear banding phenomenon originates from the local stress release through the local rearrangement events adjacent to the boundary.

In a different experiment, converging and diverging (“nano”)flows were investigated by Fink (2005). One of the interests here was the determination of possible “selection rules” for the flow—e.g., how in detail the system evolves kinetically from N flow lines to $N-1$ flow lines when N becomes small. A second interest was to find out if there was a preferred instantaneous “structure” of the fluid particles during the flow line transitions. An example is shown in Fig. 24(a). The flow converges by one interparticle spacing Δ over a distance of typically six Δ (i.e., reduction in one flow line), so that the convergence angle is about 10 deg. The figure shows the following features: (i) The typical structure of the fluid is hexagonal—i.e., the same as the 2D crystalline ground state. (ii) The transition from four to three flow lines goes via a localized $5/7$ dislocation. (iii) The transition from three to two flow lines goes via alternating jumps (“zipping”) of particles from the “central” flow line (which disappears) to the two outer ones. The characteristic structures observed are shown schematically in Fig. 24(b).

The results by Fink (2005) confirmed the observations shown in Fig. 23 for a plane nonconverging channel. As the system becomes smaller (in terms of flow lines) it begins to look instantaneously like a solid. This is, of course a consequence of the channel surface, which in

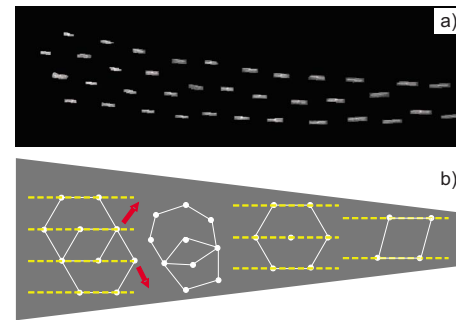


FIG. 24. (Color online) Converging 2D complex plasma flow in the limit of very few flow lines. (a) The convergence of particles of $3.4 \mu\text{m}$ diameter goes from four to two lines. The experiment was designed to investigate fluid structure and dynamical selection rules during the (discrete) flow line reduction. (b) Characteristic fluid structures observed in different regimes of the converging flow. From Fink, 2005.

these experiments is a “slip surface” (i.e., the complex plasma does not have any “wetting” properties). Experiments with rough surfaces (on the scale of the interparticle separation) have not been performed yet. In such a case we would expect surface friction to play a role with associated modification of the flow structure and dynamics.

G. Electrorheological fluids

In this section we focus on an interesting class of so-called electrorheological (ER) fluids which have acquired significant attention in the last decade. Conventional ER fluids consist of suspensions of microparticles in usually nonconducting fluids with a different dielectric constant (Chen *et al.*, 1992; Dassanayake *et al.*, 2000). The interparticle interaction, and hence the rheology of ER fluids, is determined by an external electric field, which polarizes microspheres and thus induces additional dipole-dipole coupling. The electric field plays the role of a new degree of freedom that allows us to “tune” the interaction between particles. This makes the phase diagram of ER fluids remarkably diversified (Yethiraj and van Blaaderen, 2003; Hynninen and Dijkstra, 2005).

The term electrorheological fluid is self-explanatory (Stangroom, 1983; Carlson *et al.*, 1990): At low electric fields microparticles may be fully disordered and then (provided their concentration is low as well) ER fluids may be just normal Newtonian fluids. At larger fields, however, the situation can change dramatically—due to the increased dipole-dipole attraction particles arrange themselves into strongly coupled chains (“strings,” or even “sheets”) along the field. This naturally changes the rheology—e.g., at low shear stresses ER fluids can behave such as elastic solids, while at stresses greater than a certain yield stress they are viscous liquids again. ER fluids have a significant industrial application potential—they can be used in hydraulics, photonics, display production, etc. (Stangroom, 1983; Carlson *et al.*, 1990; Yethiraj *et al.*, 2004).

In contrast to conventional ER fluids (e.g., colloids) where the induced dipoles are due to polarization of the microparticles themselves, in complex plasmas the primary role is played by clouds of compensating plasma charges (mostly excess ions) surrounding negatively charged microparticles (see Sec. II.B). Without an external field the cloud is spherical (Debye sphere), when a field is applied the cloud (which then acquires a fairly complicated shape and is called plasma wake) is shifted downstream from the particle, along the field-induced ion drift. In this case the pair interaction between charged microparticles is generally nonreciprocal (i.e., non-Hamiltonian, see Sec. II.F.1). The nonreciprocity of the interaction could only be eliminated if the wake potential were an even function of coordinates, i.e., $\varphi(\mathbf{r}) = \varphi(-\mathbf{r})$. A simple recipe to create such a reciprocal wake potential is as follows (Ivlev *et al.*, 2008): One has to apply an ac field of a frequency that is (i) much lower than the inverse time scale of the ion response (ion plasma frequency, typically $\sim 10^7 \text{ s}^{-1}$) and, at the same time, (ii) much higher than the inverse dust response time (dust plasma frequency typically $\sim 10^2 \text{ s}^{-1}$ or less). Then the ions react instantaneously to the field whereas the microparticles do not react at all. The effective interparticle interaction in this case is determined by the time-averaged wake potential. The resulting interaction is rigorously reciprocal (Hamiltonian) so that one can directly apply the formalisms of statistical physics to describe ER plasmas.

Quantitatively, the field-induced interparticle interaction in ER plasmas can be determined from the linearized dielectric response formalism (see Sec. II.B). For subthermal ion drift the interaction potential is given by Eq. (6), which represents the far-field asymptotics for the potential expanded into a series over small u_i (with the angular dependence of the first three coefficients proportional to that of the corresponding multipoles, i.e., charge, dipole, and quadrupole). Furthermore, all odd terms ($\propto u_i^j$ with odd j) are proportional to linear combinations of the odd-order Legendre polynomials whereas even terms are combinations of the even-order polynomials. Thus, for an ac field $E(t)$ with $\langle E \rangle_t = 0$, all odd-order terms disappear in the time-averaged potential $\langle \varphi \rangle_t$, which becomes an even function of coordinates. The effective energy $Q \langle \varphi \rangle_t$ of the time-averaged pair interaction is (Ivlev *et al.*, 2008)

$$W(r, \theta) \approx Q^2 \left[\frac{e^{-r/\lambda}}{r} - 0.43 \frac{M_T^2 \lambda^2}{r^3} (3 \cos^2 \theta - 1) \right]. \quad (29)$$

Thus, the effective interaction consists of two principal contributions: The first core term represents the spherically symmetric Debye-Hückel (Yukawa) part, whereas the second term is due to the interaction between the charge of one particle and the quadrupole part of the wake produced by another particle. The charge-quadrupole interaction is identical to the interaction between two equal and parallel dipoles of magnitude $\approx 0.65 M_T Q \lambda$. This implies that for small M_T the interac-

tions in ER plasmas are equivalent to dipolar interactions in conventional ER fluids.

One can compare ER colloids and ER plasmas in terms of the dipole-dipole coupling (Tao, 1993; Gulley and Tao, 1997; Hynninen and Dijkstra, 2005). Since the magnitude of the induced dipole is proportional to the volume of the polarizable sphere, the field necessary to achieve a given coupling in ER colloids will be much larger than that in ER plasmas. In colloids, microparticles of radius a acquire dipoles $\sim a^3 E_{\text{coll}}$ and are separated by distance $\sim a$, whereas the interaction in plasmas is determined by Eq. (29) with typical separation $\sim \lambda$. The equivalent field for colloids is then $E_{\text{coll}} \sim M_T (a/\lambda)^{1/2} Q/a^2$. For typical experimental conditions, the electric field $E \sim 3 \text{ V/cm}$ in plasmas (which corresponds to $M_T \sim 1$) is equivalent to $E_{\text{coll}} \sim 3 \text{ kV/cm}$ in colloids.

The recently investigated phase diagram of ER colloids reveals a variety of crystalline states (Chen *et al.*, 1992; Yethiraj and van Blaaderen 2003; Hynninen and Dijkstra, 2005; Brandt *et al.*, 2009). In addition to isotropic bcc and fcc lattices, the hcp structure can be a ground state in a fairly broad range of phase variables. Moreover, unusual anisotropic crystalline states become possible, like body-centered orthorhombic and body-centered tetragonal (bco and bct, the phase transition between them is of the second order). On the other hand, relatively little research has been done on the fluid phase. In particular, the dynamics and details of the phase transition between isotropic and string fluids is practically unexplored (Tao, 1993; Gulley and Tao, 1997).

The isotropic-to-string phase transition in ER plasmas was recently investigated in experiments under microgravity conditions (Ivlev *et al.*, 2008). Particles remained in a disordered fluid state as long as the amplitude of the applied ac field was below a certain threshold. Increasing the field further triggered rearrangement of particles: They became more ordered, until eventually well-defined particle strings were formed along the direction of the field. The transition between isotropic and string fluid states was fully reversible—decreasing the field brought the particles back into their initial isotropic state. The trend to form strings increased with particle size. The MD simulations performed with similar parameters gave remarkable agreement with the experiment.

In order to quantify the isotropic-to-string phase transition, a suitable order parameter has to be employed that is sensitive to the changing particle structures (Ivlev *et al.*, 2008). Conventional approaches, e.g., binary correlation or bond orientation functions, Legendre polynomials, etc., turned out to be too insensitive. Much more satisfactory results were obtained by implementing the anisotropic scaling index α [see, e.g., R ath *et al.* (2002)]—a local nonlinear measure for structure characterization, with which any symmetry changes can be quantified using the longitudinal and transverse distributions $P_{\parallel}(\alpha)$ and $P_{\perp}(\alpha)$. For the onset of the isotropic-to-string transition, the difference between the transverse

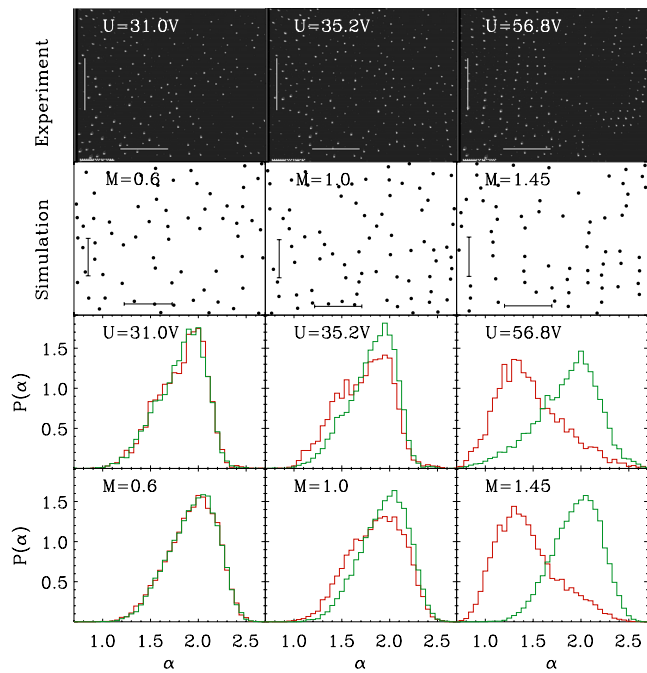


FIG. 25. (Color online) Formation of strings in ER plasmas. First row: Microgravity experiments ($6.8 \mu\text{m}$ particles, raw data), microparticles are illuminated by a thin (less than mean interparticle distance) laser sheet parallel to the applied ac electric field. Examples of low (first column), intermediate (second column), and high (third column) fields are shown, the peak-to-peak voltage of the ac signal (applied to two parallel horizontal electrodes) is indicated. Second row: MD simulations, the same configuration as in the experimental setup, the field is measured in units of the thermal Mach number M_T (scale bars correspond to 2 mm). Third and fourth rows: Histograms for longitudinal and transverse distributions of the scaling indices $P_{\parallel}(\alpha)$ and $P_{\perp}(\alpha)$ calculated for the experiment and simulation, respectively. (Note that at higher densities the particle positions in neighboring strings became highly correlated.) From Ivlev *et al.*, 2008.

and longitudinal scaling indices averaged over the ensemble, $\Delta\alpha = \int \alpha P_{\perp} d\alpha - \int \alpha P_{\parallel} d\alpha$, was used as a scalar order parameter, whereas M_T played the role of the control parameter. The data obtained were well approximated with a two-parametric fit $\Delta\alpha \propto (M_T - M_T^{\text{ct}})^{\gamma}$ for $M_T > M_T^{\text{ct}}$ and $\Delta\alpha = 0$ for $M_T \leq M_T^{\text{ct}}$, which might suggest a second-order or a weak first-order phase transition between isotropic and string fluids (Tao, 1993). Note that for a weakly coupled ER plasma, which implies gaseouslike ensembles of particles where triple interactions play a minor role, a simple analytical criterion for the isotropic-to-string phase transition can be derived from the analysis of the second virial coefficient, $B = \pi \int_0^{\infty} \int_{-1}^1 (1 - e^{-W/Td}) r^2 dr dx$ (Landau and Lifshitz, 1978), where $x = \cos \theta$ and $W(r, x)$ is given by Eq. (29).

Figure 25 summarizes the experimental results and comparison with the MD simulations (Ivlev *et al.*, 2008). The structural order of the well-developed strings is evident in both experimental and simulation data shown in the first two rows. The lower two rows show the corresponding distributions $P_{\parallel}(\alpha)$ and $P_{\perp}(\alpha)$.

To date colloidal suspensions have been the major focus for ER studies, providing a wealth of information (Chen *et al.*, 1992; Dassanayake *et al.*, 2000; Yethiraj and van Blaaderen, 2003; Hynninen and Dijkstra, 2005). The discovery that complex plasmas also have electrorheological properties adds a new dimension to such research—in terms of time-space scales and for studying new phenomena: An essentially single-species system of microparticles in complex plasmas enables us to investigate previously inaccessible rapid elementary processes that govern the dynamical behavior of ER fluids—at the level of individual particles. In particular, such investigations may allow us to study critical phenomena accompanying second-order phase transitions (Khrapak *et al.*, 2006; Kompaneets *et al.*, 2009).

H. Fundamental stability principles of condensed matter

A great deal of research has been devoted to measurements and analysis of the atomic or molecular structure of liquids—experimentally using diffraction methods (as in solids), and theoretically using MD simulations [see Reichert *et al.* (2000), Reichert (2002), and references therein]. There are also studies using other model systems, such as colloids, cold atoms in traps, and storage rings (Drewsen *et al.*, 1998; Schätz *et al.*, 2001; Anderson and Lekkerkerker, 2002). In Fig. 26(a) we show the measured distribution of Pb atoms in a melt (in 2D) including the trajectories (Reichert *et al.*, 2000; Reichert, 2002). It seems clear that instantaneously the particle structure in coordinate space is well ordered, whereas in reduced phase space it is much less ordered and becomes less so as the time between subsequent measurements is increased. This result is, of course, in accord with the reduced correlation as the distance is increased. Figure 26(b) shows a different example—a small 2D plasma crystal cluster at different couplings (Melzer, 2003; Melzer *et al.*, 2007). Here, too, we note that while instantaneously the system seems well ordered, in reduced phase space this order disappears as time increases. This phenomenon is also illustrated well in Figs. 13, 15, and 29(a) where the particle cage-escape events gradually smear out the instantaneous crystalline structure.

Figure 27 shows the measured 3D structure of lead atoms in a fluid state, also inferred from scattering experiments (Reichert *et al.*, 2000; Reichert, 2002). The pentagonal structure is quite striking (note that in the solid state Pb is bcc). There is a simple argument, due to Frank (1952), that explains this observation. First, the premise is that due to rotation the binary interaction potential between molecules in a fluid tends to average out and becomes isotropic (even for, e.g., dipolar or more complicated molecules). Next, if one considers the possible different ways in which 12 hard spheres can be arranged in simultaneous contact, counting as different only those arrangements which cannot be transformed into each other without breaking contact with the central ball, one arrives at the solution: three. The first is the well-known bcc arrangement, the second is hcp, both

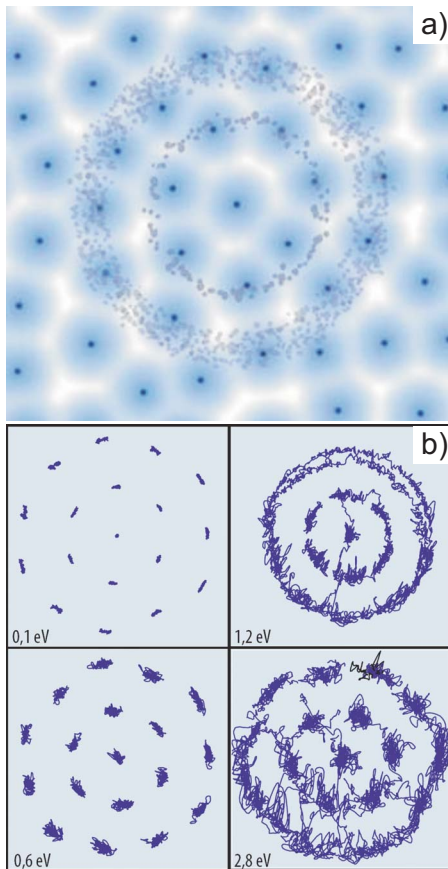


FIG. 26. (Color online) Evolution of liquid structures. (a) Instantaneous position of atoms in liquid lead. The distribution of points in the two rings around the central atom (at rest) shows the meandering of neighbors in time. From Reichert, 2002. (b) Melting of a 2D cluster in complex plasmas. The melting occurs at around 1.2 eV, a snapshot—even in the molten state—would essentially look like the structure of the crystalline state. From Melzer *et al.*, 2007.

ubiquitous crystal structures, and the third is the icosahedron. This packing has fivefold axes and the binding energy for, e.g., a Lennard-Jones-type interaction is 8.4% greater than for the two crystalline states. On the other hand, the system is not periodic, i.e., it cannot produce large-scale translational or orientational order. It appears logical, therefore, to assume that liquid 3D

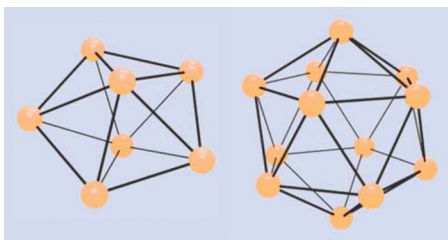


FIG. 27. (Color online) Local fivefold symmetry structures observed in a liquid lead. Such measurements show that crystals and liquids do not share similar structural properties—an important finding for understanding the fundamental stability principles of condensed matter. From Reichert, 2002.

structure is dominated by this pentagonal local order (at least when the repulsive part of the binary interaction is sufficiently short ranged). This line of argument implies that the fundamental stability principle governing instantaneous local structure of fluids is simply geometrical, and that this is possibly due to the isotropization of the molecular interaction potential as a consequence of the rotational degrees of freedom (which does not occur in rigid crystals, of course).

It is noteworthy that in undercooled fluids with purely repulsive interactions the self-organization of molecules into icosahedral “clusters” also cannot be excluded (Wette *et al.*, 2009): Based on entropy considerations (Frenkel, 1999), one can argue that when the average packing fraction of molecules is high enough (but still below the glassy limit), the free volume for such a compact cluster should be larger than the free volume for individual molecules in a disordered phase. The total entropy of fluids with the icosahedral local order then might be larger as well, thus making them thermodynamically preferred.

Observations of complex plasmas contribute to the understanding of the kinetics of liquids and to the fundamental stability principles in at least three ways: (i) by investigating liquids in six-dimensional (6D) phase space $f(\mathbf{r}, \mathbf{p}, t)$, (ii) by investigating constrained systems (2D and nanoflow situations), and (iii) by investigating systems with externally tuned anisotropic interaction potentials. So far, little work has been done in this field, however, in spite of the fact that complex plasmas are possibly the best suited candidates for an in-depth study.

The main results obtained so far have come as a by-product of other investigations, in particular 2D studies. The remarkable feature of such constrained systems is that there is no distinct local fluid structure. This is seen in the investigations into self-organization and scaling in 2D crystallization (see Sec. III.I.2), where the prevailing local structure is always hexagonal—and, as the system is less coupled, the only effect on the local structure is an increase of 5/7 dislocation pairs. It is also seen in confined flows, in particular when the flow channel is only a few flow lines (or mean particle spacings) wide, as shown in Sec. III.F.

Now, in the context of Frank’s argument mentioned above, this is easy to understand. In 2D the arrangement of “billiard balls” around one central ball, all of them touching, happens to be 6—not 5, not 7, nor any other number. Therefore, the tentative conclusion for particles with isotropic interaction potentials is that the fundamental stability criterion is purely topological, defined by the geometry of the system and not by the properties of the system itself. This is an important generic hypothesis, which should be investigated further in particular using anisotropic systems (e.g., electrorheological effects, see Sec. III.G). Further, by investigating the systems in 6D phase space, one can determine whether higher order effects may play a role, and if so how they would manifest themselves.

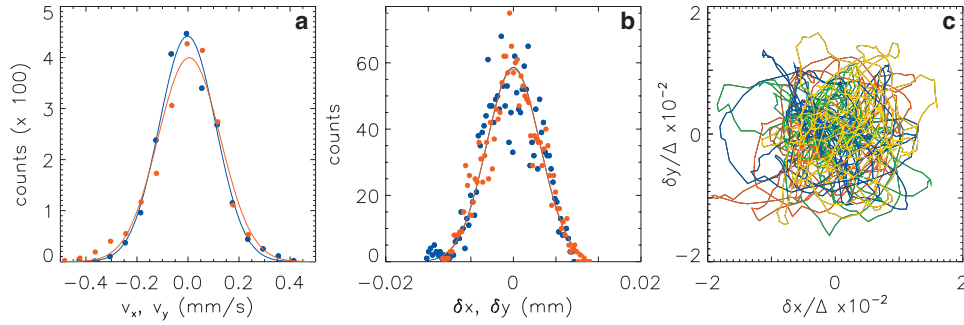


FIG. 28. (Color) Dynamics of particles in a lattice of a 2D crystal. (a) Distribution of velocities v_x (red dots) and v_y (blue dots) with Maxwellian fits (solid lines). (b) Distribution of displacements x (red dots) and y (blue dots) of particles in their nearest-neighbor cage, solid lines are Gaussian fits. (c) Particle trajectories in their respective nearest-neighbor cells during the measurement time of ≈ 12.3 s (colors-correspond to the progression of time). Particles are of $9.19 \mu\text{m}$ diameter. From [Knapek, Ivlev, et al., 2007](#).

I. 2D crystals

Next we concentrate on the kinetic description of the crystalline state in complex plasmas, with the focus on various dynamical aspects that may have generic nature and therefore play an important role in regular solids. We start with the kinetic characterization of crystals—the approach which, in principle, is equally appropriate for 2D and 3D cases. Then we proceed with different crystallization scenarios peculiar to 2D and 3D (Sec. III.J) systems. We also discuss creation and dynamics of dislocations—the process that is absolutely relevant for 3D crystals as well, but has been properly investigated so far only in 2D plasma crystals.

1. Kinetic characterization of crystals

Transitions between solid and fluid phases as well as between different crystalline states, rheological and transport properties of the fluid phase, energy relaxation, and hierarchy of metastable states are determined by the magnitude of the coupling parameter Γ [see Eq. (11)], which can be also considered as the measure of (inverse) temperature. In turn, Γ depends sensitively on local variations in crystal structure, and provides information about the occurrence of localized excited states and nonstationary processes.

The value of Γ can be determined experimentally ([Knapek, Ivlev, et al., 2007](#)), by linking the individual particle dynamics with the local density and crystal structure using the Einstein frequency Ω_E (see Sec. II.D), which refers to linear oscillations of individual particles (atoms) in a lattice. In local equilibrium, the dynamics of individual particles in each lattice cell is statistically equivalent and can be described by, e.g., a Langevin equation ([van Kampen, 1981](#)). Therefore, cells represent a canonical ensemble with the Maxwell-Boltzmann distribution, $\propto \exp[-m_d(v^2 + \Omega_E^2 r^2)/2T_d]$, as shown in Fig. 28. Then one can deduce thermodynamic characteristics locally, from the independent Gaussian fit of the velocity and displacement distribution: The velocity dispersion is T_d/m_d and the displacement dispersion is $T_d/m_d\Omega_E^2 \equiv \Delta^2/\tilde{\Gamma}$, where $\tilde{\Gamma} = (\Omega_E/\Omega_{pd})^2\Gamma$ is the effective coupling parameter modified by the screening (the

ratio of the Einstein to the dust-plasma frequency is a function of the screening parameter κ only, see Sec. II.D). For such a linear description to hold, it is essential that particles in the lattice perform sufficiently small oscillations. The role of anharmonic effects can then be neglected so that the oscillations of the neighboring particles are uncoupled and can be treated independently.

An exemplary map of $\tilde{\Gamma}$ measured in a 2D plasma crystal is shown in Fig. 29(a). This map can be used to probe correlations with various local processes occurring in a crystal. For instance, there is a 5/7 dislocation just outside the regime analyzed (the position is marked by a circle), and there is some indication that the coupling strength in the vicinity of a nonstationary cage-escape event is substantially decreased. At the same time, comparison with the density map [see Fig. 29(b)] shows no correlation.

The interparticle spacing $\tilde{\Gamma}$ shown in Fig. 29(b) varies by about 0.5% per cell so that the 2D density inhomogeneities are about 1% per cell. Performing independent measurements of the longitudinal and transverse acoustic modes (viz., acoustic velocities $C_{l,t}$; see Sec. II.D) that are very sensitive to the screening parameter κ ([Fortov et al., 2005](#), one can obtain a map of the coupling param-

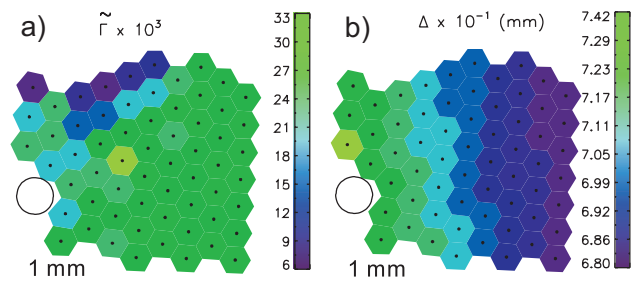


FIG. 29. (Color) 2D maps of local crystal parameters. Distribution of (a) effective coupling parameter $\tilde{\Gamma}$ and (b) interparticle distance Δ is shown, the Voronoi cell around each particle is color coded according to the value of the measured quantity. Circles indicate the position of a sevenfold-fivefold pair defect, blue cells seen at the upper edge of (a) are due to the particle cage-escape event (see Sec. III.B). From [Knapek, Ivlev, et al., 2007](#).

eter Γ (rather than $\tilde{\Gamma}$) and thus define the state of the crystal within the phase diagram (see Fig. 7).

A straightforward application of the method described above could determine the local Lindemann criterion of crystal melting, viz., what is the critical magnitude of the mean squared displacement, what are the characteristic patterns of the caged particle motion in the vicinity of the melting transition, what is the role of dynamical heterogeneity, etc.

2. Scalings in 2D crystallization

Characterization of solid, supercooled (glassy), and liquid states is, in general, not straightforward. Different models for the solid-liquid phase transition have been put forward. For 2D systems, models of particular relevance are the dislocation theory of melting—the Kosterlitz-Thouless-Halperin-Nelson-Young (KTHNY) theory [which involves two phase transitions—with an intermediate, so-called hexatic phase in between—one associated with the unbinding of dislocation pairs and the other with the unbinding of disclination pairs, Kosterlitz and Thouless (1973); Halperin and Nelson (1978); Nelson and Halperin (1979); Young (1979); Nelson (2002)], and the theory of grain-boundary-induced melting (Chui, 1982, 1983).

Apparently, one of the central questions in understanding phase transitions in 2D strongly coupled systems is what are the critical parameters that determine which melting scenario will be realized in a particular experiment (i.e., whether the melting occurs in accordance with the KTHNY scenario, or the transition is preempted by grain-boundary-induced melting). The accompanying questions are whether the correlation functions associated with the crystal and hexatic phases have the appropriate scaling behavior, and what the order is of the observed phase transitions in the thermodynamic limit. These issues have been discussed extensively [see, e.g., reviews by Strandburg (1988) and by Alba-Simionesco *et al.* (2006)].

It is generally believed that the value of the defect core energy plays a critical role in the realization of the melting scenario (Strandburg, 1988). The KTHNY mechanism should operate when the core energy exceeds $\approx 2.8T_{M1}$ (where T_{M1} is the temperature of unbinding of dislocation pairs), otherwise grain-boundary-induced melting should occur. Below we focus on two experiments that illustrate the kinetics accompanying these melting mechanisms.

The experiments by Zahn and Maret (2000) performed with colloidal particles are an example of the KTHNY scenario [for other examples, see, e.g., Murray and Winkle (1987); Marcus and Rice (1997)]. Supermagnetic spherical colloids were confined by gravity to a horizontal flat water/air interface and their interaction potential was controlled via a vertical magnetic field B , which induced a magnetic moment χB , with χ the effective magnetic susceptibility. This repulsive dipole-dipole potential dominated the interaction and the coupling parameter is $\Gamma = (\chi B)^2 (\pi n)^{3/2} / T_d$, where n is the surface

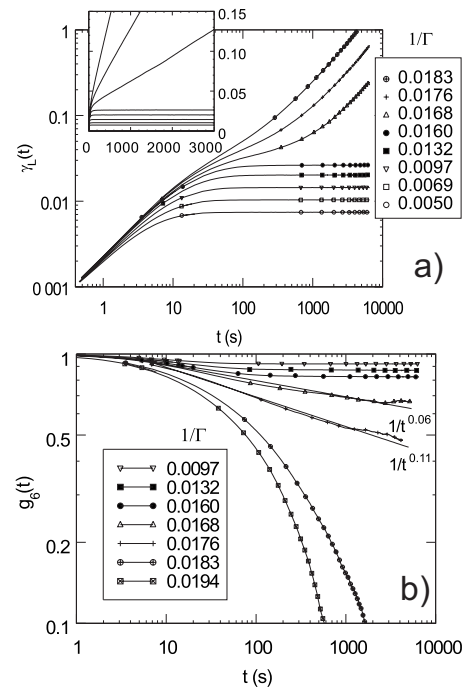


FIG. 30. Melting in 2D colloids. (a) Dynamic Lindemann parameter $\gamma_L(t)$ for different values of the temperature Γ^{-1} . In the crystalline phase the long-time limit of $\gamma_L(t)$ is bounded while it diverges in the liquid phase. The inset shows the data in a linear plot to illustrate the change in the behavior of $\gamma_L(t)$. (b) The bond-order correlation function in time $g_6(t)$. Particles are of $4.7 \mu\text{m}$ diameter. From Zahn and Maret, 2000.

fraction of the particles. Thus changing the magnetic field strength allows external tuning of the coupling parameter and the study of phase transitions in a controlled way. The data obtained with video microscopy (about 2000 particles) were analyzed in terms of displacements and correlation functions. Figure 30(a) shows the temporal evolution of the 2D modified Lindemann parameter $\gamma_L \propto \langle [\delta \mathbf{r}_{\text{rel}}(t)]^2 \rangle$, calculated using the relative neighbor-neighbor displacement $\delta \mathbf{r}_{\text{rel}}$. The crystalline regime at $\Gamma \gtrsim 62.5$ has bounded values for the mean square displacement (normalized to the lattice constant) whereas the liquid phase diverges as $t \rightarrow \infty$.

Figure 30(b) shows the bond order correlation function $g_6(t) = \langle e^{i6\theta(t)} \rangle$ as a function of time, where $\theta(t)$ denotes the angle fluctuation of a fixed bond. Three regimes can be identified: The crystalline regime at $\Gamma \gtrsim 62.5$, where $g_6 = \text{const}$, the isotropic liquid regime at $\Gamma \lesssim 54.6$, where $g_6(t)$ decays exponentially, and an intermediate regime at $56.8 \leq \Gamma \leq 59.5$, where $g_6(t)$ decays as a power law, indicating the hexatic phase. These findings are in good agreement with the KTHNY theory, supporting the two-stage melting for systems with a r^{-3} interaction potential (the core energy occurs above the critical value of $2.8T_{M1}$).

Melting via grain boundaries was seen in several experiments with complex plasmas (Melzer, Homann, and Piel, 1996; Quinn *et al.*, 1996; Knapek, Samsonov, *et al.*, 2007; Nosenko *et al.*, 2009). We consider the recent ex-

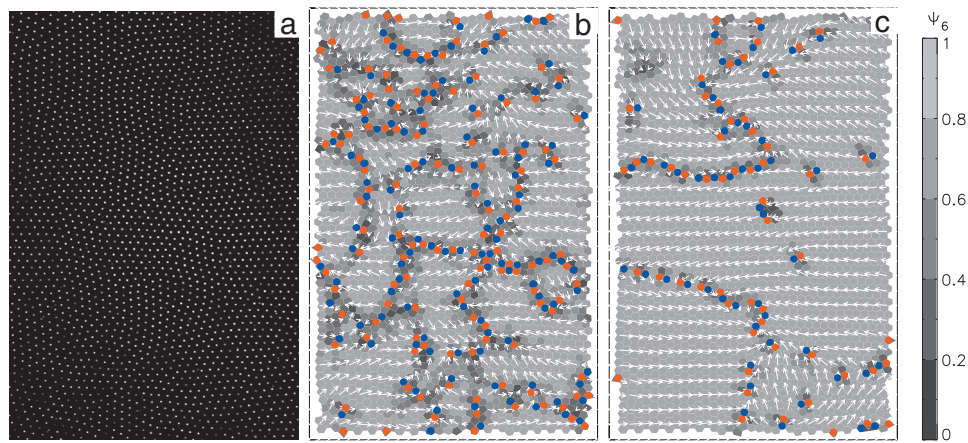


FIG. 31. (Color) Recrystallization in 2D complex plasmas. (a) Snapshot of the intermediate structure of $9.19 \mu\text{m}$ particles during the recrystallization. (b), (c) Color-coded 2D maps for two consecutive stages of recrystallization [about 10 s apart, map (b) corresponds to snapshot (a)]. The background gray scale corresponds to the local value of the bond-orientational function $|\psi_6|$, the arrows represent the vector field of ψ_6 on the complex plane, defects are marked by red (fivefold) and blue (sevenfold) dots. Adapted from Knapek, Samsonov, *et al.*, 2007.

periment by Knapek, Samsonov, *et al.* (2007), where a 2D monolayer of about 3400 particles was first allowed to crystallize, and then it was perturbed and melted by an electric impulse. The subsequent re-crystallization was recorded with high spatial and temporal resolution (see Fig. 31). To compare with the KTHNY theory, the local variation in orientational ordering was investigated by calculating the bond-orientational function $\psi_6 = \frac{1}{n} \sum_j e^{i6\theta_j}$ over the n nearest neighbors for each particle, with θ_j the angle between the nearest-neighbor bond and a reference axis. The modulus $|\psi_6|$ of this complex quantity yields the bond order parameter, which is unity for an ideal hexagonal structure, and the argument $\arg(\psi_6)$ is a measure for cell orientations with respect to the reference axis. The kinetic temperature of the system was defined from the velocity distribution of the particles (by fitting with a Maxwell-Boltzmann distribution, see Fig. 28).

Figures 31(b) and 31(c) shows color-coded maps of $|\psi_6|$ for two consecutive stages of recrystallization. The location of jumps in bond orientation is correlated with the lines of (fivefold or sevenfold) defect locations. After melting, as the system cools down, the crystalline domains grow and merge with neighboring regions, as shown in Fig. 31(b), causing the bonds to tilt to the (single) orientation of the growing region. Eventually, a metastable state shown in Fig. 31(c) is reached which is characterized by highly ordered adjoined crystalline domains.

The dynamic evolution of the lattice defects can be summarized as follows: (i) The instantaneous 2D structure revealed mainly hexagons, pentagons, and septagons at all temperatures sampled. (ii) The fraction of pentagons and septagons was identical within the statistical uncertainties—they always appear in pairs. (iii) The hexagonal ground state (also the lowest energy state) dominated at all temperatures sampled. (iv) The local disorder, identified as the fraction of pentagons or sep-

tagons, was approximated by a power-law dependence on temperature, as shown in Fig. 32.

These facts indicate that unlike 3D liquids, which may have their own distinct local order (pentagonlike, see Fig. 27)—quite different from the crystalline state—2D liquids do not exhibit a special local order. They can appear as a crystal with different amounts of lattice dislocations, which depend on the temperature. As the temperature decreases, these dislocations may partially annihilate (anneal) and also have a tendency to form strings, which act as domain boundaries separating homogeneous ordered regions.

The implications of these experimental findings are as follows:

- They show that the fundamental stability principles of condensed matter depend on the external constraints—in such a way that for 2D systems the self-organization favors mixtures of the ground state and the next most excited states.

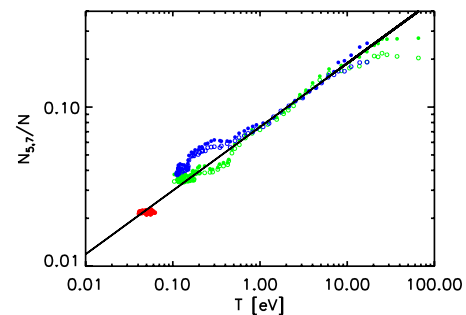


FIG. 32. (Color online) Fraction of the fivefold and sevenfold defects $N_{5,7}/N$ during the recrystallization. As temperature decreases, the number of defects in a hexagonal lattice obeys a power-law dependence, $N_{5,7} \propto T_d^{0.4}$ (solid line), revealing a classic scale-free behavior. Different colors represent three different experiments. Adapted from Knapek, Samsonov, *et al.*, 2007.

- Furthermore, the power-law behavior with respect to the order parameter temperature shows that there is no characteristic scale.
- If these findings are generic (perhaps for a certain class of materials) then they are significant for characterizing physical properties and ultimately for monolayer, membrane, and nanoengineering.
- To understand whether the findings have generic implications, we need to develop a kinetic theory that has a sufficiently general character to allow extrapolation to other systems.

a. Temperature scaling for domain boundaries

Given the above findings one can develop a simple theory that describes this process of self-organization. This theory is based on the early work of [Frenkel \(1955\)](#).

At a given temperature, a 2D system of N particles is divided into $z = N/\bar{N}_d$ homogeneous domains, each containing \bar{N}_d particles on average, with boundaries made up of pairs of pentagons and septagons. We assume that the structural order in the individual domains is uncorrelated. While it is clear that there will be a spectrum of domain sizes, for the moment we only consider averages (the justification for this approach will become apparent later).

If the mean separation between the particles is Δ , then the mean domain radius is determined by $\pi\bar{r}^2 = \pi(\Delta/2)^2(N/z)$, i.e., $\bar{r} = \frac{1}{2}(N/z)^{1/2}\Delta$. The interfaces have an additional amount of line energy $\bar{E} = 2\pi\bar{r}z\sigma$, where σ is the line tension (the interaction between domains is neglected). Substituting for \bar{r} gives $\bar{E} = \pi\Delta(Nz)^{1/2}\sigma$. As a result of the domain structure, the system entropy increases. The measure of disorder is characterized by the number of different ways in which the particles may be organized (assuming homogeneity inside each domain), $P = N! / [(N/z)!]^z$. If N and N/z are sufficiently large, then using Stirling's approximation yields $P \approx z^N$. The entropy is $S = \ln P$ and the mean free Helmholtz energy is accordingly $\bar{F} = \pi\Delta(Nz)^{1/2}\sigma - NT_d \ln z$. Assuming that during recrystallization the system always remains in thermodynamic equilibrium, from $\partial\bar{F}/\partial z = 0$ we have

$$z = (2T_d/\pi\Delta\sigma)^2 N.$$

Remarkably, z does not depend on \bar{N}_d , the mean particle population of a domain. We have now established a relationship between z and T_d . At this stage we can introduce the fractal nature of the domains as a hypothesis. This hypothesis is also intended to account for the size distribution of the domains, which we have not explicitly discussed. We write $\bar{N}_d\Delta^2 = \text{const} \times (\bar{N}_s\Delta)^{1+\alpha}$, where \bar{N}_s is the average number of particles in a domain wall. (Note that with the above definition we have $\alpha=1$ if the domain was circular, whereas for long narrow strip domains $\alpha \rightarrow 0$, which suggests that $0 < \alpha < 1$.) Substituting this scaling yields finally the total number of particles in

all domain boundaries $N_{\text{tot}} (= N_5 + N_7) \equiv z\bar{N}_s$, which obeys the scaling $N_{\text{tot}}/N \propto T_d^{2\alpha/(1+\alpha)}$. From the measurements we have $2\alpha/(1+\alpha) \approx 0.4$, which gives $\alpha \approx 0.25$ if σ is temperature independent (obviously, if σ is temperature dependent then α becomes larger than 0.25). The obtained fractal exponent lies in the expected range $0 < \alpha < 1$, but no physical argument has been obtained so far regarding its specific value. This could imply that α may be material dependent.

Thus, it is possible to explain observing the recrystallization of a 2D plasma crystal with simple thermodynamic arguments, provided the following major assumptions are satisfied: (i) The system is instantaneously in thermodynamic equilibrium. (ii) The evolution takes the form of uncorrelated domains with size and number depending on temperature. (iii) Domain boundaries are always of the same type (here 5/7 dislocations). (iv) The domain lines satisfy on average a constant fractal relationship, independent of temperature. (v) The line tension of the domain boundaries is temperature independent (or has a power law dependence on T_d). (vi) The free energy of the domain walls dominates the system evolution.

3. Dynamics of dislocations

Even far above the melting line, dislocations are ubiquitous in both 2D and 3D crystals. Dislocations are essential for understanding such properties as plasticity, yield stress, susceptibility to fatigue, fracture, etc. Their generation and motion is of interest in materials science ([Kittel, 1961](#)), the study of earthquakes and snow avalanches ([Kirchner et al., 2002](#)), colloidal crystals ([Schall et al., 2004](#)), 2D foams ([Abd el Kader and Earnshaw, 1999](#)), and various types of shear cracks ([Rosakis et al., 1999](#); [Abraham and Gao, 2000](#)).

In elastic theory, a dislocation's core is treated as a singularity in an otherwise continuous elastic material. Such a simplified approach is often too crude to capture essential quantitative characteristics of dislocations, whose scales are usually of the order of the lattice constant. In regular solids dislocation dynamics is almost impossible to study experimentally at an atomistic level ([Murayama et al., 2002](#)) because of the small distances between the atoms (or molecules), high characteristic frequencies, and the lack of experimental techniques of visualizing the motion of individual atoms.

In contrast to regular solids, complex plasmas turned out to be an exceptionally suitable model system for experimental study of the discrete structure and dynamics of dislocations. In the experiment by [Nosenko et al. \(2007\)](#) a 2D plasma crystal was heavily stressed due to inhomogeneous (parabolic) radial confinement. That was the reason for the strong variation in the number density across the crystal and, as a consequence, for the appearance of topological defects [shown in [Fig. 33\(a\)](#)]. Most of the defects formed linear chains that constitute domain boundaries in the crystal. During the course of the experiment, dislocations (i.e., isolated pairs of five-fold and sevenfold defects) were continuously generated

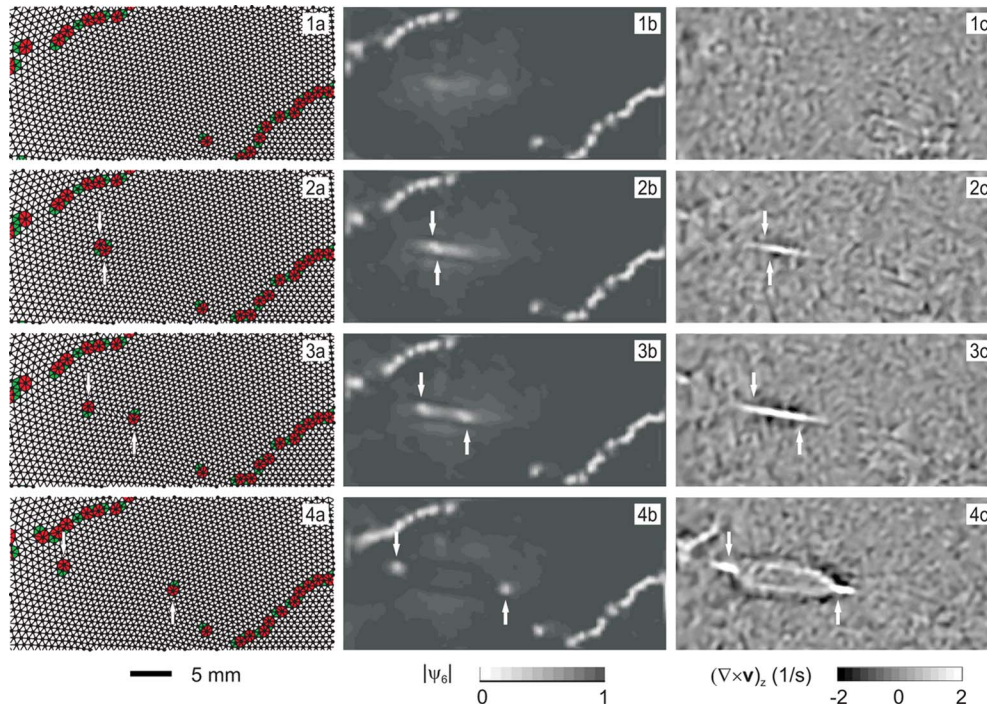


FIG. 33. (Color online) Generation and dynamics of dislocation pairs in a 2D plasma crystal. Maps of (a) triangulation of the particle positions, (b) bond-orientational function $|\psi_6|$, and (c) vorticity $(\nabla \times \mathbf{v})_x$ are shown for four different instants of time: (1) 0.33, (2) 0.57, (3) 0.70, and (4) 1.00 s. A pair of dislocations is indicated by arrows, (a) fivefold and (b) sevenfold defects are shown. Particles are of $8.09 \mu\text{m}$ diameter. From [Nosenko et al., 2007](#).

due to the shear introduced by a slow rotation of the crystal. The dislocations then moved around and finally annihilated with each other or with domain boundaries.

In order to characterize dislocations at the discreteness limit, one has to relate discrete and continuous measures of shear deformation. The most appropriate discrete measure (which is, at the same time, insensitive to uniform compressions, rotations, translations, etc.) is the modulus of the bond-orientational function $|\psi_6|$ shown in Fig. 33(b). In the limit of weak simple shear, the following relation can be used ([Nosenko et al., 2007](#)): $|\psi_6| \approx 1 - 9\gamma^2$, where γ is the shear strain. For weak pure shear, $|\psi_6| \approx 1 - 2.25e^2$, where e is the elongation, which is the measure of pure shear deformation. The dislocation dynamics can be conveniently characterized in terms of 2D vorticity $\nabla \times \mathbf{v}$ shown in Fig. 33(c) (where \mathbf{v} is the particle velocity).

Figure 33(b) shows that the shear strain had a nonuniform distribution. It was higher (i.e., $|\psi_6|$ lower) in two kinds of locations. First, it was high in domain boundaries—the two nearly parallel bright stripes in Fig. 33(b) [or equivalently the chains of fivefold and sevenfold defects in Fig. 33(a)]. Second, a diffuse background of shear strain appeared between the domain boundaries. The diffuse shear strain increased with time. When it locally exceeded a certain threshold, a pair of edge dislocations was created in that location, as one can see in the second row of Fig. 33; these dislocations appear as bright spots in (b) or as pairs of fivefold and sevenfold defects in (a), all indicated by arrows. Once a pair of dislocations was created, they moved rapidly apart (third

and fourth rows). The Burgers vectors in such a pair were oppositely directed and equal in magnitude so that the total Burgers vector was naturally conserved.

Creation of dislocation pairs is characterized by several distinct stages in the evolution of the shear strain: First, the shear strain builds up gradually in a certain location. Second, when the shear strain in this location exceeds a threshold, a pair of dislocations is created. Third, the shear stress is rapidly relaxed when the dislocations separate, and gradually drops to the background level. This cycle then starts over again, perhaps in a different location.

Dislocations that move supersonically create clear signatures—Mach cones that can be seen in Fig. 33(c), fourth row (see also Fig. 6). The Mach cones were composed of shear waves and not of compressional waves because they were excited by dislocations moving faster than the transverse acoustic velocity C_t but slower than the longitudinal one C_l . The average speed of supersonic dislocations in the experiment was about $2C_t$. In fact, linear elastic theory predicts that a gliding edge dislocation cannot overcome the sound speed of shear waves C_t because the energy radiated by a moving dislocation becomes infinite at this speed. However, gliding edge dislocations moving at the speed of $1.3C_t$ – $1.6C_t$ were observed in atomistic computer simulations ([Gumbsch and Gao, 1999](#)). The results reported by [Nosenko et al. \(2007\)](#) provide the first experimental evidence that dislocations can indeed move faster than C_t .

J. 3D crystals

Measuring the steady-state 3D crystal structure in conventional solids is well established and relatively easy. It can be done using x-ray diffraction, scanning probe microscopy, coherent electron diffraction, etc. The advantage of crystals is their stability and order, which compensates to some extent for the small (atomic) size resolution. From the crystal structure it is already possible to classify material properties and the main interactions that lead to self-organization. Consequently, determination of the bulk crystal structure, crystal surfaces (important for many chemical properties), and lately with increasing interest nanocrystal structures (which gives important clues about possible size-dependent new properties) is an important area of physics, linking material (mechanical) properties, electrical properties, superconductivity, and chemical properties (Zhu *et al.*, 1987; Gleiter, 1989, 2000; Yokoyama *et al.*, 2005; Takagiwa *et al.*, 2006).

Another important area, where crystal structures play a role, is the self-assembly of colloids. This feature is interesting because colloidal crystals can be used for, e.g., photonics, optical sensors, waveguides, chemical sensing, and lithography (Holtz and Asher, 1997; Wijnhoven and Vos, 1998; Xia *et al.*, 2000). But colloidal systems are also used to model generic properties of solids and liquids, melting, freezing, and glass transitions (Hachisu *et al.*, 1973; Pusey and van Meegen, 1986; Kegel and van Blaaderen, 2000; Pham *et al.*, 2002; Leunissen *et al.*, 2005). The fact that their phase behavior is similar to that of some simple atoms or molecules make them invaluable tools for studies at the individual particle level—with the associated transfer of new insights into natural atomic (molecular) systems that cannot be resolved in such detail.

Of course, in the last ten years or so there have been tremendous advances in the experimental investigation of dynamical effects in natural crystals too. Here the fundamental processes on the atomic or molecular level, such as vibrations and rotations in molecules or bond breaking occur on time scales of femtoseconds to picoseconds, and ultrafast optical spectroscopic techniques are needed for their resolution (Rose-Petruck *et al.*, 1999). Similarly, associated structural rearrangements of particles in perturbed crystal lattices (e.g., due to phonon propagation) can be resolved using subpicosecond x-ray diffraction (Yazaki *et al.*, 2002)—truly remarkable achievements.

These developments now open up the possibility to directly compare (and re-scale) measurements made at dynamical frequencies using plasma crystals and natural systems. In particular, one can investigate induced perturbations (e.g., phonons, solitons, and shocks; see Sec. II.D)—at least in principle, and compare the scaling relations (in terms of the natural frequencies of the systems). Such work has not been carried out so far, but technologically this is an exciting field for the future. For instance, if we wish to investigate non-Hamiltonian effects in plasma crystals (see Sec. II.F.1), it is important to

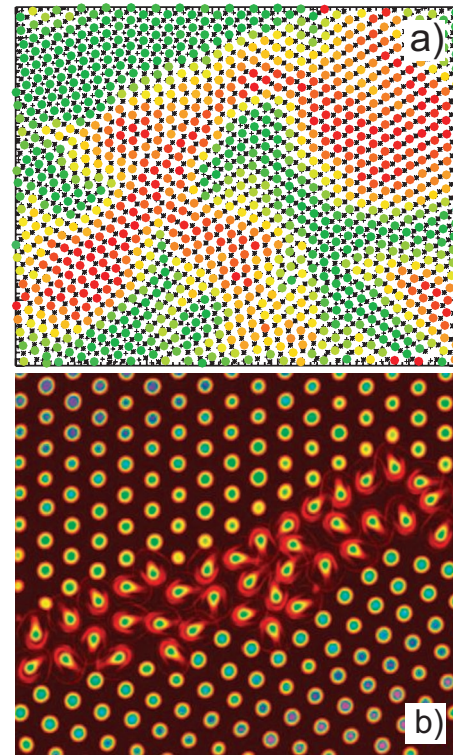


FIG. 34. (Color) Domain structure of 3D crystals. (a) Structure of a plasma crystal. Particles are of $3.38 \mu\text{m}$ diameter, three consecutive lattice planes are shown, each particle in the middle plane is color coded in accordance with the local order, (red corresponds to the fcc lattice cell and green to hcp), (particle in two adjacent planes are indicated by crosses and stars. From Zuzic *et al.*, 2000. (b) Domain interface in a crystalline colloid. Near such interfaces (grain boundaries) the crystal is premelted—the particles move rapidly and show liquidlike diffusion (red-represents the most-movements, violet is for the least). From A. Alsayed and A. Yodh.

make suitable comparisons with Hamiltonian natural crystals—to mention only one topic of interest.

To illustrate the possibilities for such research, we show two analyses of plasma crystal experiments. The first [Fig. 34(a)] corresponds to a lattice structure determination of a 3D plasma crystal, color coded onto a single lattice plane. The colors indicate different lattice structures found locally, in a single cell around each particle. We see the coexistence of the (presumable) ground state (fcc) and a metastable state (hcp), which seems to mark the domain borders (Zuzic *et al.*, 2000). Such borders are also seen between domains of the same structure but different lattice orientation—they appear to be similar to those observed in colloids [Fig. 34(b)]. Figure 35 shows an overview 3D image of a plasma crystal, where the particles are also color coded according to the local lattice structure.

1. Kinetics of 3D liquid-solid phase transitions

Crystal growth is an important branch of industry, with numerous applications ranging including semiconductors, substrates for high-temperature superconduct-

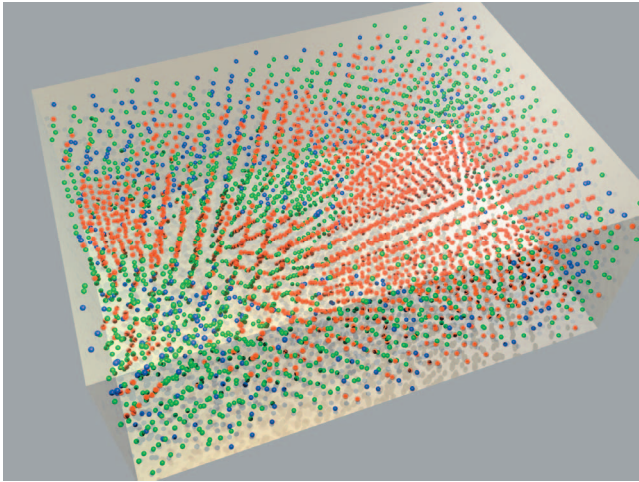


FIG. 35. (Color) 3D image of a plasma crystal. Individual particles of $\approx 1.3 \mu\text{m}$ diameter are shown from the experiment performed under microgravity conditions. Each particle is color coded in accordance with the local order (deduced with the bond-orientational invariants): red corresponds to the fcc lattice, green—to the (metastable) hcp, and blue—to the particles without apparent crystalline order (fluid, domain boundaries, defects, etc.). From P. Huber.

ors, piezo sensors, ferroelectric memories, optical elements to nanostructures, quantum dots, and organic systems. There are different facets to crystal growth, homogeneous nucleation, heterogeneous nucleation, epitaxial growth, molecular beam epitaxy, chemical vapor deposition, etc. While techniques for visualization (and quality control) of crystal growth have greatly improved, the detailed kinetic understanding of dynamical growth processes is still far from complete. The same holds for nanoparticle and microparticle contamination in production processes.

For a deeper understanding of the kinetics of crystal growth, use of model systems that allow visualization in real space and time at the individual particle level are desirable. It is no surprise, therefore, that colloidal suspensions have been widely studied in the past in order to learn more about the generic properties of self-organization [see, e.g., Vlasov *et al.* (2001); Alsayed *et al.* (2005), and references therein]. The only essential limitation of colloids for this purpose is the damping by the suspension fluid, which makes it practically impossible to investigate atomistic dynamics.

With the discovery of plasma crystals, a new system became available for studying the fully resolved dynamics of self-organization processes. Research into 3D crystallization may benefit from this, and consequently a number of studies have been conducted, beginning with the investigation of basic crystal properties [3D crystal structure, acoustic modes, etc.; see Zuzic *et al.* (2000); Zhdanov, Nunomura, *et al.* (2003)] and the liquid-solid phase transitions (Thomas and Morfill, 1996; Rubin-Zuzic *et al.*, 2006).

Based on available experimental data one can claim that there are two distinct macroscopic scenarios of crys-

tallization in 3D complex plasmas. These can be referred to as “uniform nucleation” and “crystallization front,” and which pathway is realized in the experiment depends heavily on the boundary conditions. If the (initially) liquid complex plasma is brought into the regime corresponding to a solid phase in Fig. 7 (say, by increasing the particle number density) then in the bulk region, where boundaries play no role, the system usually develops towards the uniform nucleation (although sometimes particles form a visibly amorphous solid; whether this is a 3D glassy state or not, still needs to be clarified). In this case, one normally observes coexistence of mesoscopic crystalline domains of different structure and orientation, similar to nanostructured regular solids (Gleiter, 1989, 2000). A typical example of such domains is shown in Fig. 34. However, closer to the complex plasma boundaries, when a steep potential well exists (e.g., plasma sheaths close to rf electrodes) the crystallization often develops in the form of a front propagating from boundaries inwards into the particle cloud. Apparently, a steep boundary in this case facilitates formation of a hexagonal substrate which then triggers the propagating layer-by-layer crystallization process (Rubin-Zuzic *et al.*, 2006).

Below we review recent measurements of the dynamical evolution and kinetic structure of a 3D crystallization front (Rubin-Zuzic *et al.*, 2006) and relate this to theoretical models. The first two images of Fig. 36 show a slice through a 3D complex plasma crystallization front. One can see a number of features, such as the detailed (kinetic) structure of the front and different crystal domains with different structure and/or orientation.

We focus on two particular features, which could be generic for a certain class of substances—in both the liquid and solid phases. These are the discovery of a distribution of small droplets in the crystal phase and small crystallites in the fluid phase (henceforth called *phaselets*) that are seen in the last image of Fig. 36, and a narrow (few lattice distance extent) premelted region in the crystalline regime (perpendicular to the front) where particles exhibit enhanced mobility signifying interfacial melting.

a. Phaselets

Figure 37 summarizes the measured characteristics of phaselets. Due to the special kinetic observations possible with complex plasmas, these features could be resolved down to sizes of a few particles. There are two general features worth noting: (i) The size spectra of both droplets and crystallites are compatible with power laws (Fig. 37, right column). This suggests that within the observable parameter range (~ 10 to $\sim 10^3$ particles) there is no characteristic length scale that determines either formation or dissolution. (ii) The larger crystallites and droplets tend to live longer (Fig. 37, left column). By lifetime we mean the growth+dissolution phases so that this result is not too surprising. There is, however, a substantial spread in the individual lifetimes.

At first sight, the development of the crystallites can be explained in terms of the thermodynamics: If we

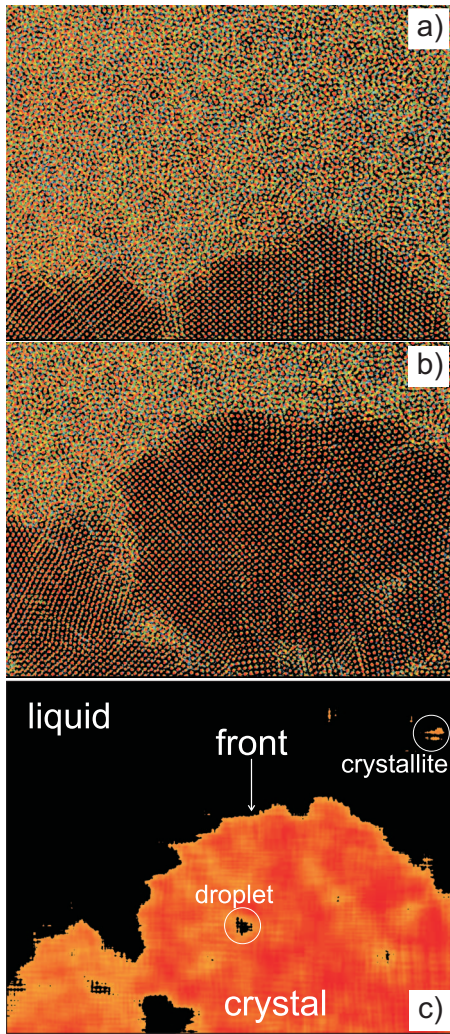


FIG. 36. (Color) Crystallization front in a 3D complex plasma. (a), (b) The front propagating upwards (images are about 16 s apart from each other). Each panel is a superposition of 10 consecutive video frames (about 0.7 s), particle positions are color coded from green to red, i.e., caged particles appear redder, “fluid” are multicolored. (c) The local order for (b), where red implies high crystalline order, black denotes the fluid phase, and yellow indicates transitional regions. Along with the crystallization front, droplets and crystallites are seen that may grow and then dissolve again. Particles are of $1.28 \mu\text{m}$ diameter. Adapted from Rubin-Zuzic *et al.*, 2006.

naturally assume the temperature (in both the liquid and crystalline regimes) below the melting point T_M , then the evolution of seed crystallites (which always form due to random fluctuations) is determined by the competition between a decrease in the bulk free energy and an increase in the surface energy. If the seed crystallite is large enough, the bulk contribution overcomes the surface part and it can grow further.

As for the droplets observed in the crystal regime, the mechanism responsible for their formation should be quite different because thermodynamically both the bulk and surface contributions cause the free energy to increase. It is possible that after the initial solidification, a gradual relaxation from a metastable to a ground state

(e.g., from hcp to bcc or fcc structure, as one can see in Fig. 34) occurs downstream from the crystallization front. This is naturally accompanied by a release of latent heat. The droplets could then be a local manifestation of this relaxation. The larger the droplet, the longer it takes to dissipate the released heat, and the longer its lifetime. The existence of interfacial melting between two large domains seen in Fig. 36 supports this.

In order to verify whether the thermodynamic arguments can indeed be employed to explain the observed findings, we have to distinguish two possibilities: (i) *Heterophase transition*—the crystallites are smaller than the critical size N_{cr} at which they may grow continuously (Lifshitz and Pitaevskii, 1981); (ii) *homogeneous nucleation*—the crystallites are larger than the critical size N_{cr} and grow continuously until they merge with one another or with the propagating crystallization front. Correspondingly, below we use two different approaches each referring to the respective physical picture.

We start with the the heterophase transition model, which is applicable for droplets of any size and for crystallites below the nucleation threshold N_{cr} . This experimentally suggested approach is similar to the generalized statistical treatment of Born (1937), Mayer (1937), Kahn and Uhlenbeck (1938), Frenkel (1955), and others. As seen in Fig. 36 the liquid and solid phases are separated into two spatial regimes (as would be the case for the classical approach to describing condensation or epitaxial growth) but each phase is statistically intermingled with phaselets. Their distributions, expressed in terms of the numbers of particles N which they contain, can be determined from first principles. Following the ideas of Frenkel (1955), one can derive the size distribution of crystallites embedded in a melt $f_C(N)$ as well as the distribution of droplets in the crystalline regime $f_D(N)$,

$$f_{C,D}(N) \propto e^{-[\pm(\mu_c - \mu_f)N + \zeta N^{2/3}]/T}. \quad (30)$$

Here $\mu_{c,f}$ denotes the chemical potential (per particle) in the crystalline and fluid bulk phases, respectively, and ζ is the proportionality coefficient in the term that represents the surface free energy of the phaselet. Near the crystallization condition T_M it is easy to show that $\mu_c - \mu_f = L(T/T_M - 1)$ [see, e.g., Frenkel (1955)], where $L > 0$ is the latent heat of liquefaction per particle. At $T < T_M$ the threshold N_{cr} for crystallites is determined from the extremum of the exponent in Eq. (30). This theoretical model is somewhat different from the crystallization experiment shown in Fig. 36, inasmuch as it describes a homogenous system, whereas the experiment refers to a propagating crystallization front. Nevertheless, regarding the two regimes (crystal and fluid) separately, it is apparent that these measurements may still be taken to represent a snapshot of the heterophase fluctuations on either side. (Note that if the temperature is different in the two regimes, say, $T > T_M$ above the front and $T < T_M$ below the front, then N_{cr} is infinite for both crystallites and droplets.)

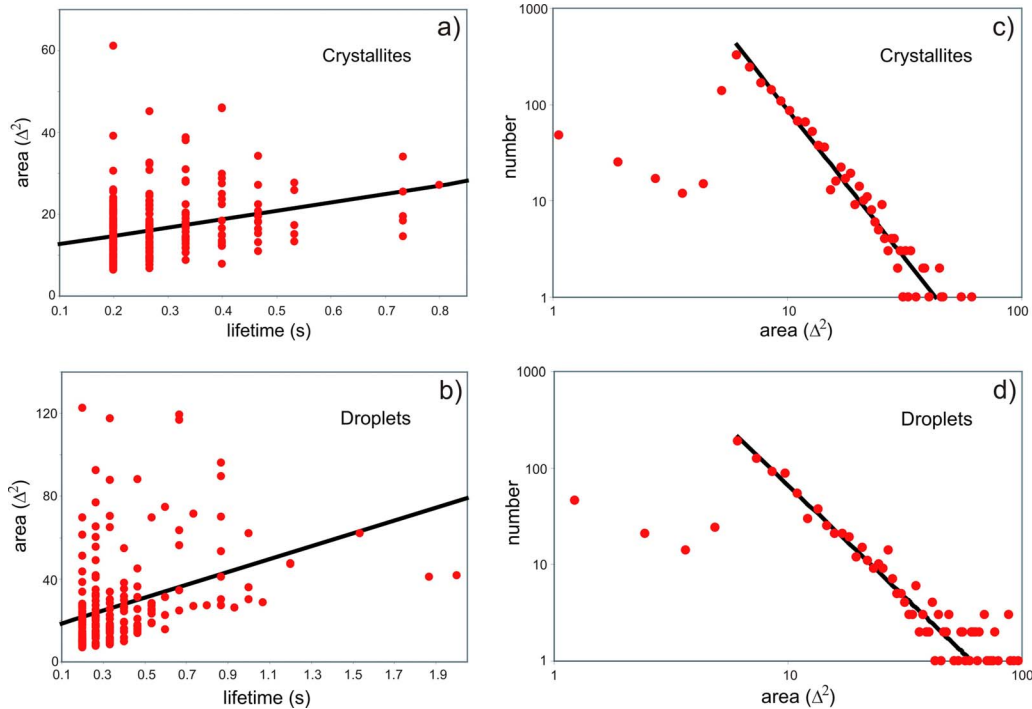


FIG. 37. (Color online) Characteristics of crystallites and droplets. (a) Area of crystallites and (b) droplets measured in units of a single particle cell (squared interparticle distance Δ^2) vs their lifetimes, and histograms showing number of (c) crystallites and (d) droplets vs their areas. Adapted from Rubin-Zuzic *et al.*, 2006.

One can see that the complex plasma data shown in (Fig. 37 right column) appear to be more compatible with a power law, whereas Eq. (30) yields an exponential decay. Furthermore, the theoretical derivation is simplified. MD studies of small liquid drops (Thompson *et al.*, 1984; Townsend and Rice, 1991; Hawa and Zachariah, 2006) have shown that the problem is quite complex, involving the detailed radius dependence of the surface tension on the internal density and pressure variation in the droplet, the surface structure, etc. While experimental evidence is still in short supply, and since there appears to be a consensus that the statistical mechanics approach is reasonably valid for small droplets, we have used the above simplified approach based on Frenkel's work and that of his contemporaries.

Now we consider the regime of homogeneous nucleation, which is applicable for crystallites only. Following Zeldovich [see, e.g., Frenkel (1955); Lifshitz and Pitaevskii (1981)], we obtain the steady-state distribution of crystallites from the Fokker-Planck approach, which yields $Df_0(\partial/\partial N)(f_C/f_0) = \text{const} \equiv J_0$. Here $D(N)$ plays the role of a diffusion in crystallite size space, J_0 is determined by an appropriate loss mechanism at the high-mass end (e.g., due to absorption of crystallites by the advancing crystallization front), and $f_0(N)$ is the equilibrium distribution [Eq. (30)] to which the solution $f_C(N)$ tends at $N \lesssim N_{\text{cr}}$. Integrating for $N > N_{\text{cr}}$ gives

$$f_C(N) = J_0 f_0(N) \int_N^{N_{\text{max}}} \frac{dN'}{D(N') f_0(N')}, \quad (31)$$

where $N_{\text{max}} \gg N_{\text{cr}}$ is the maximum size in the distribution (which generally depends on the loss mechanism). Since

$f_0(N)$ must have a pronounced peak at $N = N_{\text{cr}}$ we write it formally as a Gaussian distribution with maximum at N_{cr} . Assuming that $D(N) \propto N^\gamma$ we can evaluate the integral in Eq. (31) in a straightforward way and obtain $f_C(N) \propto N^{-\gamma}(N - N_{\text{cr}})^{-1}$. Hence, for sufficiently large $N \gg N_{\text{cr}}$ we obtain a power law $\propto N^{-(\gamma+1)}$. Note that when N approaches N_{max} , there is an abrupt cutoff.

It is interesting that for this situation we obtain a power law in the distribution of crystallite sizes for $N_{\text{cr}} \ll N \ll N_{\text{max}}$. This is compatible, in principle, with the measurements shown in Fig. 37. However, since the measured power law continues all the way down to what is practically the smallest possible crystallite size N_{min} of the order 15 particles, and since it is unreasonable to propose that $N_{\text{cr}} \lesssim N_{\text{min}}$, we have a dilemma. While the above description applies to crystallites, it is not also applicable to the droplets which were observed to have a power-law size distribution, albeit with a different exponent.

All this suggests that there must be some new and unusual physics at work here, presumably not thermodynamic equilibrium and presumably not describable with a simple Fokker-Planck approach either.

b. Interfacial melting

Regular solids usually exhibit domains of locally ordered regimes (grains), which are separated by domain (grain) boundaries (Gleiter, 2000). Thermodynamically, these grain boundaries are different (in both energy and entropy) from the homogeneous crystal regimes within. When such a grainy crystal is heated and approaches its

melting point, the grain boundaries may play a special role—they can act as seeds of premelting regions. In a number of experiments using different colloidal suspensions, the effect of grain boundary melting has been demonstrated (Pusey and van Megen, 1986; Gasser *et al.*, 2001; Alsayed *et al.*, 2005). A particular example is shown in Fig. 34(b).

A kinetic, first-principle, theory of melting faces several obstacles—there are long-range many-body interactions to contend with, there is the structural symmetry, and periodicity and universality classes are not known. Experimentally it has been possible to conduct studies with hard sphere colloids, and recently using special temperature-dependent colloidal systems [which contain microgel particles where diameters depend on temperature and therefore allow controlled tuning of the volume packing fraction, see Pusey and van Megen (1986); Alsayed *et al.* (2005)].

As a result of these experiments (and particularly also studies of ice water) it has become established that crystal surfaces may form melted layers and that similar premelting occurs at defects in crystals too. This suggests that the less perfect crystal structure and the associated interfacial free energy is the parameter that determines grain boundary melting.

Figure 36 shows that in the dynamical 3D crystallization front studies using complex plasmas interfacial melting can be also observed. This is significant for the following three reasons:

- The measurement slice shown in Fig. 36 was obtained in a large (10^6 particles) complex plasma assembly, many interparticle spacings away from the boundaries. Hence the measurements confirm that interfacial melting is not necessarily an effect confined to narrow surface regions.
- The strongly coupled complex plasma system is almost undamped. This implies that energy transport is to a large extent governed by phonons in the crystalline phase and dust-acoustic (sound) waves in the fluid regime (see Sec. II.D).
- The particle interaction is primarily electrostatic. This implies that the same process—interfacial melting—occurs in different systems with different forms of binary particle interactions. In other words, the process can be generic and is not dependent on peculiarities or special features of the system.

For these reasons we conclude that the complementarity of research between atomic, molecular, colloidal, and complex plasma studies promises to yield much more than just the sum of its parts. A ubiquitous and still poorly understood process—such as melting—needs different inputs, different constraints, generalization from different sources, and new approaches so that the principal mechanisms can be identified and combined to a fundamental kinetic theory.

IV. SUMMARY AND OUTLOOK

We mentioned in the Introduction that modern research in complex plasma physics is composed of three (mutually supporting) major directions: the investigation of the properties of this new state of soft matter, the study of generic processes in strong coupling physics, and application oriented research. In the first part of this review we highlighted some of the basic and new physics which complex plasmas enable us to study at an hitherto unprecedented resolution with respect to natural length scales (e.g., particle separation) and natural time scales (e.g., inverse Einstein or plasma frequency) for 2D as well as 3D systems—because of the optical transparency up to many thousands of interparticle distances.

Starting with the basic binary interactions we discussed processes such as wave propagation, solitons, and shocks as well as the classical phase diagram for Debye-Hückel systems. Next, we developed examples that show new physics, such as non-Hamiltonian behavior due to stochastic and systemic variations in the interaction potential and charge-induced runaway coagulation, a form of gelation phase transition.

In the second part of the review we concentrated on strong coupling phenomena in an interdisciplinary context, i.e., we highlighted those aspects of the research that would appear to have a general relevance in different areas of physics. Naturally, this emphasized the connections with another soft matter state—complex liquids—but we also addressed generic liquid and solid-state issues. The point here is, of course, that complex plasmas are the closest mesoscopic strongly coupled system known to resemble regular physical systems. In particular, the special features of complex plasmas allow for a visualization of the fully resolved atomistic dynamics in real time and space—which was not possible before.

In the fluid section, we discussed nonequilibrium dynamical heterogeneity of atoms, the kinetics of heat transport, and laminar shear flows; we focused on the development of hydrodynamic instabilities, including inertial effects in curved flows and the growth of nonlinear structures at the kinetic level—a first step towards investigating the kinetic onset of turbulence (according to Richard Feynman, “the greatest unsolved puzzle in hydrodynamics”); we summarized new physical effects observed in confined fluids and considered the electrorheological rearrangement in liquid systems. This naturally led to a discourse on the fundamental stability principles of condensed matter, the differences between solids and liquids—and, in particular, the role of 2D fluid systems.

In the study of crystals, we first focussed on 2D systems—in particular, the possibility for a local, individual particle, characterization of the coupling strength, which allows a detailed quantitative study of the development of fracture lines, dislocation dynamics, annealing, etc. We furthermore investigated the 2D melting phase transition—in the context of the different (one or two stage) theories—and concluded that 2D Yukawa-type systems are more compatible with grain-boundary-

melting scenarios, whereas dipolelike r^{-3} potentials appear to follow the KTHNY theory. This was followed by an analysis of the dislocation dynamics. Regarding 3D systems we discussed the large-scale structures, illustrating the possibilities to determine the local dynamics, the structural changes associated with domain boundaries, and interfacial melting. Finally, we investigated the kinetic structure of propagating crystallization fronts including the discovery of tiny “phaselets”—crystallites embedded in the melt and droplets in the crystalline regime.

This leaves the third direction—the present and future applications. Since we decided to concentrate on the more fundamental physics issues and the interdisciplinary aspects of complex plasma research, we only comment on this briefly here in the summary.

A field of growing importance in technology is particle control. While in most cases (e.g., plasma vapor deposition, lithography, and manufacture of computer chips) dust produced in the plasma devices is an unwanted but also unavoidable by-product of the manufacturing process, which probably accounts for billions of dollars per year in losses, there are other applications, e.g., polymorphous solar cell manufacture (Roca i Cabarrocas *et al.*, 2002), where controlled growth of nanocrystals followed by controlled deposition is a benefit. Consequently, the expertise acquired in microparticle manipulation technology (using lasers, electromagnetic fields, thermophoresis, and photophoresis) can develop into an important part of next generation plasma processing technology [see, e.g., Bouchoule (1999)].

Another topic of growing interest—on the border between basic research and applications—is plasma fusion. It has been known for a long time that tokamaks produce fine dust particles in the plasma-surface interactions (Winter, 1998). In fusion reactors, this dust will be toxic and radioactive, it can clog the gaps between the tiles on the walls and introduce thermomechanical failure, it can affect the tritium levels, etc. These are all serious considerations and it is not surprising, therefore, that increasing attention is given to dust hazard in fusion devices [see, e.g., Smirnov *et al.* (2008), and references therein]. Of particular concern—although currently not understood—is the evidence of hypervelocity dust impacts obtained from probe surface analysis in the Frascati Tokamak Upgrade, which could present a particular hazard because impacts of such particles produce more ejecta mass than that of the impactor (Castaldo *et al.*, 2007). Here research into dust production, transport, and control is also an important present and future topic.

As mentioned in the Introduction, there are other potential topics and spin-offs, ranging from plasma medicine [e.g., the sterilization, disinfection, and treatment of skin diseases—see Fridman *et al.* (2008)] and plasma biology to plasma nanofluidics (a topic partly addressed in the context of confined fluid flows in this review, but which could have technological impacts, e.g., in the design of microchannel and nanochannel systems), surface

interactions and tribology as well as pharmacy (the design and surface treatment of nano-applied medicine)—to name but a few obvious directions.

In summary, the field of complex plasmas has shown a surprising amount of new and interdisciplinary fundamental physics already. We hope that this review will provide further impetus and direction to a young and growing field and that the full potential, both for further cross-disciplinary research and for applications, will be exploited in the years to come.

ACKNOWLEDGMENTS

We are grateful to U. de Angelis, M. Fuchs, G. Joyce, S. Khrapak, R. Kompaneets, U. Konopka, H. Löwen, V. Nosenko, C. R ath, S. Ratynskaia, H. Rothermel, M. Rubin-Zuzic, P. Sheng, M. Sperl, V. Steinberg, M. Thoma, H. Thomas, V. Tsyтовich, N. Zabusky, and S. Zhdanov for valuable discussions and comments. We thank our colleagues V. Fortov, A. Lipaev, V. Molotkov, and O. Petrov for their part in realizing our joint space experiments on the ISS. We are grateful to S. Khrapak and S. Zhdanov for a critical reading of the manuscript, and to M. Fink, P. Huber, C. Knappek, V. Nosenko, R. Pompl, M. Rubin-Zuzic, and A. Yodh for permission to reproduce some of their artwork. We acknowledge partial financial support from DLR/BMWi (Grant No. 50WP0203).

REFERENCES

- Abd el Kader, A., and J. C. Earnshaw, 1999, *Phys. Rev. Lett.* **82**, 2610.
- Abraham, F. F., and H. Gao, 2000, *Phys. Rev. Lett.* **84**, 3113.
- Alba-Simionesco, A., B. Coasne, G. Dosseh, G. Dudziak, K. E. Gubbins, R. Radhakrishnan, and M. Sliwinska-Bartkowiak, 2006, *J. Phys.: Condens. Matter* **18**, R15.
- Aleksandrov, A. F., L. S. Bogdankevich, and A. A. Rukhadze, 1984, *Principles of Plasma Electrodynamics* (Springer, New York).
- Allen, J. E., 1992, *Phys. Scr.* **45**, 497.
- Al’pert, Y. L., A. V. Gurevich, and L. P. Pitaevsky, 1965, *Space Physics with Artificial Satellites* (Consultants Bureau, New York).
- Alsayed, A. M., M. F. Islam, J. Zhang, P. J. Collings, and A. G. Yodh, 2005, *Science* **309**, 1207.
- Anderson, V. J., and H. N. W. Lekkerkerker, 2002, *Nature (London)* **416**, 811.
- Annibaldi, S. V., A. V. Ivlev, U. Konopka, S. Ratynskaia, H. M. Thomas, G. E. Morfill, A. M. Lipaev, V. I. Molotkov, O. F. Petrov, and V. E. Fortov, 2007, *New J. Phys.* **9**, 327.
- Archer, L., D. Ternet, and R. Larson, 1997, *Rheol. Acta* **36**, 579.
- Arp, O., D. Block, A. Piel, and A. Melzer, 2004, *Phys. Rev. Lett.* **93**, 165004.
- Barkan, A., N. D’Angelo, and R. L. Merlino, 1994, *Phys. Rev. Lett.* **73**, 3093.
- Barnes, M. S., J. H. Keller, J. C. Forster, J. A. O’Neill, and D. K. Coultas, 1992, *Phys. Rev. Lett.* **68**, 313.
- Baroody, E. M., 1962, *Phys. Fluids* **5**, 925.
- Batchelor, G. K., 1953, *The Theory of Homogeneous Turbu-*

- lence (Cambridge University Press, Cambridge).
- Bayer, M., J. M. Brader, F. Ebert, M. Fuchs, E. Lange, G. Maret, R. Schilling, M. Sperl, and J. P. Wittmer, 2007, *Phys. Rev. E* **76**, 011508.
- Beatus, T., T. Tlustý, and R. Bar-Ziv, 2006, *Nat. Phys.* **2**, 743.
- Betz, H. D., U. Schumann, and P. Laroche, 2008, Eds., *Lightning: Principles, Instruments and Applications* (Springer, New York).
- Blum, J., *et al.*, 2000, *Phys. Rev. Lett.* **85**, 2426.
- Born, M., 1937, *Physica* (Amsterdam) **4**, 1034.
- Bouchoule, A., 1999, Ed., *Dusty Plasmas: Physics, Chemistry and Technological Impacts in Plasma Processing* (Wiley, Chichester).
- Boufendi, L., and A. Bouchoule, 1994, *Plasma Sources Sci. Technol.* **3**, 262.
- Brandt, P. C., A. V. Ivlev, and G. E. Morfill, 2009, *J. Chem. Phys.* **130**, 204513.
- Carlson, J. D., A. F. Sprecher, and H. Conrad, 1990, Eds., *Electrorheological Fluids* (Technomic, Lancaster).
- Castaldo, C., *et al.*, 2007, *Nucl. Fusion* **47**, L5.
- Chakrabarti, J., J. Dzubiella, and H. Löwen, 2004, *Phys. Rev. E* **70**, 012401.
- Chan, C.-L., W.-Y. Woon, and L. I., 2004, *Phys. Rev. Lett.* **93**, 220602.
- Chandrasekhar, S., 1961, *Hydrodynamic and Hydromagnetic Stability* (Oxford University, Oxford).
- Chen, T., R. N. Zitter, and R. Tao, 1992, *Phys. Rev. Lett.* **68**, 2555.
- Chu, J. H., and L. I., 1994, *Phys. Rev. Lett.* **72**, 4009.
- Chui, S. T., 1982, *Phys. Rev. Lett.* **48**, 933.
- Chui, S. T., 1983, *Phys. Rev. B* **28**, 178.
- Chung, P. M., L. Talbot, and K. J. Touryan, 1975, *Electric Probes in Stationary and Flowing Plasmas: Theory and Application* (Springer, New York).
- Cox, R. G., and S. Mason, 1971, *Annu. Rev. Fluid Mech.* **3**, 291.
- Cross, M., and P. Hohenberg, 1993, *Rev. Mod. Phys.* **65**, 851.
- Cui, C., and J. Goree, 1994, *IEEE Trans. Plasma Sci.* **22**, 151.
- Dassanayake, U., S. Fraden, and A. van Blaaderen, 2000, *J. Chem. Phys.* **112**, 3851.
- de Mello, A. J., 2006, *Nature* (London) **442**, 394.
- de Gennes, P. G., 1979, *J. Phys. (Paris)* **40**, 783.
- Donko, Z., J. Goree, P. Hartmann, and K. Kutasi, 2006, *Phys. Rev. Lett.* **96**, 145003.
- Drewsen, M., C. Brodersen, L. Hornekar, J. S. Hangst, and J. P. Schiffer, 1998, *Phys. Rev. Lett.* **81**, 2878.
- Dubin, D. H. E., 2000, *Phys. Plasmas* **7**, 3895.
- Epstein, P., 1924, *Phys. Rev.* **23**, 710.
- Ernst, M. H., 1986, *Fractals in Physics* (North-Holland, Amsterdam), p. 289.
- Ernst, M. H., E. H. Hauge, and J. M. J. van Leeuwen, 1970, *Phys. Rev. Lett.* **25**, 1254.
- Evans, D. J., and G. P. Morriss, 1990, *Statistical Mechanics of Nonequilibrium Liquids* (Academic, New York).
- Farouki, R. T., and S. Hamaguchi, 1994, *J. Chem. Phys.* **101**, 9885.
- Federici, G., C. H. Skinner, J. N. Brooks, J. P. Coad, C. Grisolia, A. A. Haasz, A. Hassanein, V. Philipps, C. S. Pitcher, J. Roth, W. R. Wampler, and D. G. Whyte, 2001, *Nucl. Fusion* **41**, 1967.
- Fink, M. A., *et al.*, 2005, in *New Vistas in Dusty Plasmas*, edited by L. Boufendi, M. Mikikian, and P. K. Shukla, AIP Conf. Proc. No. 799 (AIP, Melville, NY).
- Fischer, E. W., 1993, *Physica A* **201**, 183.
- Flory, P. J., 1953, *Principles of Polymer Chemistry* (Cornell University, New York).
- Fortov, V., I. Iakubov, and A. Khrapak, 2007, *Physics of Strongly Coupled Plasma* (Oxford University, New York).
- Fortov, V. E., A. V. Ivlev, S. A. Khrapak, A. G. Khrapak, and G. E. Morfill, 2005, *Phys. Rep.* **421**, 1.
- Fortov, V. E., A. G. Khrapak, S. A. Khrapak, V. I. Molotkov, A. P. Nefedov, O. F. Petrov, and V. M. Torchinsky, 2000, *Phys. Plasmas* **7**, 1374.
- Fortov, V. E., A. P. Nefedov, O. F. Petrov, A. A. Samarian, and A. V. Chernyshev, 1996, *Phys. Rev. E* **54**, R2236.
- Fortov, V. E., A. P. Nefedov, O. S. Vaulina, A. M. Lipaev, V. I. Molotkov, A. A. Samaryan, V. P. Nikitskii, A. I. Ivanov, S. F. Savin, A. V. Kalmykov, A. Y. Soloviev, and P. V. Vinogradov, 1998, *JETP* **87**, 1087.
- Fortov, V. E., A. D. Usachev, A. V. Zobnin, V. I. Molotkov, and O. F. Petrov, 2003, *Phys. Plasmas* **10**, 1199.
- Fortov, V. E., O. S. Vaulina, O. F. Petrov, M. N. Vasiliev, A. V. Gavrikov, I. A. Shakova, N. A. Vorona, Y. V. Khrustalyov, A. A. Manohin, and A. V. Chernyshev, 2007, *Phys. Rev. E* **75**, 026403.
- Frank, F. C., 1952, *Proc. R. Soc. London, Ser. A* **215**, 43.
- Frenkel, D., 1999, *Physica A* **263**, 26.
- Frenkel, J., 1955, *Kinetic Theory of Liquids* (Dover, New York).
- Fridman, G., G. Friedman, A. Gutsol, A. B. Shekhter, V. N. Vasilets, and A. Fridman, 2008, *Plasma Processes Polym.* **5**, 503.
- Fuchs, M., and M. Ballauff, 2005, *Colloids Surf., A* **270**, 232.
- Gasser, U., E. R. Weeks, A. Schofield, P. N. Pusey, and D. A. Weitz, 2001, *Science* **292**, 258.
- Gavrikov, A., I. Shakhova, A. Ivanov, O. Petrov, N. Vorona, and V. Fortov, 2005, *Phys. Lett. A* **336**, 378.
- Ginzburg, V. L., 1996, *Phys. Usp.* **39**, 973.
- Gleiter, H., 1989, *Prog. Mater. Sci.* **33**, 223.
- Gleiter, H., 2000, *Acta Mater.* **48**, 1.
- Goldsmith, H., and S. Mason, 1967, *Rheology: Theory and Application* (Academic, New York), Vol. 4, p. 87.
- Goree, J., 1994, *Plasma Sources Sci. Technol.* **3**, 400.
- Goree, J., G. E. Morfill, V. N. Tsytovich, and S. V. Vladimirov, 1999, *Phys. Rev. E* **59**, 7055.
- Götze, W., 1999, *J. Phys.: Condens. Matter* **11**, A1.
- Götze, W., and L. Sjogren, 1992, *Rep. Prog. Phys.* **55**, 241.
- Greenberg, R., and A. Brahic, 1984, Eds., *Planetary Rings* (The University of Arizona, Tucson).
- Gulley, G. L., and R. Tao, 1997, *Phys. Rev. E* **56**, 4328.
- Gumbsch, P., and H. Gao, 1999, *Science* **283**, 965.
- Hachisu, S., Y. Kobayashi, and A. Kose, 1973, *J. Colloid Interface Sci.* **42**, 342.
- Hahn, H.-S., E. A. Mason, and F. J. Smith, 1971, *Phys. Fluids* **14**, 278.
- Halperin, B. I., and D. R. Nelson, 1978, *Phys. Rev. Lett.* **41**, 121.
- Hamaguchi, S., R. T. Farouki, and D. H. E. Dubin, 1997, *Phys. Rev. E* **56**, 4671.
- Hansen, J. P., and I. R. McDonald, 1986, *Theory of Simple Liquids* (Academic, New York).
- Hansen, J. P., and D. Schiff, 1973, *Mol. Phys.* **25**, 1281.
- Hansen, J. P., and L. Verlet, 1969, *Phys. Rev.* **184**, 151.
- Hasegawa, A., 1985, *Adv. Phys.* **34**, 1.
- Havnes, O., T. Aslaksen, T. W. Hartquist, F. Li, F. Melandsø, G. E. Morfill, and T. Nitter, 1995, *J. Geophys. Res.* **100**, 1731.

- Havnes, O., C. K. Goertz, G. E. Morfill, E. Grun, and W. Ip, 1987, *J. Geophys. Res.*, [Atmos.] **92**, 2281.
- Havnes, O., F. Li, F. Melandsø, T. Aslaksen, T. W. Hartquist, G. E. Morfill, T. Nitter, and V. Tsytovich, 1996, *J. Vac. Sci. Technol. A* **14**, 525.
- Hawa, T., and M. Zachariah, 2006, *J. Aerosol Sci.* **37**, 1.
- Hayashi, Y., and S. Tachibana, 1994, *Jpn. J. Appl. Phys.* **33**, L804.
- Helbing, D., I. J. Farkas, and T. Vicsek, 2000, *Phys. Rev. Lett.* **84**, 1240.
- Heller, D. A., E. S. Jeng, T.-K. Yeung, B. M. Martinez, A. E. Moll, J. B. Gastala, and M. S. Strano, 2006, *Science* **311**, 508.
- Hewins, R., R. Jones, and E. Scott, 1996, Eds., *Chondrules and the Protoplanetary Disk* (Cambridge University, Cambridge).
- Holmes, C. B., M. E. Cates, M. Fuchs, and P. Sollich, 2005, *J. Rheol.* **49**, 237.
- Holtz, J. H., and S. A. Asher, 1997, *Nature (London)* **389**, 829.
- Hoover, W. G., 1985, *Phys. Rev. A* **31**, 1695.
- Hou, L.-J., Y.-N. Wang, and Z. L. Miskovic, 2003, *Phys. Rev. E* **68**, 016410.
- Huang, Y.-H, and L. I, 2007, *Phys. Rev. E* **76**, 016403.
- Hummer, G., J. C. Rasaiah, and J. P. Noworyta, 2001, *Nature (London)* **414**, 188.
- Hutchinson, I. H., and L. Patacchini, 2007, *Phys. Plasmas* **14**, 013505.
- Hynninen, A.-P., and M. Dijkstra, 2005, *Phys. Rev. Lett.* **94**, 138303.
- Ichimaru, S., H. Iyetomi, and S. Tanaka, 1987, *Phys. Rep.* **149**, 91.
- Ishihara, O., and S. V. Vladimirov, 1997, *Phys. Plasmas* **4**, 69.
- Ivlev, A. V., U. Konopka, and G. Morfill, 2000, *Phys. Rev. E* **62**, 2739.
- Ivlev, A. V., U. Konopka, G. Morfill, and G. Joyce, 2003, *Phys. Rev. E* **68**, 026405.
- Ivlev, A. V., and G. Morfill, 2001, *Phys. Rev. E* **63**, 026412.
- Ivlev, A. V., G. E. Morfill, and U. Konopka, 2002, *Phys. Rev. Lett.* **89**, 195502.
- Ivlev, A. V., V. Steinberg, R. Kompaneets, H. Höfner, I. Sidorenko, and G. E. Morfill, 2007, *Phys. Rev. Lett.* **98**, 145003.
- Ivlev, A. V., S. K. Zhdanov, S. A. Khrapak, and G. E. Morfill, 2005, *Phys. Rev. E* **71**, 016405.
- Ivlev, A. V., S. K. Zhdanov, B. A. Klumov, and G. E. Morfill, 2005, *Phys. Plasmas* **12**, 092104.
- Ivlev, A. V., S. K. Zhdanov, B. A. Klumov, V. N. Tsytovich, U. de Angelis, and G. E. Morfill, 2004, *Phys. Rev. E* **70**, 066401.
- Ivlev, A. V., S. K. Zhdanov, and G. E. Morfill, 2007, *Phys. Rev. Lett.* **99**, 135004.
- Ivlev, A. V., S. K. Zhdanov, H. M. Thomas, and G. E. Morfill, 2009, *Europhys. Lett.* **85**, 45001.
- Ivlev, A. V., *et al.*, 2008, *Phys. Rev. Lett.* **100**, 095003.
- Jäckle, J., 1986, *Rep. Prog. Phys.* **49**, 171.
- Janiaud, E., D. Weaire, and S. Hutzler, 2006, *Phys. Rev. Lett.* **97**, 038302.
- Juan, W.-T., M.-H. Chen, and L. I, 2001, *Phys. Rev. E* **64**, 016402.
- Jullien, R., and R. Botet, 1987, *Aggregation and Fractal Aggregates* (World Scientific, Singapore).
- Kadau, K., T. C. Germann, N. G. Hadjiconstantinou, P. S. Lomdahl, G. Dimonte, B. L. Holian, and B. J. Alder, 2004, *Proc. Natl. Acad. Sci. U.S.A.* **101**, 5851.
- Kahn, B., and G. E. Uhlenbeck, 1938, *Physica (Amsterdam)* **5**, 399.
- Kalman, G., and K. I. Golden, 1990, *Phys. Rev. A* **41**, 5516.
- Kalman, G., M. Rosenberg, and H. E. DeWitt, 2000, *Phys. Rev. Lett.* **84**, 6030.
- Karpman, V. I., 1975, *Nonlinear Waves in Dispersive Media* (Pergamon, Oxford).
- Kaw, P. K., 2001, *Phys. Plasmas* **8**, 1870.
- Kaw, P. K., and A. Sen, 1998, *Phys. Plasmas* **5**, 3552.
- Kegel, W. K., and A. van Blaaderen, 2000, *Science* **287**, 290.
- Kempf, S., S. Pfalzner, and T. Henning, 1999, *Icarus* **141**, 388.
- Kennedy, R. V., and J. E. Allen, 2003, *J. Plasma Phys.* **69**, 485.
- Khodataev, Y. K., S. A. Khrapak, A. P. Nefedov, and O. F. Petrov, 1998, *Phys. Rev. E* **57**, 7086.
- Khrapak, S. A., A. V. Ivlev, and G. E. Morfill, 2004, *Phys. Rev. E* **70**, 056405.
- Khrapak, S. A., A. V. Ivlev, G. E. Morfill, and H. M. Thomas, 2002, *Phys. Rev. E* **66**, 046414.
- Khrapak, S. A., A. V. Ivlev, G. E. Morfill, and S. K. Zhdanov, 2003, *Phys. Rev. Lett.* **90**, 225002.
- Khrapak, S. A., B. A. Klumov, and G. E. Morfill, 2008, *Phys. Rev. Lett.* **100**, 225003.
- Khrapak, S. A., and G. Morfill, 2001, *Phys. Plasmas* **8**, 2629.
- Khrapak, S. A., G. E. Morfill, A. V. Ivlev, H. M. Thomas, D. A. Beysens, B. Zappoli, V. E. Fortov, A. M. Lipaev, and V. I. Molotkov, 2006, *Phys. Rev. Lett.* **96**, 015001.
- Khrapak, S. A., A. P. Nefedov, O. F. Petrov, and O. S. Vaulina, 1999, *Phys. Rev. E* **59**, 6017.
- Khrapak, S. A., S. V. Ratynskaia, A. V. Zobnin, A. D. Usachev, V. V. Yaroshenko, M. H. Thoma, M. Kretschmer, H. Höfner, G. E. Morfill, O. F. Petrov, and V. E. Fortov, 2005, *Phys. Rev. E* **72**, 016406.
- Khrapak, S., *et al.*, 2003, *Phys. Plasmas* **10**, 1.
- Kirchner, H. O. K., G. Michot, and J. Schweizer, 2002, *Phys. Rev. E* **66**, 027103.
- Kittel, C., 1961, *Introduction to Solid State Physics* (Wiley, New York).
- Knapek, C. A., A. V. Ivlev, B. A. Klumov, G. E. Morfill, and D. Samsonov, 2007, *Phys. Rev. Lett.* **98**, 015001.
- Knapek, C. A., D. Samsonov, S. Zhdanov, U. Konopka, and G. E. Morfill, 2007, *Phys. Rev. Lett.* **98**, 015004.
- Koch, D. L., and R. J. Hill, 2001, *Annu. Rev. Fluid Mech.* **33**, 619.
- Kompaneets, R., 2007, Ph.D. thesis, Ludwig-Maximilians-Universität München.
- Kompaneets, R., A. V. Ivlev, V. Tsytovich, and G. Morfill, 2005, *Phys. Plasmas* **12**, 062107.
- Kompaneets, R., U. Konopka, A. V. Ivlev, V. Tsytovich, and G. Morfill, 2007, *Phys. Plasmas* **14**, 052108.
- Kompaneets, R., G. E. Morfill, and A. V. Ivlev, 2009, *Phys. Plasmas* **16**, 043705.
- Konopka, U., *et al.*, 2005, *New J. Phys.* **7**, 227.
- Kosterlitz, J. M., and D. J. Thouless, 1973, *J. Phys. C* **6**, 1181.
- Kremer, K., M. O. Robbins, and G. S. Grest, 1986, *Phys. Rev. Lett.* **57**, 2694.
- Lai, Y.-J., and L. I, 2002, *Phys. Rev. Lett.* **89**, 155002.
- Lampe, M., V. Gavrishchaka, G. Ganguli, and G. Joyce, 2001, *Phys. Rev. Lett.* **86**, 5278.
- Lampe, M., G. Joyce, and G. Ganguli, 2001, *Phys. Scr.*, T **T89** 106.
- Lampe, M., G. Joyce, G. Ganguli, and V. Gavrishchaka, 2000, *Phys. Plasmas* **7**, 3851.
- Landau, L. D., and E. M. Lifshitz, 1976, *Mechanics* (Pergamon, Oxford).
- Landau, L. D., and E. M. Lifshitz, 1978, *Statistical Physics. Part I* (Pergamon, Oxford).

- Landau, L. D., and E. M. Lifschitz, 1986, *Theory of Elasticity* (Pergamon, Oxford).
- Landau, L. D., and E. M. Lifschitz, 1987, *Fluid Mechanics* (Pergamon, Oxford).
- Lapenta, G., 2000, Phys. Rev. E **62**, 1175.
- Lapenta, G., 2002, Phys. Rev. E **66**, 026409.
- Laroussi, M., and X. Lu, 2005, Appl. Phys. Lett. **87**, 113902.
- Lee, M. H., 2000, Icarus **143**, 74.
- Lemons, D. S., M. S. Murillo, W. Daughton, and D. Winske, 2000, Phys. Plasmas **7**, 2306.
- Leunissen, M. E., C. G. Christova, A.-P. Hynninen, C. P. Royall, A. I. Campbell, A. Imhof, M. Dijkstra, R. van Roij, and A. van Blaaderen, 2005, Nature (London) **437**, 235.
- Lifshitz, E. M., and L. P. Pitaevskii, 1981, *Physical Kinetics* (Pergamon, Oxford).
- Lindemann, F. A., 1910, Z. Phys. **11**, 609.
- Lissauer, J. J., 1993, Annu. Rev. Astron. Astrophys. **31**, 129.
- Liu, B., and J. Goree, 2007, Phys. Rev. E **75**, 016405.
- Liu, B., and J. Goree, 2008, Phys. Rev. Lett. **100**, 055003.
- Liu, B., J. Goree, V. Nosenko, and L. Boufendi, 2003, Phys. Plasmas **10**, 9.
- Löwen, H., 1996, Phys. Rev. E **53**, R29.
- Löwen, H., T. Palberg, and R. Simon, 1993, Phys. Rev. Lett. **70**, 1557.
- Lucas, R. A., A. Omant, and R. Stora, 1985, Eds., *Birth and Infancy of Stars* (Elsevier, Amsterdam).
- March, N., and M. P. Tosi, 2002, *Introduction to Liquid State Physics* (World Scientific, London).
- Marcus, A. H., and S. A. Rice, 1997, Phys. Rev. E **55**, 637.
- Matsoukas, T., and M. Russell, 1997, Phys. Rev. E **55**, 991.
- Mayer, J. E., 1937, J. Chem. Phys. **5**, 67.
- Meakin, P., 1991, Rev. Geophys. **29**, 317.
- Meijer, E. J., and D. Frenkel, 1991, J. Chem. Phys. **94**, 2269.
- Meijer, E. J., and D. Frenkel, 1994, J. Chem. Phys. **100**, 6873.
- Melandsø, F., and J. Goree, 1995, Phys. Rev. E **52**, 5312.
- Melzer, A., 2003, Phys. Rev. E **67**, 016411.
- Melzer, A., D. Block, and A. Piel, 2007, Physik J. **6**, 31.
- Melzer, A., A. Homann, and A. Piel, 1996, Phys. Rev. E **53**, 2757.
- Melzer, A., S. Nunomura, D. Samsonov, Z. W. Ma, and J. Goree, 2000, Phys. Rev. E **62**, 4162.
- Melzer, A., V. A. Schweigert, and A. Piel, 1999, Phys. Rev. Lett. **83**, 3194.
- Melzer, A., V. A. Schweigert, I. V. Schweigert, A. Homann, S. Peters, and A. Piel, 1996, Phys. Rev. E **54**, R46.
- Merlino, R. L., A. Barkan, C. Thompson, and N. D'Angelo, 1998, Phys. Plasmas **5**, 1607.
- Meyers, M. A., and K. K. Chawla, 1998, *Mechanical Behavior of Materials* (Prentice Hall, Englewood Cliffs, NJ).
- Miller, S. A., V. Y. Young, and C. R. Martin, 2001, J. Am. Chem. Soc. **123**, 12335.
- Misawa, T., N. Ohno, K. Asano, M. Sawai, S. Takamura, and P. K. Kaw, 2001, Phys. Rev. Lett. **86**, 1219.
- Montgomery, D., G. Joyce, and R. Sugihara, 1968, Phys. Plasmas **10**, 681.
- Morfill, G. E., S. A. Khrapak, A. V. Ivlev, B. A. Klumov, M. Rubin-Zuzic, and H. M. Thomas, 2004, Phys. Scr., T **1107**, 59.
- Morfill, G. E., U. Konopka, M. Kretschmer, M. Rubin-Zuzic, H. M. Thomas, S. K. Zhdanov, and V. Tsytovich, 2006, New J. Phys. **8**, 7.
- Morfill, G. E., M. Rubin-Zuzic, H. Rothermel, A. Ivlev, B. Klumov, H. Thomas, and U. Konopka, 2004, Phys. Rev. Lett. **92**, 175004.
- Morfill, G. E., and M. Scholer, 1987, Eds., *Physical Processes in Interstellar Clouds* (Reidel, Dordrecht).
- Morfill, G. E., H. M. Thomas, U. Konopka, H. Rothermel, M. Zuzic, A. Ivlev, and J. Goree, 1999, Phys. Rev. Lett. **83**, 1598.
- Murayama, M., J. M. Howe, H. Hidaka, and S. Takaki, 2002, Science **295**, 2433.
- Murillo, M. S., 1998, Phys. Plasmas **5**, 3116.
- Murillo, M. S., 2000, Phys. Plasmas **7**, 33.
- Murray, C. H., and D. H. V. Winkle, 1987, Phys. Rev. Lett. **58**, 1200.
- Nambu, M., S. V. Vladimirov, and P. K. Shukla, 1995, Phys. Lett. A **203**, 40.
- Nefedov, A. P., O. F. Petrov, and V. E. Fortov, 1997, Phys. Usp. **40**, 1163.
- Nefedov, A. P., O. F. Petrov, Y. K. Khodataev, and S. A. Khrapak, 1999, JETP **88**, 460.
- Nefedov, A. P., et al., 2003, New J. Phys. **5**, 33.
- Nelson, D. R., 2002, *Defects and Geometry in Condensed Matter Physics* (Cambridge University, Cambridge).
- Nelson, D. R., and B. I. Halperin, 1979, Phys. Rev. B **19**, 2457.
- Nosenko, V., and J. Goree, 2004, Phys. Rev. Lett. **93**, 155004.
- Nosenko, V., J. Goree, Z. W. Ma, D. H. E. Dubin, and A. Piel, 2003, Phys. Rev. E **68**, 056409.
- Nosenko, V., J. Goree, Z. W. Ma, and A. Piel, 2002, Phys. Rev. Lett. **88**, 135001.
- Nosenko, V., S. Nunomura, and J. Goree, 2002, Phys. Rev. Lett. **88**, 215002.
- Nosenko, V., S. K. Zhdanov, A. V. Ivlev, C. A. Knapek, and G. E. Morfill, 2009, Phys. Rev. Lett. **103**, 015001.
- Nosenko, V., S. Zhdanov, A. V. Ivlev, G. Morfill, J. Goree, and A. Piel, 2008, Phys. Rev. Lett. **100**, 025003.
- Nosenko, V., S. Zhdanov, and G. Morfill, 2007, Phys. Rev. Lett. **99**, 025002.
- Nozieres, P., and D. Quemada, 1986, Europhys. Lett. **2**, 129.
- Nunomura, S., J. Goree, S. Hu, X. Wang, and A. Bhattacharjee, 2002, Phys. Rev. E **65**, 066402.
- Nunomura, S., T. Misawa, N. Ohno, and S. Takamura, 1999, Phys. Rev. Lett. **83**, 1970.
- Nunomura, S., D. Samsonov, and J. Goree, 2000, Phys. Rev. Lett. **84**, 5141.
- Nunomura, S., D. Samsonov, S. Zhdanov, and G. Morfill, 2006, Phys. Rev. Lett. **96**, 015003.
- Ohta, H., and S. Hamaguchi, 2000a, Phys. Rev. Lett. **84**, 6026.
- Ohta, H., and S. Hamaguchi, 2000b, Phys. Plasmas **7**, 4506.
- Papoular, M., 1987, J. Phys. A **20**, L649.
- Peeters, F. M., and X. Wu, 1987, Phys. Rev. A **35**, 3109.
- Perera, D. N., and P. Harrowell, 1999, Phys. Rev. E **59**, 5721.
- Pham, K. N., A. M. Puertas, J. Bergenholtz, S. U. Egelhaaf, A. Moussaid, P. N. Pusey, A. B. Schofield, M. E. Cates, M. Fuchs, and W. C. K. Poon, 2002, Science **296**, 104.
- Phillipot, S. R., and D. Wolf, 1990, J. Am. Ceram. Soc. **73**, 933.
- Piel, A., M. Klindworth, O. Arp, A. Melzer, and M. Wolter, 2006, Phys. Rev. Lett. **97**, 205009.
- Pramanik, J., G. Prasad, A. Sen, and P. K. Kaw, 2002, Phys. Rev. Lett. **88**, 175001.
- Prigogine, I., 1980, *From Being to Becoming* (Freeman, San Francisco).
- Pusey, P. N., 2005, Science **309**, 1198.
- Pusey, P. N., and W. van Meegen, 1986, Nature (London) **320**, 340.
- Pustyl'nik, M. Y., N. Ohno, S. Takamura, and R. Smirnov, 2006, Phys. Rev. E **74**, 046402.
- Qian, T., X.-P. Wang, and P. Sheng, 2006, J. Fluid Mech. **564**,

- 333.
- Quinn, R. A., C. Cui, J. Goree, J. B. Pieper, H. Thomas, and G. E. Morfill, 1996, *Phys. Rev. E* **53**, R2049.
- Rao, N. N., P. K. Shukla, and M. Y. Yu, 1990, *Planet. Space Sci.* **38**, 543.
- Räth, C., W. Bunk, M. Huber, G. Morfill, J. Retzlaff, and P. Schuecker, 2002, *Mon. Not. R. Astron. Soc.* **337**, 413.
- Ratynskaia, S., K. Rypdal, C. Knapek, S. Khrapak, A. V. Milovanov, A. Ivlev, J. J. Rasmussen, and G. E. Morfill, 2006, *Phys. Rev. Lett.* **96**, 105010.
- Raveche, H. J., R. D. Mountain, and W. B. Streett, 1974, *J. Chem. Phys.* **61**, 1970.
- Reichert, H., 2002, *Physik J.* **1**, 83.
- Reichert, H., O. Klein, H. Dosch, M. Denk, V. Honkimäki, T. Lippmann, and G. Reiter, 2000, *Nature (London)* **408**, 839.
- Reichman, D. R., E. Rabani, and P. L. Geissler, 2005, *J. Phys. Chem. B* **109**, 14654.
- Robbins, M. O., K. Kremer, and G. S. Grest, 1988, *J. Chem. Phys.* **88**, 3286.
- Roca i Cabarrocas, P., A. Fontcuberta i Morral, and Y. Poissant, 2002, *Thin Solid Films* **403**, 39.
- Rosakis, A. J., O. Samudrala, and D. Coker, 1999, *Science* **284**, 1337.
- Rose-Petruck, C., R. Jimenez, T. Guo, A. Cavalleri, C. W. Siders, F. Raksi, J. Squier, B. Walker, K. R. Wilson, and C. P. J. Barty, 1999, *Nature (London)* **398**, 310.
- Rosenberg, M., and G. Kalman, 1997, *Phys. Rev. E* **56**, 7166.
- Rothermel, H., T. Hagl, G. E. Morfill, M. H. Thoma, and H. M. Thomas, 2002, *Phys. Rev. Lett.* **89**, 175001.
- Rubin-Zuzic, M., G. E. Morfill, A. V. Ivlev, R. Pompl, B. A. Klumov, W. Bunk, H. M. Thomas, H. Rothermel, O. Havnes, and A. Fouquet, 2006, *Nat. Phys.* **2**, 181.
- Sagdeev, R. Z., 1966, *Reviews of Plasma Physics* (Consultants Bureau, New York) Vol. 4, p. 23.
- Saigo, T., and S. Hamaguchi, 2002, *Phys. Plasmas* **9**, 1210.
- Saija, F., S. Prestipino, and P. V. Giaquinto, 2006, *J. Chem. Phys.* **124**, 244504.
- Salin, G., and J.-M. Caillol, 2002, *Phys. Rev. Lett.* **88**, 065002.
- Salin, G., and J.-M. Caillol, 2003, *Phys. Plasmas* **10**, 1220.
- Salmon, J.-B., A. Colin, S. Manneville, and F. Molino, 2003, *Phys. Rev. Lett.* **90**, 228303.
- Saltzman, E. J., and K. S. Schweizer, 2006, *J. Chem. Phys.* **125**, 044509.
- Samaryan, A. A., A. V. Chernyshev, A. P. Nefedov, O. F. Petrov, Y. M. Mikhailov, V. B. Mintsev, and V. E. Fortov, 2000, *JETP* **90**, 817.
- Samsonov, D., and J. Goree, 1999, *Phys. Rev. E* **59**, 1047.
- Samsonov, D., J. Goree, Z. W. Ma, A. Bhattacharjee, H. M. Thomas, and G. E. Morfill, 1999, *Phys. Rev. Lett.* **83**, 3649.
- Samsonov, D., J. Goree, H. M. Thomas, and G. E. Morfill, 2000, *Phys. Rev. E* **61**, 5557.
- Samsonov, D., A. V. Ivlev, R. A. Quinn, G. Morfill, and S. Zhdanov, 2002, *Phys. Rev. Lett.* **88**, 095004.
- Samsonov, D., S. Zhdanov, and G. Morfill, 2005, *Phys. Rev. E* **71**, 026410.
- Samsonov, D., S. Zhdanov, R. A. Quinn, S. I. Popel, and G. E. Morfill, 2004, *Phys. Rev. Lett.* **92**, 255004.
- Santen, L., and W. Krauth, 2000, *Nature (London)* **405**, 550.
- Schall, P., J. Cohen, D. A. Weitz, and F. Spaepen, 2004, *Science* **305**, 1944.
- Schätz, T., U. Schramm, and D. Habs, 2001, *Nature (London)* **412**, 717.
- Schirmacher, W., G. Diesemann, and C. Ganter, 1998, *Phys. Rev. Lett.* **81**, 136.
- Schwabe, M., M. Rubin-Zuzic, S. Zhdanov, H. M. Thomas, and G. E. Morfill, 2007, *Phys. Rev. Lett.* **99**, 095002.
- Schweigert, V. A., 2001, *Plasma Phys. Rep.* **27**, 997.
- Shimada, T., T. Murakami, S. Yukawa, and N. Ito, 2000, *J. Phys. Soc. Jpn.* **69**, 3150.
- Shintani, H., and H. Tanaka, 2006, *Nat. Phys.* **2**, 200.
- Shukla, P. K., 2003, *Phys. Plasmas* **10**, 1619.
- Shukla, P. K., and B. Eliasson, 2009, *Rev. Mod. Phys.* **81**, 25.
- Shukla, P. K., and A. A. Mamun, 2001, *Introduction to Dusty Plasma Physics* (IOP, Bristol).
- Sickafoose, A. A., J. E. Colwell, M. Horanyi, and S. Robertson, 2000, *Phys. Rev. Lett.* **84**, 6034.
- Sillescu, H., 1999, *J. Non-Cryst. Solids* **243**, 81.
- Slattery, W. L., G. D. Doolen, and H. E. DeWitt, 1980, *Phys. Rev. A* **21**, 2087.
- Smirnov, R. D., A. Y. Pigarov, M. Rosenberg, S. I. Krasheninnikov, and D. A. Mendis, 2007, *Plasma Phys. Controlled Fusion* **49**, 347.
- Smirnov, R. D., *et al.*, 2008, in *Multifacets of Dusty Plasma*, edited by J. T. Mendonca, D. P. Resendes, and P. K. Shukla, AIP Con. Proc. No. 1041 (AIP, Melville, NY), p. 59.
- Smoluchowski, M., 1917, *Z. Phys. Chem.* **92**, 129.
- Stangroom, J. E., 1983, *Phys. Technol.* **14**, 290.
- Steinberg, V., A. V. Ivlev, R. Kompaneets, and G. E. Morfill, 2008, *Phys. Rev. Lett.* **100**, 254502.
- Stevens, M. J., and M. O. Robbins, 1993, *J. Chem. Phys.* **98**, 2319.
- Stillinger, F. H., 1995, *Science* **267**, 1935.
- Stoffels, E., A. J. Flikweert, W. W. Stoffels, and G. M. W. Kroesen, 2002, *Plasma Sources Sci. Technol.* **11**, 383.
- Strandburg, K. J., 1988, *Rev. Mod. Phys.* **60**, 161.
- Sütterlin, K. R., *et al.*, 2009, *Phys. Rev. Lett.* **102**, 085003.
- Takagiwa, H., E. Nishibori, N. Okada, M. Takata, M. Sakata, and J. Akimitsu, 2006, *Sci. Technol. Adv. Mater.* **7**, 22.
- Tao, R., 1993, *Phys. Rev. E* **47**, 423.
- Teng, L.-W., P.-S. Tu, and L. I., 2003, *Phys. Rev. Lett.* **90**, 245004.
- Tennekes, H., and J. L. Lumley, 1972, *A First Course in Turbulence* (MIT, Cambridge).
- Thomas, E., Jr., R. Fisher, and R. L. Merlino, 2007, *Phys. Plasmas* **14**, 123701.
- Thomas, H., G. E. Morfill, V. Demmel, J. Goree, B. Feuerbacher, and D. Möhlmann, 1994, *Phys. Rev. Lett.* **73**, 652.
- Thomas, H. M., and G. E. Morfill, 1996, *Nature (London)* **379**, 806.
- Thompson, S. M., K. E. Gubbins, J. P. R. B. Walton, R. A. R. Chanry, and J. S. Rowlinson, 1984, *J. Chem. Phys.* **81**, 530.
- Townsend, R. M., and S. A. Rice, 1991, *J. Chem. Phys.* **94**, 2207.
- Tsyтович, V., G. Morfill, S. Vladimirov, and H. Thomas, 2008, *Elementary Physics of Complex Plasmas* (Springer, New York).
- Tsyтович, V. N., 1997, *Phys. Usp.* **40**, 53.
- Tuckerman, M. E., Y. Liu, G. Ciccotti, and G. J. Martyna, 2001, *J. Chem. Phys.* **115**, 1678.
- Uglov, A. A., and A. G. Gnedovets, 1991, *Plasma Chem. Plasma Process.* **11**, 251.
- Uhlenbeck, G. E., and L. S. Ornstein, 1930, *Phys. Rev.* **36**, 823.
- Vaitheeswaran, S., J. C. Rasaiah, and G. Hummer, 2004, *J. Chem. Phys.* **121**, 7955.
- van Kampen, N. G., 1981, *Stochastic Processes in Physics and Chemistry* (Elsevier, Amsterdam).

- van Zanten, J., and K. P. Rufener, 2000, *Phys. Rev. E* **62**, 5389.
- Vaulina, O., S. Khrapak, and G. Morfill, 2002, *Phys. Rev. E* **66**, 016404.
- Vaulina, O., S. Khrapak, A. P. Nefedov, and O. F. Petrov, 1999, *Phys. Rev. E* **60**, 5959.
- Vaulina, O. S., and I. E. Dranzhevskii, 2007, *Plasma Phys. Rep.* **33**, 494.
- Vaulina, O. S., and S. A. Khrapak, 2000, *JETP* **90**, 287.
- Vaulina, O. S., and S. A. Khrapak, 2001, *JETP* **92**, 228.
- Vaulina, O. S., A. P. Nefedov, O. F. Petrov, and V. E. Fortov, 2000, *JETP* **91**, 1147.
- Vladimirov, S. V., S. A. Maierov, and O. Ishihara, 2003, *Phys. Plasmas* **10**, 3867.
- Vladimirov, S. V., K. Ostrikov, and A. A. Samarian, 2005, *Physics and Applications of Complex Plasmas* (Imperial College, London).
- Vlasov, Y. A., X.-Z. Bo, J. C. Sturm, and D. J. Norris, 2001, *Nature* (London) **414**, 289.
- Walch, B., M. Horanyi, and S. Robertson, 1995, *Phys. Rev. Lett.* **75**, 838.
- Wang, C. L., G. Joyce, and D. R. Nicholson, 1981, *J. Plasma Phys.* **25**, 225.
- Wang, X., A. Bhattacharjee, and S. Hu, 2001, *Phys. Rev. Lett.* **86**, 2569.
- Weaire, D., and S. Hutzler, 2000, *The Physics of Foams* (Oxford Univ., Oxford).
- Wette, P., I. Klassen, D. Holland-Moritz, T. Palberg, S. V. Roth, and D. M. Herlach, 2009, *Phys. Rev. E* **79**, 010501(R).
- Whipple, E., 1981, *Rep. Prog. Phys.* **44**, 1197.
- Whitby, M., and N. Quirke, 2007, *Nat. Nanotechnol.* **2**, 87.
- Wijnhoven, J. E. G. J., and W. L. Vos, 1998, *Science* **281**, 802.
- Winske, D., 2001, *IEEE Trans. Plasma Sci.* **29**, 191.
- Winske, D., M. S. Murillo, and M. Rosenberg, 1999, *Phys. Rev. E* **59**, 2263.
- Winter, J., 1998, *Plasma Phys. Controlled Fusion* **40**, 1201.
- Woon, W.-Y., and L. I., 2004, *Phys. Rev. Lett.* **92**, 065003.
- Wysocki, A., and H. Löwen, 2004, *J. Phys.: Condens. Matter* **16**, 7209.
- Xia, Y. N., B. Gates, Y. D. Yin, and Y. Lu, 2000, *Adv. Mater.* **12**, 693.
- Xie, B., K. He, and Z. Huang, 1999, *Phys. Lett. A* **253**, 83.
- Xie, B. S., and M. Y. Yu, 2000, *Phys. Rev. E* **62**, 8501.
- Yaroshenkov, V. V., A. V. Ivlev, and G. E. Morfill, 2005, *Phys. Rev. E* **71**, 046405.
- Yazaki, A., H. Kishimura, H. Kawano, Y. Hironaka, K. G. Nakamura, and K. Kondo, 2002, *J. Appl. Phys.* **41**, 1614.
- Yethiraj, A., and A. van Blaaderen, 2003, *Nature* (London) **421**, 513.
- Yethiraj, A., J. H. J. Thijssen, A. Wouterse, and A. van Blaaderen, 2004, *Adv. Mater.* **16**, 596.
- Yokoyama, S., Y. Honda, H. Morioka, S. Okamoto, H. Funakubo, T. Iijima, H. Matsuda, K. Saito, T. Yamamoto, H. Okino, O. Sakata, and S. Kimura, 2005, *J. Appl. Phys.* **98**, 094106.
- Young, A. P., 1979, *Phys. Rev. B* **19**, 1855.
- Zahn, K., and G. Maret, 2000, *Phys. Rev. Lett.* **85**, 3656.
- Zhakhovskii, V. V., V. I. Molotkov, A. P. Nefedov, V. M. Torchinski, A. G. Khrapak, and V. E. Fortov, 1997, *JETP* **66**, 419.
- Zhdanov, S., S. Nunomura, D. Samsonov, and G. Morfill, 2003, *Phys. Rev. E* **68**, 035401(R).
- Zhdanov, S., R. A. Quinn, D. Samsonov, and G. E. Morfill, 2003, *New J. Phys.* **5**, 74.
- Zhdanov, S. K., A. V. Ivlev, and G. E. Morfill, 2005, *Phys. Plasmas* **12**, 072312.
- Zhdanov, S. K., D. Samsonov, and G. E. Morfill, 2002, *Phys. Rev. E* **66**, 026411.
- Zheng, X. H., and J. C. Earnshaw, 1998, *Europhys. Lett.* **41**, 635.
- Zhu, X., R. Birringer, U. Herr, and H. Gleiter, 1987, *Phys. Rev. B* **35**, 9085.
- Zobnin, A. V., A. P. Nefedov, V. A. Sinelshchikov, and V. E. Fortov, 2000, *JETP* **91**, 483.
- Zobnin, A. V., A. D. Usachev, O. F. Petrov, and V. E. Fortov, 2002, *JETP* **95**, 429.
- Zorn, R., 2003, *J. Phys.: Condens. Matter* **15**, R1025.
- Zuzic, M., A. V. Ivlev, J. Goree, G. E. Morfill, H. M. Thomas, H. Rothermel, U. Konopka, R. Sütterlin, and D. D. Goldbeck, 2000, *Phys. Rev. Lett.* **85**, 4064.